Chapter 1
Introduction

1.1 Background

A laser consists of an active element that provides the energy levels for the laser transition, mirrors that enable control of the laser process through cavity feedback and finally a pump source that provides the necessary energy. In some lasers, a host material is also needed to form a stable environment for the active element. The active element, together with the host material if applicable, constitutes the gain medium, also called the laser medium. The nature of this medium makes up the main classification system for lasers; gas lasers, dye lasers, semiconductor lasers and solid-state lasers. This thesis will concern the latter class when using a semiconductor laser as the pump source, i.e. diode-pumped solid-state lasers (DPSSLs).

In a DPSSL, the active element is an ion doped into a dielectric host material. Except for the actinide U^{3+}, the ions are either lanthanides such as Yb^{3+}, Er^{3+}, Nd^{3+}, Ho^{3+} and Tm^{3+} or transition metals such as $Cr^{2+,\ 3+,\ 4+}$, Ti^{3+} and Fe^{2+}. The wide variety of host materials includes glasses, ceramics and crystals like borates, fluorides, oxides and chlorides. Up until now, at least 620 different materials have been evaluated for laser purposes.[1] This multitude is actually one of the strengths of the DPSSL, since it gives the possibility to optimize the laser medium for each given situation. Furthermore, the laser material geometry can also be optimized to give e.g. high compactness or high average power. This versatility often makes DPSSLs an attractive choice when designing laser systems. The thesis will focus on DPSSLs where the active ion is either Er^{3+} or Yb^{3+}.

Er^{3+}-doped solid-state laser systems are very attractive due to their emission at 1.54 µm, which is considered eye-safe. In the case of laser radiation impacting on a human eye, this wavelength is absorbed by OH^- groups in the eye thereby avoiding a high intensity focus on the retina. On the other hand, the transmission in the atmosphere is excellent since there is a wide transmission window between 1.5-1.75 µm. These two properties together make Er-doped lasers ideal in situations which include free-space propagation in a non-laboratory environment, such as LIDAR (Light Detection And Ranging) and range-finding. Furthermore, the strong absorption in human tissue is very suitable for certain forms of micro-surgery.

In Er-doped lasers operating around 1.54 µm, the laser transition occurs between the $^4I_{13/2}$ and the $^4I_{15/2}$ energy levels in Er^{3+} ions. As the $^4I_{15/2}$ level is also the ground state, the threshold increases rapidly with dopant concentration. At the same time, the absorption cross section in erbium is quite low, which calls for high concentrations in order to obtain efficient absorption of the pump light. This trade-off between low threshold and high absorption is solved by adding Yb^{3+} ions to the system. Pump light is then absorbed by the ytterbium ions and subsequently transferred to erbium. However, this constitutes a rather complex laser system whose efficiency is strongly dependent on the host material.

The first Er-Yb laser system was constructed in 1965, using a flashlamp-pumped Er,Yb-codoped glass rod.[2] Ever since, glass has been the dominating host material for Er-Yb systems due to the advantageous lifetimes for both Yb $\rightarrow$ Er energy transfer and Er lasing. The glass host material has been optimized throughout the years,[3] but still the average output power is limited by the low thermal conductivity of glass. A lot of effort has been put into the search for a suitable crystalline

replacement with better output performance,[4-7] but this has proved very challenging. Still, promising new results have been achieved using borate crystals.[8,9]

In a solid-state laser using Yb^{3+} as the active ion, the energy level system becomes much simpler. In fact, one of the major advantages of Yb-doped lasers is that the only relevant states are the $^2F_{5/2}$ and the $^2F_{7/2}$ levels with their respective Stark levels. This effectively excludes problems such as excited-state absorption (ESA) and upconversion (UC). Together with an extremely low quantum defect, this results in high slope efficiencies under both Ti:sapphire[10] and diode pumping.[11] Another advantageous feature of Yb-doped materials is the similarity of ionic radii between Yb^{3+} and common substitution ions in the host material lattice. This leads to an acceptance of high dopant concentrations without any serious quenching, especially when the Yb^{3+} ion goes into yttrium sites.[12,13] These properties have enabled efficient thin-disc lasers both in the continuous-wave regime (cw)[14] and in the mode-locked regime.[15]

Although Yb^{3+}-doped lasers first appeared already in 1964,[16] real interest in these systems exploded in the late 1990's with the arrival of high-power semiconductor lasers that could truly exploit the low quantum defect of the ytterbium system. Today, one of the main research areas is related to the improvement of thermal management of the lasers to reach ever higher output powers. This can be done by altering the shape of the active element to increase the surface-to-volume ratio, either by minimizing the length in a thin-disc design[14] or by maximizing it in a fiber laser design.[17] To some extent, it can also be done by insertion of an intracavity element that compensates for thermal effects.[18] An alternative in some crystals with a negative dn/dT is instead to alter the crystal orientation so that the laser beam propagates along a direction where the thermal expansion and thermooptic effect cancel each other.

The wide emission spectra of Yb-doped materials have made them popular for use in femtosecond laser systems. A drawback of the same property is that Yb lasers often show a large bandwidth if no spectrally discriminating component is added to the cavity. Traditionally, there are several possibilities such as etalons, Lyot-filters and prisms. Recently, another possibility has emerged, the volume Bragg grating (VBG). [19] A VBG is a piece of photosensitive glass, typically a few millimeters thick, into which a sinusoidally varying refractive index modulation is written. The result is a potentially high reflectivity of > 99% in combination with a narrow bandwidth in the order of ~100 pm. Moreover, the reflectivity and bandwidth values are not firmly coupled, so it is possible to engineer almost any combination. Another advantageous property is that there is an unlimited spectral range, i.e. the peak reflectivity occurs at a single wavelength and does not repeat itself periodically. VBGs have been used previously to lock the wavelength of semiconductor lasers,[20] Nd lasers,[21] Er-Yb lasers[22] and Ti:sapphire lasers[23] as well as optical parametric oscillators (OPOs).[24]

A common group of host materials for Yb lasers are the double tungstates. These are biaxial crystals, which means that they exhibit a rare phenomenon known as conical refraction. Conical refraction is a special case of the common double refraction that occurs when light travels along one of the two optic axes. While in double refraction the two orthogonal polarizations travel along different paths in the crystal, in conical refraction every single polarization state has its own path. For example, at normal incidence for unpolarized light, the beam inside the crystal propagates as a cone and on the output surface it forms a ring instead of the two characteristic spots of double refraction. The phenomenon was first proposed by Hamilton in 1832[25] and in addition to the early work of Poggendorff[26] it has been further studied in modern times by several groups.[27-30] Still, there have been few, if any, practical applications.

1.2 Development of the work

The thesis work started with research into gadolinium-calcium oxoborate, $GdCa_4O(BO_3)_3$ or GdCOB for short, as host material for Er,Yb-doped lasers. This was done in close co-operation with the group of Boris Denker at the General Physics Institute (GPI) in Moscow. A borate crystal was chosen due to the high phonon cut-off energy, hopefully resulting in suitable lifetimes of the energy levels, and also due to the promising recent international progress with such crystals, especially with YCOB.[9] GdCOB in particular was chosen since it is very convenient to grow and, as opposed to e.g. YCOB, could be

grown from the available platinum crucibles. Using a Ti:sapphire pumped monolithic laser design, we obtained 70 mW output power at 15% slope efficiency in cw.[I] In the Q-switched regime, we used a pulsed high-power diode-bar to overcome the high threshold of GdCOB together with the added saturable loss of the spinel Q-switch. We also used a shorter crystal to improve the mode overlap and reduce reabsorption and finally arrived at a maximum output power of 88.2 mW.[II] The slope efficiency in this case was 11.6 % and the pulses were 5-6 ns long. As a comparison, one of the best monolithic glass lasers has produced 150 mW at 19 % efficiency.[3]

While the above results are quite good for crystalline hosts and constitutes the first experiments on passive Q-switching in Er,Yb-doped crystals, they cannot compete with the best glass lasers. Even though these are only initial experiments it seems that, judging from the fracture limit and threshold, the outlook for GdCOB to replace glass looks limited. So instead we initiated spectroscopic studies of other host materials. As a part of the EU-project DT-CRYS, double tungstates were investigated.[III] Also, in co-operation with the group at GPI, an unorthodox approach was tested where Er,Yb:YAG crystals were heated several hundred degrees.[IV] At this temperature, our measurements showed that the lifetimes become similar to those in glass while the thermal conductivity is about 5 $WK^{-1}m^{-1}$, significantly higher than in glass. It also seems that gain should be possible despite the increased thermal population and reduced thresholds. However, this gain is strongly reduced and the practical problems with a heated gain medium make it difficult to imagine this as more than an interesting curiosity.

Under the EU-project DT-CRYS, parallel experiments were made with Yb-doped double tungstate lasers. Our first priority was to investigate if the thermal lens could be reduced in a properly oriented $KGd(WO_4)_2$ (KGW) crystal since the thermo-optic coefficient is negative in this material. Towards this goal, we first had to construct an efficient reference laser with the standard b-cut orientation. The maximum output power was 9.3 W using as pump source a high-power, non-fiber-coupled diode bar focusing 19.3 W at 980 nm into a ~100 µm spot. This performance was limited by available pump power. To increase pump power, a 50 W fiber-coupled diode bar at the Max-Born Institute in Berlin was used. With this pump the output power rose to 12.4 W before crystal fracture. The optical efficiency was 47% in both cases.[V] Now, the b-cut crystal was replaced by the athermally oriented crystal, cut for propagation along an axis at 17° angle from the dielectric axis $\mathbf{N_m}$. This orientation gives access to the dielectric axis with lowest threshold, $\mathbf{N_p}$, but not the axis with the best absorption, $\mathbf{N_m}$. This limited the output power to 4 W, but at the same slope efficiency in terms of absorbed power. Using a probe beam at 532 nm to measure the thermal lens, we found that in our experiments the rate of thermal lens increase was almost halved using the athermally oriented crystal.[VI]

During these measurements we also made some tuning experiments using an etalon, but the tuning range was limited due to the limited spectral range of the etalon. At the same time, several experiments were made in our group using VBGs. It seemed suitable to use these devices to lock and tune the wavelength of the laser. To enable extensive laser tuning with Bragg gratings, for the first time to our knowledge, the grating was placed in a retroreflector design.[31] However, at first we obtained very disappointing results and the beam through the grating looked strange. This behavior was different from the earlier Bragg-locked lasers of our group, which used normal incidence as opposed to the oblique incidence of the retroreflector setup. This incited us to read earlier articles on the theory of VBGs, to compose and develop this theory into a form more suitable for our application and to make a series of experiments into the relevant, fundamental workings of VBGs.[VII] Based on this investigation, we were able to redesign the laser cavity and achieved much improved results. The tuning range was from 997 to 1040-1050 nm, depending on the configuration, with a laser bandwidth of 10 GHz. The maximum output power was 3 W, and by positioning the VBG for normal incidence, without the retroreflector, the same output power could be obtained at 1063 nm as well.[VIII, IX] At shorter wavelengths below 1000 nm, however, the output power drops rapidly due to the increasing transmission of the input coupler. At the same time, if still shorter wavelengths can be reached, the quantum defect would be extremely low and the result can be considered a quasi-two-

level laser. This prompted us to use a VBG, at normal incidence, as input coupler. With this design, we obtained an output power of 3.6 W at 998 nm.[X] The threshold is relatively high, 7 W of absorbed power, and the absorption is reduced due to ground-state depletion. Still, the slope efficiency versus absorbed power is almost 60% and the quantum defect is only 1.6%. Considering the fracture limit experienced in the Berlin experiments, it should be possible to reach output powers of more than 20 W using this laser design.

Finally, we wanted to redo the experiments on the athermally oriented crystal with an athermal crystal orientation that allowed for the pump polarization to be along the $\mathbf{N_m}$ direction. We found such an orientation to be approximately along one of the optic axes. At first, we were confused by the results and the seemingly random polarization. Then, we recalled that the crystal suppliers had mentioned that the propagation direction could exhibit conical refraction. Gradually, by experiments and studies of articles on the phenomenon we learned how to use the conical refraction to control both the polarization direction and the extinction ratio.[XI] At the same time, we maintained an output power of about 8.5 W at 60% slope efficiency with respect to incident pump power. A side-effect, though, was that this exciting phenomenon drew our efforts away from the intended experiments on the athermal behavior, which have been postponed until later.

1.3 Outline of the thesis

This thesis summarizes the research presented in the articles I – XI. The chapters are organized to roughly follow the timeline of the research, starting with the earliest work. The common point for all chapters is lanthanide doped solid-state lasers. Therefore, the thesis begins with an introduction to the theory for such devices, given in Chapter 2. This chapter presents the basic physics behind the energy level schemes of doped crystals and how these can be used to build solid-state lasers, as well as some factors that influence the performance of these lasers.

Chapter 3 discusses the Er-Yb laser and the use of crystalline host materials in order to improve the thermal management of it. Specifically, the results obtained with Er,Yb:GdCOB are presented as well as spectroscopic investigations into Er,Yb-doped tungstates and Er,Yb:YAG. Chapter 4 presents high-power results for end-pumped Yb:KGW as well as experiments using athermally oriented crystals to reduce the thermal lensing. In Chapter 5, these Yb:KGW lasers are further treated, but this time in combination with VBGs to establish spectral control. The chapter begins with a theoretical treatment of these gratings applied to laser cavities and then turns to handle the construction of a tunable Yb:KGW laser with narrow bandwidth. Furthermore, the chapter discusses the possibility to utilize VBGs to achieve a quasi-two-level laser. Chapter 6 introduces polarization tuning of biaxial crystals using internal conical refraction. A brief background to the phenomenon is given and experimental results using Yb:KGW are presented. Finally, the work is concluded in Chapter 7 and the author's contribution to the articles is described in Chapter 8.

Chapter 2
Aspects of solid-state laser theory

2.1 Ion energy levels and photon interaction

All lasers are based on the stimulated emission process. The fundament of this process is electron, ion or molecule transition between two states with different energies, $E_j > E_i$, which is stimulated by a photon of energy $E_L \approx E_j - E_i$. From the released energy, a second photon is created that is an exact clone of the first photon, i.e. it has the same energy, the same phase, the same polarization and the same propagation direction. In lanthanide doped solid-state lasers, the transitions involved in the stimulated emission process concern electrons situated in the incompletely filled 4f shell and these electron transitions occur between different states of this shell. Since all the orbitals of this shell have the same parity, such transitions are forbidden due to the selection rules for an unperturbated system. Despite this, the transitions may occur, because of coupling with the crystal field and other electrons. Still, the oscillation strengths are much weaker than for allowed transitions, which makes the lifetimes long enough to be suited for laser operation.

In a basic model of a free ion, the different states within the 4f shell would be degenerate. However, coupling between the angular momenta and the spins of the different electrons occupying sites in the 4f shell causes the states to split into different energy levels. These energy levels are usually written in the form $^{2S+1}L_J$. Here, S is the total spin quantum number, L is the resultant orbital angular momentum of the state and J is the total angular momentum resulting from the vector addition S+L. Furthermore, the host material will cause the dopant ions to experience a local electric field. This electric field will split these energy levels further because of the Stark effect. Each $^{2S+1}L_J$ energy level will be split into J+1/2 sublevels called Stark levels. The different sublevels of each $^{2S+1}L_J$ level are usually much closer to each other than to the neighboring $^{2S+1}L_J$ levels. Also, phonon-assisted thermalization rates between the population densities of different Stark levels are usually so fast compared to other processes that it can be considered instantaneous. On the other hand, phonon-assisted redistribution rates between the population densities of different $^{2S+1}L_J$ levels can be of the same order of magnitude as the spontaneous emission or even slower.

Apart from the stimulated emission process described above, two other electron-photon interactions are possible between the two different energy levels E_j and E_i. The first is the absorption process, where a photon of energy E_L is absorbed by an ion with an electron in the lower energy state, exciting it to the higher energy state. The second is the spontaneous emission process, where an electron in the higher energy state spontaneously de-excites into the lower energy state and emits a photon of energy E_L with random phase and random propagation direction. The latter emission process can also be thought of as stimulated emission of quantum noise.

The probability function for an electron-photon interaction to occur is not a discrete spike at a fixed wavelength. Instead, it is broadened with regard to the wavelength λ into a lineshape function $g(\lambda)$. This broadening occurs due to the temporal and spatial dependence of the transition energy $E_j - E_i$. The mechanisms behind this can be homogeneous, in which case the interaction with a photon at a certain wavelength will not reduce the relative interaction probability for photons with the same wavelength. An example of such a broadening mechanism that occurs in all solid-state laser materials is crystal lattice vibrations, where a phonon is absorbed or emitted simultaneously with the

stimulated emission process and the phonon energy is added to or subtracted from the photon energy. In the case of inhomogeneous broadening, on the other hand, the interaction with a photon will reduce the possibility of interaction with another photon with the same wavelength. In the end, this may lead to so-called spectral hole burning where stimulated emission severely reduces the population inversion at a certain wavelength region only. An example of inhomogeneous broadening is non-equivalent lattice sites for the active ions.

If the population density, N_j, in a state with energy E_j is higher than the thermal equilibrium population, spontaneous emission into lower energy states will cause an exponential decay of the population. The time-constant of this decay, τ_{Rj}, is called the radiative lifetime of that state. It should be noted that the population also decreases exponentially due to phonon relaxation, where a phonon is emitted instead of a photon. The time-constant of phonon relaxation, τ_{NRj}, is called the nonradiative lifetime. The larger the bandgap, $\Delta E = E_j - E_i$, is compared with the energy of the present phonons, the longer τ_{NRj} will be. Finally, the total or fluorescent lifetime of the jth level, τ_j, is given by the expression $1/\tau_j = 1/\tau_{NRj} + 1/\tau_{Rj}$.

2.2 Intensity amplification

The probabilities for the absorption and stimulated emission processes are governed by the cross-sections, σ_{ij} and σ_{ji}, for the respective process. Through perturbation calculations, it is possible to state that[32]

$$\sigma_{ji}(\lambda) = \frac{\eta\lambda^4}{8\pi n^2 \tau_{Rj} c} g(\lambda). \tag{2.1}$$

Here, n is the refractive index, c is the vacuum speed of light and η is the ratio, typically close to 1, between the overlap of the two states' wavefunctions in the photon polarization direction and the averaged overlap in all three orthogonal directions. In this cross-section modeling of reality, each ion is seen as having a capture area equaling the cross-section. If a photon propagates through this area and the ion has an electron in a relevant state, it will cause absorption or stimulated emission respectively. A beam with intensity I passing through a suitably doped material of length L will therefore experience an amplification or decay proportional to the ratio between the total capture area of all ions and the beam cross-section. This can be written as:

$$dI = [N_j\sigma_{ji} - N_i\sigma_{ij}]\cdot I \cdot L. \tag{2.2}$$

Here N_x is the population density of state E_x. The emission and absorption cross-sections of a certain transition are related through $\sigma_{ji} = (g_i/g_j)\sigma_{ij}$, where g_x is the degeneracy of the state with energy E_x. It is obvious from Eq. 2.2 that in order to amplify the intensity, $N_j\sigma_{ji}$ has to exceed $N_i\sigma_{ij}$ or equivalently N_j has to exceed $N_i \cdot g_j/g_i$. This situation is called population inversion and in solid-state lasers it is achieved through optical pumping, i.e. exciting the electrons by absorption of photons from an external pump source. From Eq. 2.2 it can also be seen that once N_j equals $N_i \cdot g_j/g_i$ the intensity will neither increase nor decrease and the beam will be neither absorbed nor amplified. Thus, optical pumping directly from state E_i to state E_j is impossible because once transparency is reached, the additional absorption required for the stimulated emission process to dominate over absorption will not occur, i.e. the absorption has been saturated.

Instead, optical pumping from state E_i to a higher energy state $E_k > E_j$ is typically utilized. The state E_k should have a fast relaxation rate so that the excited electrons rapidly decay to E_j through phonon relaxation. Furthermore, population inversion will be reached much easier if the state E_i has a negligible population at thermal equilibrium. In this case, naturally, the electrons have to be excited from a fourth state, the ground state, with energy $E_0 < E_i$. Such a system is called a four-level laser system. If, however, E_0 and E_i are just different Stark levels of the same $^{2S+1}L_J$ level, so that thermal population of E_i becomes important, then the system is considered a three-level laser. Moreover, if $E_k = E_j$ in a three-level laser while the difference between E_0 and E_i is extremely small, then the system might be called a quasi-two-level laser. A generalized optical pumping scheme is given in Fig. 2.1.

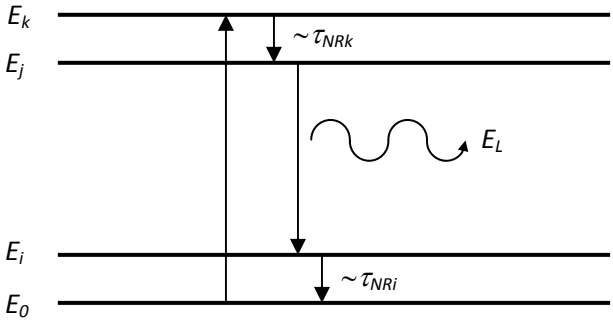

FIGURE 2.1: The optical pumping scheme.

An important parameter of the pumping scheme is the quantum defect, Q_D. This is the percentage of the pump photon energy that is inevitably wasted in the pumping process, i.e. $Q_D = 1-E_L/(E_k-E_0)$. Generally, as is outlined above, this energy is turned into phonons, which is equivalent to heating the material. Therefore the quantum defect not only limits the general optical-to-optical power efficiency of the laser, but it also limits the maximum output power that can be achieved before thermal effects start decreasing the laser efficiency and possibly even fractures the laser material, see Section 2.6.

In order to make a practical laser model, it is common to use the effective emission and absorption cross sections, $\sigma_e(\lambda)$ and $\sigma_a(\lambda)$, respectively. In this approach, the effect of population distribution between different Stark levels have been taken into account to create cross sections that can be used with regard to the total population of the $^{2S+1}L_J$ energy level. Note that if this approach is applied to Eq. 2.2, population inversion between two energy levels can be achieved through optical pumping if $N_j\sigma_e(\lambda) > N_i\sigma_a(\lambda)$ for one wavelength but the inverse is true for another, shorter wavelength. This situation would arise in a laser where E_k and E_j in Fig. 2.1 are two different Stark levels as are E_i and E_0.

As long as the absorption loss is much higher than all other loss sources of the experiment, the effective absorption cross section can be relatively easily measured. Basically, it is sufficient to illuminate a sample with light and then measure the transmission loss as a function of wavelength and polarization. The effective emission cross section can then be found through the reciprocity method:[33]

$$\sigma_{\mathrm{e}}(\lambda) = \sigma_{\mathrm{a}}(\lambda)\frac{Z_{\mathrm{i}}}{Z_{\mathrm{j}}}\exp\left[\frac{(E_{ij}-{}^{hc}/_{\lambda})}{k_B T}\right]. \tag{2.3}$$

Here, Z_i and Z_j are the partition functions of the lower and upper laser level, respectively, h is Planck's constant, k_B is Boltzmann's constant and T is the temperature. E_{ij} is the zero-phonon transition energy between the two laser levels. An alternative method to find the emission cross section is by exciting the sample, collecting the fluorescence and then using the Füchtbauer-Ladenburg formula:[34]

$$\sigma_{\mathrm{e}}(\lambda) = \frac{\lambda^5 \eta_{\mathrm{r}} I(\lambda)}{8\pi n^2 c \tau_j \int \lambda \cdot I(\lambda)\mathrm{d}\lambda}. \tag{2.4}$$

In Eq. 2.4, $\eta_r = 1-\tau_j/\tau_{NRj}$ is the radiative quantum efficiency and $I(\lambda)$ is the measured fluorescence intensity. In spectral regions where absorption is strong, $I(\lambda)$ might be influenced by reabsorption. It might thus be argued that Eq. 2.3 is preferable where absorption is strong, while Eq. 2.4 is preferable where absorption is weak. Note also that since the shape of $\sigma_e(\lambda)$ follows $I(\lambda)$ closely, it is possible to get a good estimation by simply fitting a single point of the normalized $\lambda^5 I(\lambda)$ curve to a known numerical value of σ_e.

2.3 Rate equations and laser modes

Except for special cases, e.g. at cryogenic temperatures, phonon relaxations from E_k to E_j in Fig. 2.1 and from E_i to E_0 are so fast in comparison with other processes that they can be considered instantaneous. Furthermore, the upper and lower laser levels (E_j and E_i in Fig. 2.1, respectively) are often so far apart that spontaneous emission dominates over phonon relaxation. It then follows that the latter can be neglected. These simplifications are assumed to hold in the following discussion.

The fraction of the incident optical pump power actually being absorbed in the laser material is the absorption efficiency, η_a. If the pump is a laser beam that makes a single-pass through the material, as is the case in the experiments of this thesis, η_a = 1-exp(-αL), where the absorption coefficient is given by $\alpha = N_0 \cdot \sigma_a(\lambda)$. Out of this absorbed pump power, only a fraction η_p will actually result in an excited electron at the upper laser level. Using a pump with a small bandwidth, as in the experiments within this thesis, η_p can be close to one while using a broad bandwidth source such as a flashlamp or having losses at the E_k state in Fig. 2.1 will reduce η_p significantly. Assuming a pump source with a small bandwidth that is emitting at wavelengths around λ_p and using the expression for photon energy $E = hc/\lambda$, the density of the pump-rate into the upper laser level can be written as:

$$R_{\mathrm{p}}(x,y,z) = \frac{\lambda_{\mathrm{p}} \cdot \eta_{\mathrm{a}} \cdot \eta_{\mathrm{p}} \cdot P_{\mathrm{p}}}{h \cdot c} r_{\mathrm{pump}}(x,y,z), \tag{2.5}$$

Here P_p is the total pump power and r_{pump} is the normalized spatial distribution function of the absorbed pump power in the material. Apart from adding electrons to the upper laser level, pumping may also remove them from the lower laser level. If the thermal population of the lower laser level is a fraction f_l of the ground state population then the depletion of its population due to pumping will be $R_p \cdot f_l$. This fraction is given by the Boltzmann distribution as f_l = exp[-$\Delta E/k_B T$] where ΔE is the energy difference between the ground state and the lower laser level. Note that in a three-level laser, when the lower laser level and the ground state are within the same $^{2S+1}L_J$ energy level, f_l will be equal to one in the effective cross-section approach used in the following models. In most four-level lasers, on the other hand, it will be approximately zero.

A laser mode is any temporal and spatial distribution of the electro-magnetic field, transversal to the propagation direction, which reproduces itself at the same spot in the cavity after propagating one round-trip. $\gamma_{rt}(\lambda)$ is the mode's exponential loss coefficient for each round-trip and τ_{rt} is the duration of each round-trip. To control which modes are possible, mirrors with suitable radii of curvature are placed in suitable positions according to ABCD-matrix calculations. These mirrors impose boundary conditions on the circulating electric field. The temporal boundary conditions determine the longitudinal modes while the spatial boundary conditions determine the transversal modes.

The most common transversal modes in solid-state lasers are the Hermite-Gaussian modes. A complete set of normalized mode functions for such a beam propagating along the *z*-axis in free space is given, in one transverse direction *x*, by:[35]

$$u_m(x,z) = \left(\frac{2}{\pi}\right)^{1/4} \left(\frac{1}{2^m m! w_0}\right)^{1/2} \left(\frac{\tilde{q}_0}{\tilde{q}(z)}\right)^{1/2} \left[\frac{\tilde{q}_0 \tilde{q}^*(z)}{\tilde{q}_0^* \tilde{q}(z)}\right]^{m/2} \times H_m\left(\frac{\sqrt{2}x}{w(z)}\right) \exp\left[\frac{-jkx^2}{2\tilde{q}(z)}\right], \tag{2.6}$$

$$\frac{1}{\tilde{q}(z)} = \frac{1}{R(z)} - j\frac{\lambda}{\pi w^2(z)}, \tag{2.7}$$

$$\frac{d\tilde{q}(z)}{dz} = 1. \tag{2.8}$$

Here, *m* is the transverse mode number, H_m is the respective Hermite polynomial, *k* is the wave number, *w*(*z*) is the beam radius (1/e^2) and *R(z)* is the radius of curvature. While Eqs. 2.6-2.8

can be used to describe the spatial distribution of any Hermite-Gaussian beam in detail, the beam propagation is often estimated by a divergence angle for simplicity. This divergence angle is connected with the spatial beam quality, which is commonly measured using the beam propagation factor $M^2 = (\pi/\lambda)\cdot w_0\theta$, where w_0 is the beam waist radius and θ is the divergence angle. A higher M^2-value results in a worse beam quality because the divergence and the focused spot diameter both scale with M^2 and the beam is said to be M^2-times diffraction limited. A Hermite-Gaussian mode as outlined above has an M^2-value of $2m + 1$ in the x-direction.

While the transversal modes set the spatial beam quality, the longitudinal modes define the spectral bandwidth. Each longitudinal mode is associated with a specific wavelength that gives a standing wave fulfilling the boundary conditions. As a consequence, a typical cavity defines the longitudinal modes through $L_c = j\lambda/2$, where L_c is the optical length of the cavity and j is the longitudinal mode number (1, 2, 3…). It then follows that the mode spacing is given by $\Delta\lambda = \lambda^2/2L$.

Now, referring to the upper laser level as level 2 and the lower laser level as level 1, the rate equations that govern the temporal dynamics of the populations of these levels as well as the intensity and power for a certain transverse laser mode m and a longitudinal mode at wavelength λ becomes:

$$\frac{dN_2(x,y,z)}{dt} = R_p(x,y,z) - \frac{N_2(x,y,z)}{\tau_2} - \sum_m \sum_\lambda \left[\sigma_e(\lambda)N_2(x,y,z) - \sigma_a(\lambda)N_1(x,y,z)\right]\cdot \frac{\lambda \cdot I_{m\lambda}(x,y,z)}{hc}, \tag{2.9}$$

$$\frac{dN_1(x,y,z)}{dt} = \begin{cases} -\dfrac{dN_2(x,y,z)}{dt}, & (f_l = 1) \\ \beta_{21}\dfrac{N_2(x,y,z)}{\tau_2} - \dfrac{N_1(x,y,z)}{\tau_1} + & \\ \displaystyle\sum_m \sum_\lambda \left[\sigma_e(\lambda)N_2(x,y,z) - \sigma_a(\lambda)N_1(x,y,z)\right]\cdot \frac{\lambda \cdot I_{m\lambda}(x,y,z)}{hc}, & (f_l = 0) \end{cases} \tag{2.10}$$

$$\frac{dP_{m\lambda}}{dt} = \frac{A}{\tau_{rt}} \iiint \left[\sigma_e(\lambda)N_2(x,y,z) - \sigma_a(\lambda)N_1(x,y,z)\right]\cdot I_{m\lambda}(x,y,z)dV - \frac{\gamma_{rt}}{\tau_{rt}} P_{m\lambda}, \tag{2.11}$$

$$I_{m\lambda}(x,y,z) = P_{m\lambda} \cdot u_m(x,z) \cdot u_m^{'}(y,z). \tag{2.12}$$

Here the sums in Eqs. 2.9-2.10 are supposed to be taken over all possible modes and wavelengths. u_m and u_m' are the normalized mode functions in the two orthogonal transversal directions and A refers to the number of passes through the laser material during one round-trip, i.e. 1 for a ring cavity and 2 for a standard double-pass cavity with two end-mirrors. $\gamma_{rt}(\lambda)$ and τ_{rt} are the mode's exponential loss coefficient and the duration of each round-trip, respectively. β_{21}, finally, is the branching ratio from level 2 to level 1, i.e. the amount of spontaneous decay from level 2 that end up in level 1 relative the total spontaneous decay from level 2. In these equations, the intensity variations of the oscillating field along the z-direction is assumed to follow the cavity mode, which is approximately true for low output coupling.

It is evident that it is necessary to keep $\gamma_{rt}(\lambda)$ low for the desired transversal and longitudinal mode. However, N_2 also decreases due to stimulated emission into other modes. As this constitutes a loss of excited electrons, stimulated emission into other modes must be kept low. Because

stimulated emission is proportional to intensity, this can be achieved by maximizing γ_{rt} for all undesired modes. In this way, control of the laser emission is established by controlling losses.

When threshold is reached, i.e. when N_2 is large enough for the stimulated emission to equal the losses for a certain mode so that lasing starts, the populations become clamped. This means that, in theory, N_2 remains fixed when R_p is increased. Mathematically, this states that Eq. 2.9 should be equal to zero when R_p is increased, which is accomplished by increasing $I_{m\lambda}$, namely the intensity in the lasing mode. Thus once threshold is reached for a certain mode, further increase of the pump power will cause the intensity of that mode to increase linearly. Because N_2 is not further increased, no other modes will reach threshold. However, the intensity in the wings of the lasing mode is limited by the mode structure and the peak intensity. If the pump mode is significantly larger than the lasing mode, $I_{m\lambda}$ in the wings will not be strong enough to saturate the gain and N_2 will continue to rise. This might enable higher-order modes to reach threshold with increased pump powers. The addition of higher-order modes with increased pump power might be supported by thermal lensing that changes the spatial boundary conditions.

To avoid the onset of undesired transversal modes, the spatial distribution of R_p should match the intensity distribution of the desired mode. If this is not sufficient, it is possible to place an element with transversally varying losses inside the cavity, such as a pinhole. Often the desired mode means the fundamental Gaussian mode TEM_{00}, but a TEM_{00} single transversal-mode operation might not always be optimal. Even though multi-mode operation degrades the beam quality, it is often more efficient in extracting the energy of the pumped laser medium. Also, a single higher-order mode might be the best choice for overlap between pump and laser modes. To maximize the brightness, for example, there will be a trade-off between beam quality and output power.

Regarding longitudinal modes, these are often so close to each other in terms of losses and emission cross sections that several modes will have almost the same thresholds and will, therefore, lase simultaneously. To reduce the number of longitudinal modes, as well as to set the center frequency, an element with different losses for different longitudinal modes is introduced in the cavity, such as an etalon, a prism or a VBG. Since the mode spacing is inversely proportional to the cavity length, single longitudinal mode operation tends to be more easily obtained in short lasers.

2.4 Output performance

For the common case where the pump beam has a Gaussian transversal intensity distribution of radius w_p and the laser cavity mode is also Gaussian with width w_c, the lasing threshold and slope efficiency, dP_{laser}/dP_{pump}, is given by[36]

$$P_{th} = \frac{\pi(w_p^2 + w_c^2)hc}{4\sigma_e \tau_2 \eta_a \lambda_p}\left[T_{OC} + L + 2(1 - \exp(-\sigma_a N_1 l))\right], \tag{2.13}$$

$$\eta_{slope} = \frac{T_{OC}}{\gamma_{rt}} \frac{\lambda_P}{\lambda_L} \eta_a \eta_p \eta_{PL}. \tag{2.14}$$

Here, T_{OC} is the output coupler transmission and η_{PL} is the overlap efficiency between the pump and laser modes. It should also be stated that the above formulas refer to incident pump power. Quite often, the threshold and slope efficiency are given referring to absorbed pump power in which case the term η_a should be removed from Eqs. 2.13 and 2.14. Similarly, the optical efficiency, i.e. the output-to-input power ratio, can be referring to both absorbed and incident power. The preferred reference power depends on the message; incident power often tells more of the actual laser system while absorbed power might give a better picture of the final potential of a method, material or design.

In an ideal laser, the total output power is well defined by the equation $P_{tot} = \eta_{slope}(P_p - P_{th})$. However, in practice many lasers tend to exhibit a slope efficiency that varies with pump power. This is especially true for three-level lasers. There are several reasons for this behavior. One example is

that the wavelength of the pump tends to vary with pump power, thus varying η_a. This mostly concerns semiconductor pump sources. Another reason is that the thermal lens might change the mode conditions, thus changing η_{PL} and frequently also the number of lasing modes. Furthermore, in long three-level lasers initial reabsorption loss by the end of the crystal where R_p is not strong enough to cause population inversion may be removed at higher pump powers. This is equally true for the wings of the transversal pump intensity distribution. In the end, for high pump powers, severe thermal effects will usually limit the slope efficiency. This is sometimes termed thermal roll-off.

2.5 Loss mechanisms

The output coupling is experienced as a loss by the oscillating laser field inside the cavity. Apart from this beneficial loss, there are several parasitic sources that cause loss of either pump power, laser power or both. Examples such as defects in the laser material or non-ideal coatings will not be further discussed here. Instead, this section will focus on the loss mechanisms that are inherent properties of the laser material.

Upconversion (UC) is one such loss source. In an upconversion process, two electrons of separate ions with about the same energy resonantly interact so that one is de-excited to a lower energy state whereas the other is excited to a higher energy state, E_m. In some cooperative upconversion processes, even more electrons may take part in the transfer process so that several electrons are de-excited to provide excitation energy for another electron. The upconversion process is illustrated in Fig. 2.2.

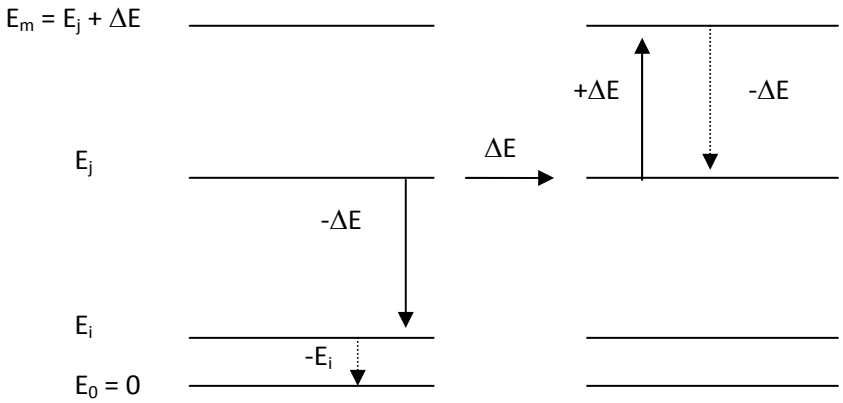

FIGURE 2.2: An example that illustrates the upconversion process. The decay from E_i to the ground state, as well as the decay from the higher energy level E_m to E_j, may be divided into several steps.

The upconversion process constitutes a problem mainly as a loss source for electrons in the upper laser level. In most cases, the electron that is excited to E_m rapidly decays back to the upper laser level. The other electron, however, continues to decay until it reaches the ground state. The net result is one lost excited electron, equivalent to one lost pump photon. To make matters even worse, the lost energy has generally been turned into heat. Since the combined energy of the two electrons was $2 \cdot E_j$ before the upconversion and only E_j after the upconversion and the subsequent decay, the net heating equals the upper laser level energy.

In modeling the upconversion, the loss rate of excited electrons, dN_2/dt, can be considered to equal a constant C times N_2^2. Because of the squared dependence on N_2, upconversion becomes an increasing problem at higher doping levels and will finally limit the maximum achievable inversion. The constant C is dependent on the ion-ion distance in the material, because a closer distance increases the chance for interaction, which is why it increases with the dopant concentration. Note finally that there has to exist a suitable energy level for upconversion excitation in order for the process to take place. In Yb-doped materials for example, no such level exists and the traditional view is that upconversion should not be an issue. Still, recent research suggests that cooperative

upconversion to a charge transfer band might be an important issue in certain highly-doped materials.[37]

Finally, it should be stated that upconversion is not always a problem. It can be used to build upconversion lasers, such as thulium-doped lasers[38] or erbium-doped lasers operating around 3 µm.[39] In certain lasers the weak light from the spontaneous emission in the decay following the upconversion process can be very helpful when aligning the laser. It makes it possible to visualize the pump beam passing through the crystal and it helps in finding optimal focusing because the luminescence is proportional to the square of the absorbed power. It also fades when the cavity is properly aligned, because population in the upper laser level is lower under lasing conditions compared to non-lasing conditions for the same pump power.

Another problem may be excited state absorption (ESA). In this case a laser photon is absorbed by an electron that is already in the upper laser level. The electron is excited and subsequently, as in the case of upconversion, returns through phonon relaxations or spontaneous emission. The net result is the loss of one laser photon which is often turned into heat. ESA can be modeled as a standard absorption loss with a cross-section σ_{ESA}, i.e. $dN_2/dt = \sigma_{ESA} \cdot N_2 \cdot I$. Again, there has to exist a suitable energy level for ESA excitation in order for the process to take place. Yb-doped systems once again prove beneficial, in that no such level exists and ESA is not an issue.

Quenching of the upper laser level lifetime might be a problem in some materials at high doping concentrations. Quenching as a term can refer to many different processes, here it refers mainly to energy migration between ions and between ions and defects. At higher concentrations, energy transfers more easily from ion to ion and finally to a defect where it is lost. In this way, quenching limits the maximum dopant concentration for effective lasing in some laser materials.

2.6 Thermal issues

With the exception of laser cooling systems, where the pump photon energy is lower than the average fluorescence photon energy, the laser material is inevitably heated during the laser process. This heating stems primarily from the phonon relaxation in the pump scheme, see Fig. 2.1. It follows that the heat load, $H(x,y,z)$, is approximately equal to $Q_D \cdot \eta_a \cdot P_p \cdot r_{pump}(x,y,z)$. This gives a heat load distribution that follows the pump distribution and that is proportional to the quantum defect, two important statements. It is also important to note that the heat load generally differs between lasing and non-lasing conditions. There are two main reasons for this. First, under non-lasing conditions, the population in the upper laser level is larger for the same pump power and as a result there will be more nonradiative decay from this level and from upconversion. Second, under non-lasing conditions, the emission is governed by the fluorescence which usually has a different average wavelength than the lasing and thus a different quantum defect. Another heat source is the nonradiative decay from the upper laser level. In most systems, this can be neglected but for a system with high population inversion and low quantum defects, it becomes a significant contribution to the heat load. Such a system will be discussed in Section 5.3.

While the heating never leads to such temperatures that the material actually melts, except in extreme cases, the problems associated with heating arise from the non-uniform temperature distribution that follows the non-uniform cooling and heating inside the laser medium. Fig. 2.3 shows the predicted temperature gradients in a $3\times3\times3$ mm^3 Yb:KGW crystal, similar to the crystals used in Chapters 4-6. The maximum temperature gradient becomes $1.1\cdot10^5$ K/m while the maximum local temperature is limited to 55 °C.

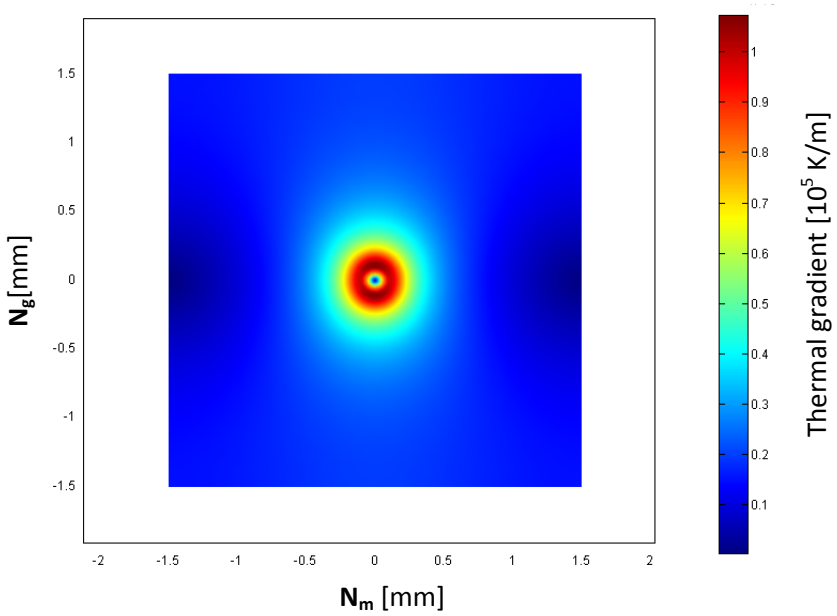

FIGURE 2.3: Calculated temperature gradients for a 3×3×3 mm^3 b-cut Yb:KGW crystal operating at 5.5 % quantum defect. An absorbed pump power of 18 W in a 100 µm 1/e^2-radius is assumed and the cooling direction is along the $\mathbf{N_g}$ axis.

In the worst-case scenario, thermal gradients will lead to fracture of the laser material. Long before this, however, heating of the laser material causes serious issues due to thermal lensing, which might even be astigmatic. Thermal lensing is the sum of three different phenomena caused by heating that all of them will change the optical path in the material. The first phenomenon is the thermo-optic effect, dn/dT, i.e. the change in refractive index with temperature. There is also the thermal expansion, which causes bulging of the end facets. Modeling of this thermal bulging is quite complex, because it depends to a large degree on the material geometry due to the restraining effect of the cooler areas. This effect is taken into account in Eq. 2.13 below as the parameter C_α[40] which ranges between 0 and 1. The third effect arises from the stress induced by the interior frustration of thermal expansion. This stress alters the refractive index of the material through the photoelastic effect. As the stress is generally different in different directions, this effect may cause birefringence in otherwise isotropic materials. The three phenomena taken together will cause a change in the optical path that is given by:[41]

$$\Delta OP = \int_0^l \left[\frac{dn}{dT}(T) + C_\alpha (n-1)(1+\nu)\alpha_T(T) + n^3 \alpha_T(T) C_{r,\varphi} \right] T(x,y,z)dz, \qquad (2.15)$$

Here, $C_{r,\varphi}$ is the photoelastic coefficient, n is the refractive index, ν is Poisson's ratio and α_T is the thermal expansion coefficient along the propagation direction. Note that Eq. 2.15 relates to isotropic materials. In anisotropic materials, the thermo-optic coefficient depends on the polarization and the thermal expansion depends on the propagation direction. As a consequence, tensor notation must generally be used. For example, since the change in the optical path length occurs along the same direction as the propagation, this means that the term $(1+\upsilon)\alpha_T(T)$ should be replaced by $\mathbf{x}\cdot(\alpha_T)_{ij}\cdot\mathbf{x}$, where $(\alpha_T)_{ij}$ is the thermal expansion tensor and $\mathbf{x}$ is the normalized propagation directional vector.

If the temperature distribution is symmetric around the propagation direction, the focal length at distance r from said axis can be calculated as follows:[42]

$$f(r) = \frac{r^2}{2\left[\Delta OP(0) - \Delta OP(r)\right]}. \tag{2.16}$$

The important effect of the thermal lens is to alter the cavity conditions. This might destabilize initially stable cavities or it might improve the mode overlap between undesired higher-order modes and the pump mode, thus bringing these modes below lasing threshold. While the destabilization might decrease laser output power, the latter might reduce the beam quality.[43]

Chapter 3
Crystalline host materials for Er-Yb lasers

3.1 The Er-Yb laser system

The energy level diagram for Er,Yb-codoped systems, as well as the most relevant processes, is depicted in Fig. 3.1. As has been discussed in Section 1.1, most of the pump is being absorbed by the Yb^{3+} ions, exciting them from the ground state, i.e. the $^2F_{7/2}$-level, into the $^2F_{5/2}$-level. There are three different wavelength possibilities for this excitation, one for each Stark level of the $^2F_{5/2}$-level. The exact location of these wavelengths vary with the host material, but they tend to be around 900 – 920 nm, around 930-950 nm and around 970 – 985 nm, respectively. Only if the longest wavelength is used will there be any significant absorption by the Er^{3+}-ions. Note also that broadening can smear out these peaks, as e.g. in phosphate glass or under high temperatures.

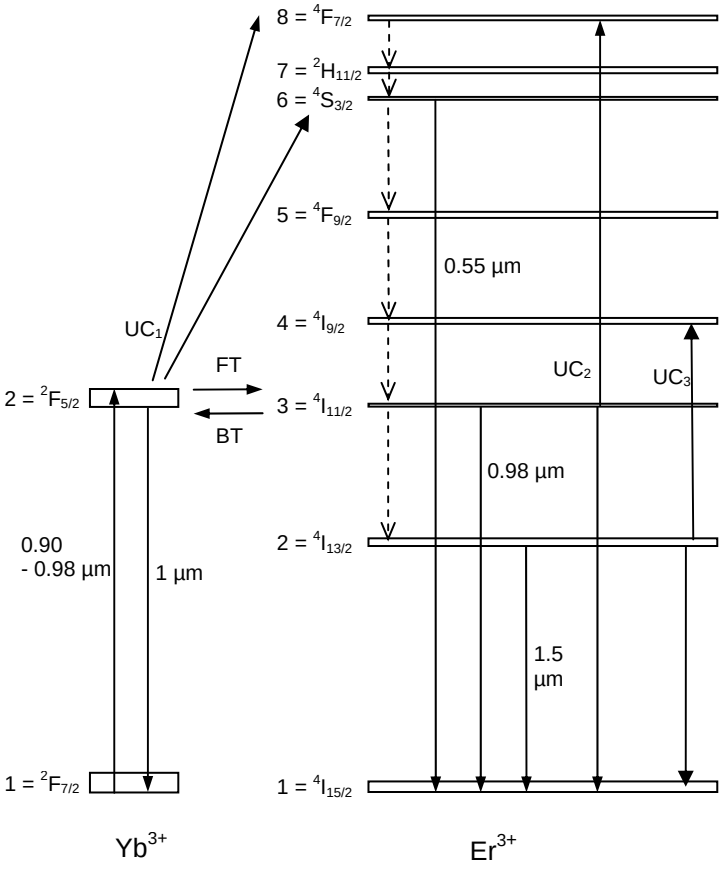

FIGURE 3.1: The energy level diagram of Er-Yb systems.

The absorbed energy is subsequently transferred to the $^4I_{11/2}$-level in Er, a process referred to as forward transfer (FT). This is a migration-assisted transfer process where the energy is typically transferred between several Yb^{3+} ions before being resonantly transferred to an Er^{3+}-ion. It follows

that the transfer rate is dependent on the Yb-Yb ionic distance. Once the energy has reached the Er^{3+}-ion, it is of utter importance that the ion rapidly decays into the $^4I_{13/2}$-level before the energy can be transferred back to an Yb^{3+} ion through the back transfer (BT) process. Another risk is that the energy is transferred to a material defect at some point in the migration. The effective macroscopic energy transfer rate from Yb^{3+} to Er^{3+} can be estimated experimentally as:

$$W_{\mathrm{Yb-Er}} = \frac{1}{\tau_{\mathrm{ye}}} - \frac{1}{\tau_{\mathrm{y}}}. \tag{3.1}$$

Here, τ_{ye} refers to the $^2F_{5/2}$-level radiative lifetime in the Er,Yb-codoped sample while τ_y refers to the same lifetime in a singly Yb-doped sample. In a host material where the relaxation from the $^4I_{11/2}$-level is so fast that back transfer can be neglected, $W_{Yb\text{-}Er}$ is approximately proportional to the Er doping concentration. Therefore, for a given Yb concentration, it is possible to establish an energy-transfer constant $k_{FT} = W_{Yb\text{-}Er}/N_{Er}$, where N_{Er} is the Er concentration. For the Yb concentration range of $10^{20} – 10^{21}$ cm^{-3}, k_{FT} in glass is dependent on the square of the Yb concentration.[44] As is illustrated in Fig. 3.2, which gives the transfer rate for glass and GdCOB at a constant Er concentration of $3.5 \cdot 10^{19}$ cm^{-3}, this statement appears to be true for oxoborate crystals as well.

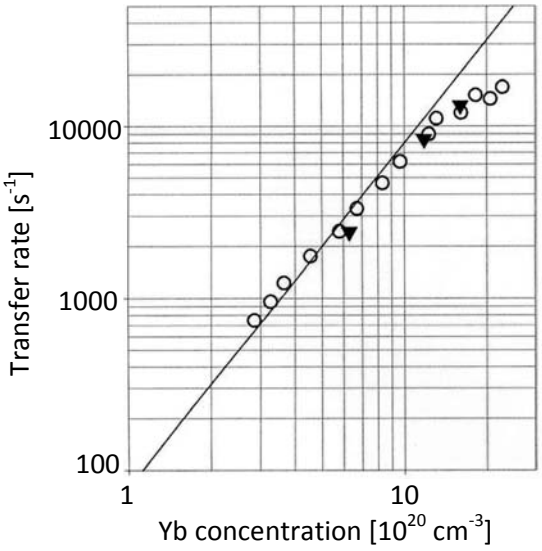

FIGURE 3.2: The transfer rate dependence on Yb concentration in glass[44] (circles) and GdCOB[I] (triangles) for $N_{Er} = 3.5 \cdot 10^{19}$ cm^{-3}.

It is evident that the Yb^{3+} concentration should generally be as high as possible without severe quenching or, in the case of glass, nanocluster crystallization. For hosts such as tungstates, YAG or vanadates,[45] on the other hand, where the lifetime of the $^4I_{11/2}$-level is non-negligible, the picture is quite different since the back-transfer rate has to be taken into account. This rate can be estimated as $W_{BT} = k_{BT} \cdot N_{Yb}$, where k_{BT} is the back-transfer coefficient and N_{Yb} is the ytterbium concentration.

In this model, k_{FT} and k_{BT} are material coefficients that are deduced from experiments. An alternative approach is the Dexter model, which in a first approximation that assumes dipolar-dipolar interaction to be dominant becomes:[46]

$$W_{FT} = \frac{3hc^2}{8\pi^4 n^2 R^6} \int \frac{\sigma_{\mathrm{e}} \sigma_{\mathrm{a}}}{E^2} dE. \tag{3.2}$$

In this model, R is the distance between neighboring excited Yb^{3+} ions and Er^{3+} ions in the ground-state, E is the photon energy and $\sigma_{e,a}$ are the cross-sections of ytterbium and erbium, respectively. Since the emission peak of Yb and the absorption peak of Er are overlapping around

0.98 μm, the integral is to be taken over the span of these peaks. The discrepancy between Eq. 3.2 and experimental results is quite significant, since it does not take quadrupole interactions into account.[46] Nevertheless, it gives a fairly good insight as to how different parameters influence the transfer efficiency.

There are three basic loss mechanisms in the Er-Yb energy level diagram. There is first the cumulative upconversion process, where an excited Yb ion interacts with an excited Er ion to achieve upconversion of that Er ion. This can proceed either through Yb ($^2F_{5/2}$) + Er ($^4I_{11/2}$) $\rightarrow$ Yb ($^2F_{7/2}$) + Er ($^4F_{7/2}$) or through Yb ($^2F_{5/2}$) + Er ($^4I_{13/2}$) $\rightarrow$ Yb ($^2F_{7/2}$) + Er ($^4F_{9/2}$). This process is illustrated in Fig. 3.1 as UC_1. A second process is the upconversion process between two excited Er ions. This can take the form of either Er ($^4I_{11/2}$) + Er ($^4I_{11/2}$) $\rightarrow$ Er ($^4I_{15/2}$) + Er ($^4F_{7/2}$), marked as UC_2 in Fig. 3.1, or Er ($^4I_{13/2}$) + Er ($^4I_{13/2}$) $\rightarrow$ Er ($^4I_{15/2}$) + Er ($^4I_{9/2}$), marked as UC_3. Finally, there is excited state absorption (ESA) of laser photons at both the $^4I_{11/2}$-level and the $^4I_{13/2}$-level. For all these cases, the excited electrons rapidly returns through multi-phonon relaxation processes, though some are channeled down to the ground state through spontaneous emission. This occurs at several wavelengths, but the emission at 0.55 μm from the $^4S_{3/2}$-level is visible and illuminates the pumped region in green. The ESA loss tends to be negligible at normal Er^{3+} concentrations around 1 % because the cross-section in e.g. glass is of the order of 10^{-22} cm^{-2}. [47] The upconversion processes, on the other hand, play a very significant role at high population inversions, e.g. in a Q-switched laser, and will limit the maximum inversion level. In phosphate glass, this limit is approximately 0.9 N_{Er}.[48]

Lasing occurs between the $^4I_{13/2}$-level and the $^4I_{15/2}$-level at a wavelength around 1.5 -1.6 μm depending on the host material. Since $\sigma_e \approx \sigma_a$ at the emission peak, this laser transition can be considered as being close to a true three-level system. As a result, around 50 % of the ions have to be excited in order to achieve population inversion, a fact that leads to high laser thresholds. To counter this, the lifetime of the $^4I_{13/2}$-level, $\tau_{Er,2}$, should be long. As has been discussed above, at the same time the lifetime of the $^4I_{11/2}$-level, $\tau_{Er,3}$, needs to be short due to the transfer process and also in order to limit upconversion losses. This constitutes the main problem in finding a suitable host material for Er-Yb systems.

For modeling the dynamics of the Er-Yb laser system, the following set of rate equations may be used.[49-51] The indices refer to the energy level indices in Fig. 3.1. It is assumed that the phonon relaxation is fast enough so that the energy levels 4, 5, 7 and 8 are depopulated instantaneously. Furthermore, the excited state absorption is assumed to be negligible. The equations are given by:

$$\frac{dN_{\mathrm{Yb},2}}{dt} = R_{\mathrm{P}} - \frac{N_{\mathrm{Yb},2}}{\tau_{\mathrm{Yb}}} - k_{\mathrm{FT}} N_{\mathrm{Er},1} N_{\mathrm{Yb},2} + k_{\mathrm{BT}} N_{\mathrm{Yb},1} N_{\mathrm{Er},3} - k_{\mathrm{C},3} N_{\mathrm{Er},3} N_{\mathrm{Yb},2} - k_{\mathrm{C},2} N_{\mathrm{Er},2} N_{\mathrm{Yb},2} \quad (3.3)$$

$$\frac{dN_{\mathrm{Er},6}}{dt} = -W_{\mathrm{NR},6} N_{\mathrm{Er},6} - \frac{N_{\mathrm{Er},6}}{\tau_{\mathrm{Er},6}} + k_{\mathrm{C},3} N_{\mathrm{Yb},2} N_{\mathrm{Er},3} + C_{\mathrm{up},3} N_{\mathrm{Er},3}^2 + k_{\mathrm{C},2} N_{\mathrm{Er},2} N_{\mathrm{Yb},2}, \quad (3.4)$$

$$\begin{aligned} \frac{dN_{\mathrm{Er},3}}{dt} &= -W_{\mathrm{NR},3} N_{\mathrm{Er},3} - \frac{N_{\mathrm{Er},3}}{\tau_{\mathrm{Er},3}} - k_{\mathrm{BT}} N_{\mathrm{Yb},1} N_{\mathrm{Er},3} + k_{\mathrm{FT}} N_{\mathrm{Er},1} N_{\mathrm{Yb},2} - k_{\mathrm{C},3} N_{\mathrm{Yb},2} N_{\mathrm{Er},3} \\ &- 2C_{\mathrm{up},3} N_{\mathrm{Er},3}^2 + W_{\mathrm{NR},6} N_{\mathrm{Er},6} + \beta_{63} \frac{N_{\mathrm{Er},6}}{\tau_{\mathrm{Er},6}} + C_{\mathrm{up},2} N_{\mathrm{Er},2}^2, \end{aligned} \quad (3.5)$$

$$\frac{dN_{\mathrm{Er},2}}{dt} = -\frac{N_{\mathrm{Er},2}}{\tau_{\mathrm{Er},2}} + W_{\mathrm{NR},3} N_{\mathrm{Er},3} + \beta_{32} \frac{N_{\mathrm{Er},3}}{\tau_{\mathrm{Er},3}} + \beta_{62} \frac{N_{\mathrm{Er},6}}{\tau_{\mathrm{Er},6}} - 2C_{\mathrm{up},2} N_{\mathrm{Er},2}^2 - R_{\mathrm{se}}, \quad (3.6)$$

$$N_{\mathrm{Yb}} = N_{\mathrm{Yb},1} + N_{\mathrm{Yb},2}\,, \tag{3.7}$$

$$N_{\mathrm{Er}} = N_{\mathrm{Er},1} + N_{\mathrm{Er},2} + N_{\mathrm{Er},3} + N_{\mathrm{Er},6}\,. \tag{3.8}$$

The population densities, $N_{\mathrm{Yb},1-2}$ and $N_{\mathrm{Er},1-6}$, correspond to the level numbers shown in Fig. 3.1. R_{P} is the pump rate from Yb (1) to Yb (2); τ_{Yb}, $\tau_{\mathrm{Er},2}$, $\tau_{\mathrm{Er},3}$ and $\tau_{\mathrm{Er},6}$ are the radiative lifetimes from the Yb (2), Er (2), Er (3) and Er (6) levels, respectively; $W_{\mathrm{NR},3}$ and $W_{\mathrm{NR},6}$ are the nonradiative decay rates from the Er (3) and Er (6) levels, respectively, $k_{\mathrm{C},i}$ is the cumulative upconversion coefficient with respect to the Er (2) and Er (3) levels, respectively, $C_{\mathrm{up},i}$ is the cooperative upconversion coefficient of the respective level, β_{ij} are the branching ratios from the Er (i) to the Er (j) levels and N_{Yb} and N_{Er} are the respective total Yb^{3+} and Er^{3+} ion concentrations in the material. R_{se} is the net rate of stimulated emission and reabsorption, which can be neglected when analyzing results from non-lasing fluorescence spectroscopy as in Section 3.4.

The traditional Er-Yb laser is a compact setup, often even monolithic, where the increased absorption from the Yb co-doping comes to full advantage. This is the laser type that will be treated in the following sections. The major alternatives are rod lasers and fiber lasers, which could be either singly Er-doped[52] or Er,Yb-codoped.[53,54] These lasers tend to give higher output powers, more than hundred Watts has been demonstrated and further scaling seems possible, but they operate at a completely different scale in terms of cost and size. Also, in the Q-switching regime, these lasers tend to give much longer pulse-durations due to the longer cavities.

3.2 Crystalline host materials

As stated before, phosphate glasses are by far the most common host materials for Er,Yb-codoped lasers. Even though the quantum defect limit for the slope efficiency in these lasers is around 60 %, the actual efficiency becomes significantly lower due to the transfer and the upconversion processes. A typical continuous-wave (cw) Er,Yb:glass laser, such as described in Ref. 44, exhibits a slope efficiency of 20 – 30 %, a threshold in the order of tens of milliwatts and a maximum output power of around 100 mW. The SELG laser glass,[55] which was recently developed for efficient high-average-power operation, can reach above 300 mW of output power (230 mW under single-frequency operation) with a slope efficiency of 27 % with regard to incident pump power. In a monolithic setup, where the mirrors are deposited directly onto the laser material, an average single-frequency output power of 138 mW has been achieved for 990 mW of incident pump power.[56]

Until a few years ago, lasing results in crystalline hosts were significantly worse. In Er,Yb:YAG, for example, only 30 mW of output power was achieved at a slope efficiency versus absorbed power of 7.0 %.[4] The threshold was around 50 mW. In the same paper, 20 mW of output power from an Er,Yb:YSO laser was reported at a slope efficiency of 5.6 % and at a similar threshold. 20 mW of output power has also been reported for an Er,Yb:CAS laser.[5] Here, the threshold was 20 mW and the slope efficiency was 5.5 % versus absorbed power. From Er,Yb:YVO_4, only 40 mW of output power could be achieved even though the incident power was 1.8 W.[7] Using LSB as a host material, however, a significant 150 mW of output power could be achieved.[57] Still, the slope efficiency was limited to 6 % versus incident power and the threshold was high, 800 mW of incident pump power. In this experiment, absorption was said to be around 70 %.

The first results that could seriously compare with glass lasers were obtained in YCOB and were published by Burns et al. in a series of papers in 2002-2003. These results are well summarized in Ref. 9. They achieved a slope efficiency versus absorbed power of 27 % in a hemispherical cavity, resulting in 250 mW of output power. As can be expected from a high-phonon-energy material such as YCOB, the threshold was also high: 850 mW of absorbed power. A flat-flat cavity yielded 150 mW of output power at 22 % slope efficiency and with a 1.05 W threshold. In both experiments a pump spot of 110 µm diameter and an output coupling of 1 % were used. These results remain the most

efficient outcome in terms of output power using crystalline hosts. However, in many industrial applications a compact monolithic laser design is preferred. Burns et al. investigated such a cavity, but the slope efficiency was limited to 3.4 %, apparently due to inferior coatings.

In 2004, we presented cw lasing results using a monolithic design and the much related crystal GdCOB,[I] which has a lower melting temperature that allows for platinum crucibles to be used in the growth process. In these experiments we obtained a 15 % slope efficiency and 70 mW output power, using Ti:sapphire pumping, while we obtained 7 % slope efficiency and 80 mW output power using diode pumping. In 2006 Tolstik et al. presented results with an Er,Yb:YVO_4 laser that produced an output power of 170 mW at a slope efficiency of 8 %.[45] The most recent results in the field appears to be from Er,Yb:YAB, in which 1 W continuous output power at 35 % slope efficiency has been obtained.[8] These experiments were reported only two weeks before the printing of this thesis and constitute the first demonstration of a crystal host material that is truly superior to glass.

Several applications of Er-Yb lasers, such as range-finding and LIDAR, require Q-switched operation. In the passively Q-switched regime, a monolithic setup where a saturable absorber is bonded to the active material has several advantages. Naturally, it makes the cavity mechanically more stable and compact. A further benefit of the compactness is shorter pulses and, consequently, higher repetition rates, as the pulse length scales with the cavity length.[58] In the case of Q-switching an Er-Yb laser with Co^{2+}:$MgAl_2O_4$ (Co:MALO or spinel),[59] a further benefit arises from the high thermal conductivity of spinel which makes the absorber act as an extra heat sink.[3]

In the case of glass host material, the highest passively Q-switched output power of 180 mW (150 mW under diode pumping) has been achieved using this setup in combination with the SELG-glass.[3] The slope efficiency versus incident power was around 15 % and threshold was about 200 mW of incident power. The pulse durations were 5 ± 1 ns.

In the case of crystalline hosts, the two first experiments were published simultaneously in June 2005.[60, II] Both of these setups used high-power diode bars/arrays operating in the quasi-cw regime as pump sources and both employed spinel absorbers. However, the cavity designs were quite different. In the experiments by Georgiou et al, the active material consisted of an Er,Yb:YAG crystal in a 180 mm long cavity. They achieved slope efficiencies of 2.2 % to 3.4 % with regard to incident power in the free-running regime. In the Q-switched regime, they only reported the pulse duration, 340 ns, and the pulse energy, 1.7 mJ. In our experiments, the active material consisted of an Er,Yb:GdCOB crystal in a 2.3 mm long monolithic cavity. Here, the slope efficiency was 11.6 % with regard to absorbed power and the average output power was 88 mW. Due to the much shorter cavity, pulse durations were only 5-6 ns. More recently, in 2007, 108 mW of Q-switched output power at a 9.6 % slope efficiency was obtained in an Er,Yb:YAB crystal[61] using a spinel absorber. In this case the pump was operating in the cw regime. The laser was designed in a non-monolithic cavity and the pulse duration was 135 ns.

As mentioned in the previous section, the experienced difficulties in finding a suitable host material for Er, Yb-doped lasers lies in the fact that the lifetime of the $^4I_{13/2}$-level, $\tau_{Er,2}$, should be long while the lifetime of the $^4I_{11/2}$-level, $\tau_{Er,3}$, needs to be short. A factor that contributes to this problem is the fact that the $^4I_{11/2}$-level lifetime is determined by phonon relaxation, which benefits from high phonon energies in the phonon spectrum of the host material. The $^4I_{13/2}$-level lifetime, on the other hand, is determined by spontaneous emission when the phonon spectrum only yields low energy phonons. However, the probability for multi-phonon relaxation is exponentially dependent on the inverse of the number of phonons needed to bridge the energy gap, as can be seen from the single-frequency model that gives the following expression for the multi-phonon quenching rate W_q:[62]

$$W_q = W_{q0}\left(\frac{\exp(E_{ph}/k_BT)}{\exp(E_{ph}/k_BT)-1}\right)^p . \tag{3.9}$$

Here, W_{q0} is the relaxation rate at zero-temperature and E_{ph} is the energy of the highest-frequency phonons in the lattice whose energies times p matches the band gap.

It follows that, when high-energy phonons are present in the host material, the lifetime of the $^4I_{15/2}$-level becomes increasingly limited by phonon relaxation.[63] As a consequence, the phonon spectrum becomes an issue in finding a suitable Er-Yb host material. Generally, these materials can be divided into two groups. The low phonon energy materials exhibit long lifetimes of both levels resulting in a low threshold but also in a low slope efficiency. The high phonon energy materials, however, exhibit short lifetimes of both levels resulting in a high threshold but also in a high slope efficiency. Finally there is phosphate glass, which exhibits lifetimes that are close to ideal. Table 3.1 gives a survey of a number of laser materials. It lists the highest energy phonons, which are the main source of multi-phonon relaxation.

Material	Highest phonon energy peak [cm^{-1}]	$\tau_{Er,2}$ [ms]	$\tau_{Er,3}$ [µs]	Reference
LSB	-	0.7	< 0.5	[64]
GdCOB / YCOB	1300	1.2	< 0.25	[65, I]
$LaBO_3$	1296	0.7	-	[66]
YAB	1500	0.35	< 5	[67, 8]
Phosphate glass	1180	8.5	2-3	[56,68]
CAS	1000	7.6	41	[49]
YSO	960	8	16	[4, 69]
KGW / KYW	900	3-4	148	[70, III]
YVO_4	888	2.5	27	[7, 71]
YAG	787	7.7	100	[70]

TABLE 3.1: A sample of Er-Yb laser host materials. In the case of GdCOB/YCOB and KGW/KYW, the values are closely related and only the Gd-values are listed.

Of course, another point to consider is the thermal conductivity. It is evident from the reported experiments that the most successful crystals so far have been different borates. While these borates have significantly higher thermal conductivity (2-5 W $m^{-1}K^{-1}$) than glass (< 1 W $m^{-1}K^{-1}$) , their thermal properties are often quite modest compared with the best crystals. Actually, a crystal with excellent thermal conductivity such as YAG (> 10 W $m^{-1}K^{-1}$) is roughly as much better compared to many borates as they in turn are compared to glass.

As the work presented in this chapter has mainly been performed with GdCOB and KReW (Re= Gd, Y, Lu, …) and the work in the rest of the thesis has been done exclusively with KReW, these two crystals will be presented in more detail in the following subsections.

3.2.1The GdCOB crystal

Gadolinium-calcium oxoborate is a biaxial crystal belonging to the monoclinic space group *Cm*. The unit cell parameters are *a* = 8.10 Å, *b* = 16.02 Å and *c* = 3.56 Å.[72] The non-orthogonal unit cell angle β is 101.26°. The Gd^{3+} ion is coordinated by six oxygen ions in the crystal lattice. The crystal structure is illustrated in Fig. 3.3. When doped with lanthanide ions, the ions predominantly occupy the Gd^{3+} sites in the lattice.

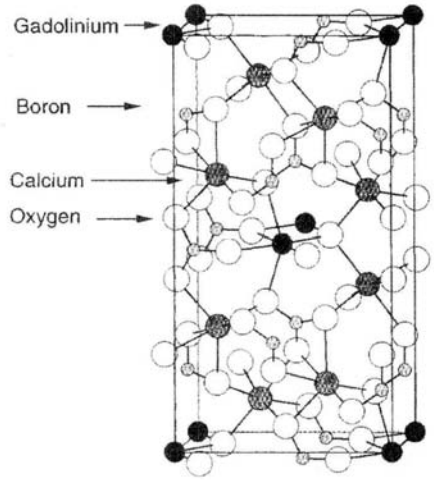

FIGURE 3.3: The crystal structure of GdCOB.[72]

Since GdCOB is a biaxial crystal, the indicatrix is an ellipsoid with three non-equal axes. The three axes of the ellipsoid form the dielectric directions **X**, **Y** and **Z**, respectively, with different optical properties. While the **Y**-direction is parallel to the crystallographic axis **b**, the other directions are given in Fig. 3.4.[72]

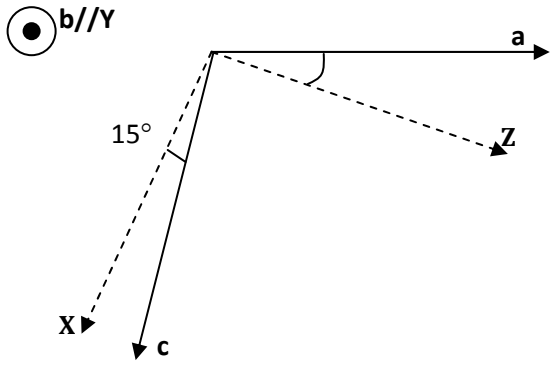

FIGURE 3.4: The orientation of the dielectric directions in GdCOB.

The transparency window of GdCOB is 320-2600 nm, which fits optical and near-infrared applications well. Since GdCOB has non-linear properties, d_{eff} = 2.1 pm/V in the optimal phase-matched direction,[74] it has been used as a frequency-conversion crystal for this region. The thermal properties, however, are often more significant for a solid-state laser host material. The most relevant thermal parameters of GdCOB are presented in Table 3.2. It can be seen from these parameters that the thermal conductivity is relatively low for this crystal. In fact, it is far from the conductivity in YAG of more than 10 $Wm^{-1}K^{-1}$ and it is only 2-3 times higher than in specially designed glasses.[3] Furthermore, the thermal expansion coefficients are in the order of 10^{-5} K^{-1}, which is about a factor of two stronger than in glass, and they are also anisotropic. Still, GdCOB exhibits some advantageous thermal properties such as a relatively low thermo-optic coefficient.

Property	*Value in GdCOB*
Thermal Conductivity	$\kappa \parallel$ **X** = 2.17 W $m^{-1}K^{-1}$, $\kappa \parallel$ **Y** = 1.32 W $m^{-1}K^{-1}$, $\kappa \parallel$ **Z** = 2.40 W $m^{-1}K^{-1}$
Thermal Expansion	$\alpha_T \parallel$ **a** = 1.1 · 10^{-5} K^{-1}, $\alpha_T \parallel$ **b** = 0.83 · 10^{-5} K^{-1}, $\alpha_T \parallel$ **c** = 1.5 · 10^{-5} K^{-1}
Thermo-optic Coefficient	dn/dT_{avg} = 2 · 10^{-6} K^{-1}
Density	ρ = 3.70 · 10^3 kg m^{-3}
Melting Point	T_m = 1480 °C
Specific Heat	C_p = 600 J $kg^{-1}K^{-1}$

TABLE 3.2: The most relevant thermal properties of GdCOB. All values except the melting point were obtained from Ref. 74 and are given for room temperature.

3.2.2 The KReW crystals

The KReW (Re = Yb, Y, Lu,…) crystals are members of the double tungstates family. Materials within this family are described by the formulation $A^{I}T^{III}(WO_4)_2$, where A is a monovalent alkali-metal cation (Li, Na, K, Rb or Cs) and T is a trivalent metal or rare-earth cation. KReW are biaxial crystals belonging to the monoclinic space group *C2/c*. The different KReW crystals have very similar properties, so in the following discussion only the values of the crystal KGW will be given as an example. The unit cell parameters in this crystal are a = 10.64 Å, b = 10.35 Å and c = 7.54 Å.[75] The non-orthogonal unit cell angle β is 130.8°. The crystal structure is maintained by chains of WO_4 groups in the **c** direction. The elements of the chains are linked by sharing vertex O4 and the chains are paired together two and two by sharing vertex O2, as illustrated in Fig. 3.5(a). The vertex O3 connects these chains to the Gd^{3+} chains going in the [1 0 1] direction. Two adjacent elements of the Gd^{3+} chains share these O3 edges. Parallel to the Gd^{3+} chains, chains of K^+ fill the vacancies. The parallel Gd^{3+} and K^+ chains are illustrated in Fig. 3.5(b). When doped with lanthanide ions, the ions occupy the Gd^{3+} sites in the lattice. Though these sites are equivalent in KGW, this is not the case in some of the other double tungstates such as NaGW which gives an wider, inhomogeneously broadened spectrum in these materials.

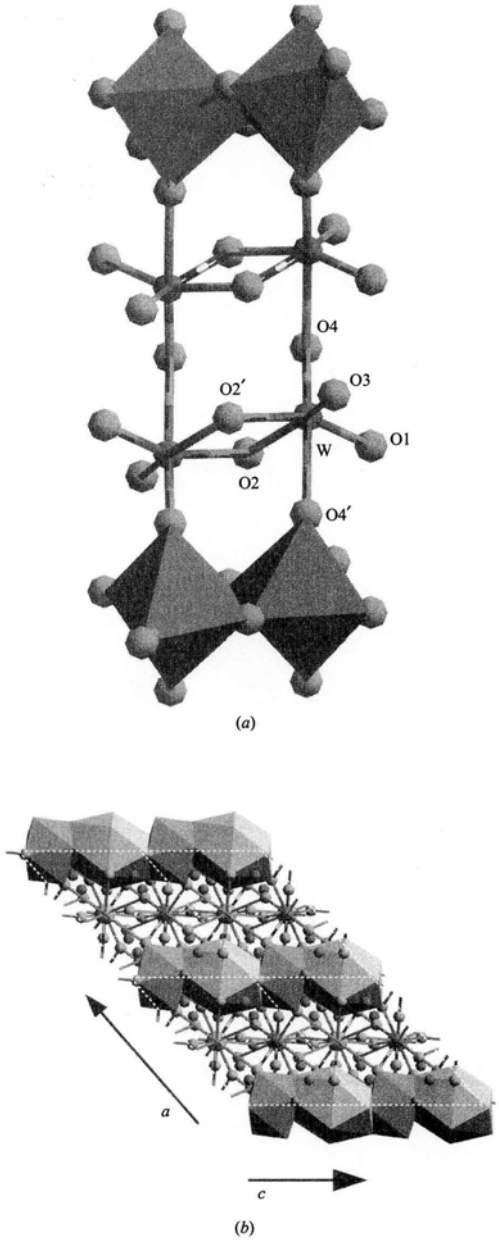

FIGURE 3.5: The crystal structure of KGW.[75] The parallel chains of WO_4 groups are illustrated in (a) while the Gd^{3+} and K^{+} chains are illustrated in (b).

Similar to GdCOB, KReW crystals are biaxial with three non-equal dielectric axes; $\mathbf{N_m}$, $\mathbf{N_p}$ and $\mathbf{N_g}$. While the $\mathbf{N_p}$-direction is parallel to the crystallographic axis **b**, the other directions are given, for KGW, in Fig. 3.6.[76]

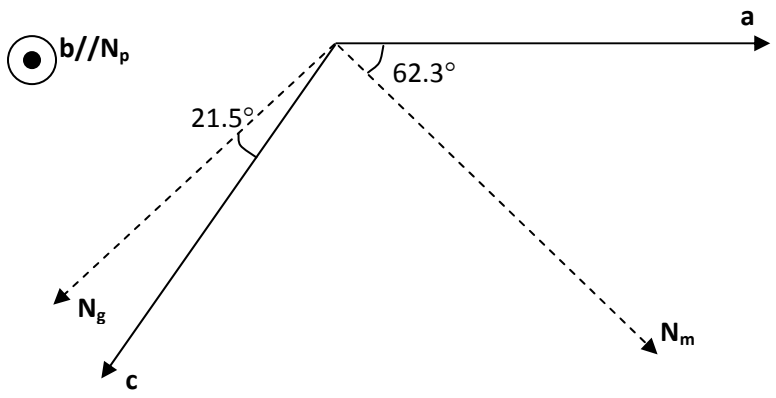

FIGURE 3.6: The orientation of the dielectric directions in KGW.

KReW crystals are optically very dense with refractive indices around 2. For Yb-doping, KGW is among the most promising host materials.[77] Yb:KGW lasers have shown good performance in all of the laser aspects where the Yb^{3+} ion offers advantages; high efficiency, high output power and broad emission bandwidth. Under single-pass end-pumping, an optical-to-optical efficiency of 47 % regarding incident power and an output power of 12.4 W can be simultaneously achieved.[IV] In a larger setup, with 24 pump passes through a thin disc crystal, the same optical efficiency can be achieved together with almost 60 W output power.[78] Moreover, the wide emission bandwidth has enabled pulses as short as 100 fs to be generated by using a semiconductor saturable absorber mirror (SESAM) for mode-locking.[79] When co-doped with Yb^{3+}, lasing of Er^{3+} at 1.5 µm in KGW has also been reported.[6] However, in this case the slope efficiency was only about 1 % with respect to the absorbed power which compares unfavorably with glass or with borates. As a final comment, it should be mentioned that the stimulated Raman scattering in KGW is strong enough to enable self-frequency Raman conversion in Yb:KGW.[80]

The thermal properties of KReW are highly anisotropic. For the athermal orientation approach to reduce thermal lensing, which is presented in Section 4.3, the anisotropy of the thermal expansion is especially important. The thermal expansion ellipsoid is defined by the three principal axes of thermal expansion, denoted $\mathbf{X'_1}$, $\mathbf{X'_2}$ and $\mathbf{X'_3}$, respectively.[76, 81] $\mathbf{X'_2}$ is parallel to the crystallographic **b**-axis while $\mathbf{X'_1}$ and $\mathbf{X'_3}$ are given, for KGW, by Fig. 3.7.

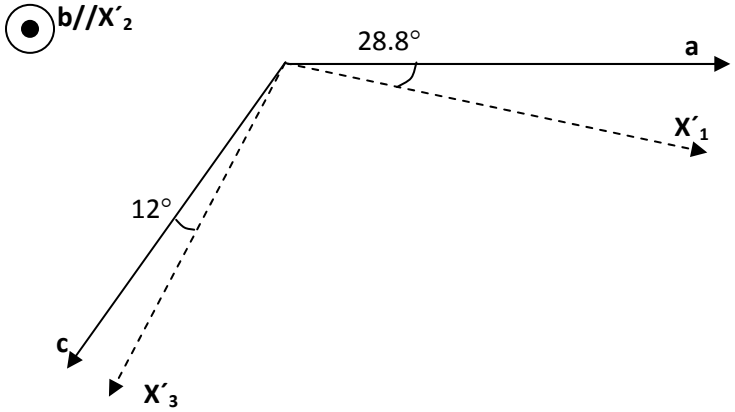

FIGURE 3.7: The principal thermal expansion directions in KGW.

The most relevant thermal parameters of KGW are presented in Table 3.3. It can be seen from these parameters that both the thermal expansion and the refractive index change are quite significant, but of opposite sign. This is crucial for the athermal orientation approach, where the two phenomena are made to approximately cancel. Furthermore, it can be seen that the thermal conductivity, though still less than in YAG, is quite reasonable and better than in GdCOB.

Property	*Value in KGW*	*Reference*
Thermal Conductivity	$\kappa \parallel \mathbf{N_p} = 2.5$ W m^{-1}K^{-1} , $\kappa \parallel \mathbf{N_m} = 3.0$ W m^{-1}K^{-1}, $\kappa \parallel \mathbf{N_g} = 3.5$ W m^{-1}K^{-1}	[81]
Thermal Expansion	$\alpha_T \parallel \mathbf{X'_1} = 1.1 \cdot 10^{-5}$ K^{-1}, $\alpha_T \parallel \mathbf{X'_2} = 0.28 \cdot 10^{-5}$ K^{-1}, $\alpha_T \parallel \mathbf{X'_3} = 2.3 \cdot 10^{-5}$ K^{-1}	[75]
Thermo-optic Coefficient	$dn/dT \parallel \mathbf{N_p} = -1.5 \cdot 10^{-5}$ K^{-1}, $dn/dT \parallel \mathbf{N_m} = -1.0 \cdot 10^{-5}$ K^{-1}, $dn/dT \parallel \mathbf{N_g} = -1.6 \cdot 10^{-5}$ K^{-1}	[81]
Density	$\rho \approx 6.50 \cdot 10^3$ kg m^{-3}	[82]
Melting Point	$T_m = 1031$ °C	[83]
Specific Heat	$C_p = 500$ J kg^{-1}K^{-1}	[84]

TABLE 3.3: The most relevant thermal properties of KGW. The density, however, is given for KYW.

3.3 Er,Yb:GdCOB laser experiments

For these experiments, the laser crystals were grown by the Czochralski method from a GdCOB melt with 38.5 at.% Yb (~$1.6 \cdot 10^{21}$ cm^{-3}) and 2.5 at.% Er (~$1 \cdot 10^{20}$ cm^{-3}) dopant concentrations. The melting temperature of GdCOB allowed the use of platinum crucibles as opposed to the iridium crucibles needed for YCOB growth. Following the growth, the crystals were cut perpendicular to the growth direction, which was the **Y** crystallographic axis. Two different crystal thicknesses were produced, 1.4 and 2.4 mm. Crystals were also grown from a melt with 28 at.% Yb (~$1.2 \cdot 10^{21}$ cm^{-3}) and 2.5 at.% Er dopant concentrations and these were similarly cut for 1.5 mm thickness to be used in the Q-switched lasing experiments. The input facet of the crystals was coated for high-reflectivity (HR) at the lasing wavelength around 1.54 µm while transmitting > 95 % at the different pump wavelengths between 0.9 µm and 1.0 µm. The opposite facet was coated for 97.9 % reflectivity at the laser wavelength for the cw experiments and left uncoated for the Q-switched experiments. The crystals were passively cooled through a copper or aluminum heat sink, using indium foil to fill out possible air gaps between heat sink and crystal.

Three different pump sources, referred to as A, B and C, respectively, were employed in the cw laser experiments.[I] Pump A was a quasi-continuous-wave (qcw) diode bar that consisted of seven emitters at 975 nm with a total bandwidth of 10 nm. The pump-pulse duration was 100 ms at a 20 % duty cycle. This pump source was used in combination with a 1.4 mm thick laser crystal. Pump B was a fiber-coupled single-emitter cw laser diode emitting at 975 nm with a spectral bandwidth of 6 nm. In these experiments, the laser crystal thickness was 2.4 mm. Pump C was a Ti:sapphire laser operating in the cw regime at a wavelength of 902 nm. In these experiments, a polarizer was positioned directly after the pump laser and the crystal thickness was once again 2.4 mm. For all cases, the pump spot diameter inside the crystal was ~100 µm ($1/e^2$). The output power performances of the different pump sources are illustrated in Fig. 3.8.

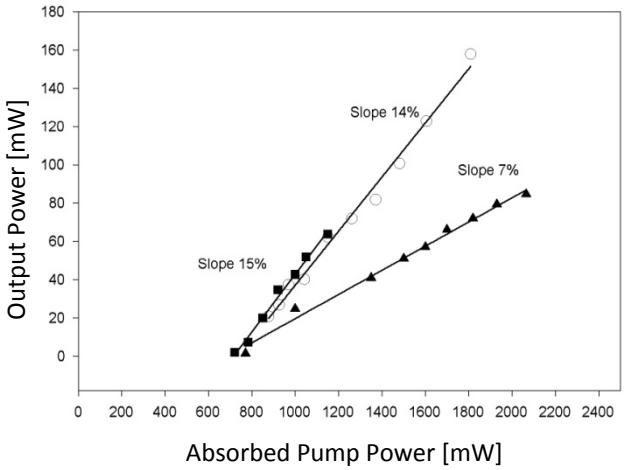

FIGURE 3.8: Input-output characteristics of the cw laser experiments. Empty circles refer to Pump A (QCW diode pumping, peak powers shown), solid triangles refer to Pump B (CW diode pumping) and solid squares refer to Pump C (Ti:sapphire pumping).

It is evident that all of the thresholds are quite similar, around 750 mW of absorbed pump power. The slope efficiencies using Pump A and Pump C are also similar around 14 – 15 %. Pump B, however, exhibits a drastically degraded slope efficiency. The reason for this might be that the monolithic cavity is very sensitive to thermal lensing. Using the other two pumps, the lens could be optimized either through adjusting the duty cycle or the polarization. Indeed, in the experiments, the output power at the same absorbed pump power varied noticeably with these parameters.

To Q-switch the Er,Yb:GdCOB laser, a 0.7 mm thick Co:$MgAl_2O_4$ (Co:MALO or spinel) plate with a single-pass saturable loss of 2 % was polished to optical finish and pressed into contact with the uncoated facet of one of the 1.5 mm thick crystals intended for Q-switching.[II] The reflection loss at this boundary should be negligible since the refractive index of Co:MALO ($n \approx 1.7$) roughly equals that of GdCOB. The opposite side of the Co:MALO plate was coated as an output coupler with 97.5 % reflection.

The pump laser in this case was different from the ones used in the cw experiments. It was a laser diode system from LIMO GmbH that was extensively used throughout this thesis work. The laser system was a diode-bar without fiber-coupling but with an integrated set of optics designed to focus the diode bar emission into a slightly elliptical spot with diameters of 97 × 95 µm (FWHM) or 125 × 175 µm ($1/e^2$). The intensity distribution of this spot was gaussian along the narrow direction and almost top-hat along the other direction. Two aspherical lenses in a confocal setup were used to image this focus into the crystal, resulting in a slightly enlarged spot of 150 × 200 µm ($1/e^2$ diameter). The designed emission wavelength at full power was 978 nm with a spectral width of 2.4 nm (FWHM), but it could be temperature tuned to coincide with the absorption center of Yb in GdCOB that is close to 975 nm. Likewise, it could be temperature tuned to 981 nm in order to match the absorption of Yb in KReW in later experiments. The pump absorption in the crystal was about 67 %. The diode laser was capable of cw operation, but in these Er,Yb:GdCOB experiments it was operated in the quasi-cw regime to obtain instant pump powers well above laser threshold while keeping the thermal load below the damage threshold. The pulse durations were 1 - 2 ms with different repetition rates. In the following discussion, the absorbed power during these pulses is referred to as absorbed peak power while the term absorbed average power refers to the absorbed energy per second from the repetitive pump pulses.

With this configuration, a train of Q-switched pulses was obtained. However, the train was irregular due to the different gain experienced by the different polarizations and the different lasing modes. Consequently, the laser pulse duration varied around 5 - 6 ns and the pulse energy varied around 2.8 ± 0.3 µJ with a resulting peak power of ~0.5 kW. Both pulse duration and energy

remained at this level for all pump powers. The laser wavelength was 1538 nm with a FWHM linewidth of 2 nm. The laser output performance at 1 ms pulse duration and 15 Hz pulse repetition rate can be seen in Fig. 3.9. Here, the average absorbed power was increased by increasing the absorbed peak power from zero to 5.7 W. The slope efficiency in these experiments was 11.6 % with a threshold of 1.65 W peak absorbed power corresponding to 25 mW of average absorbed power. The peak power threshold was about twice the cw threshold, in reasonable agreement with the addition of the saturable loss from the Co:MALO plate.

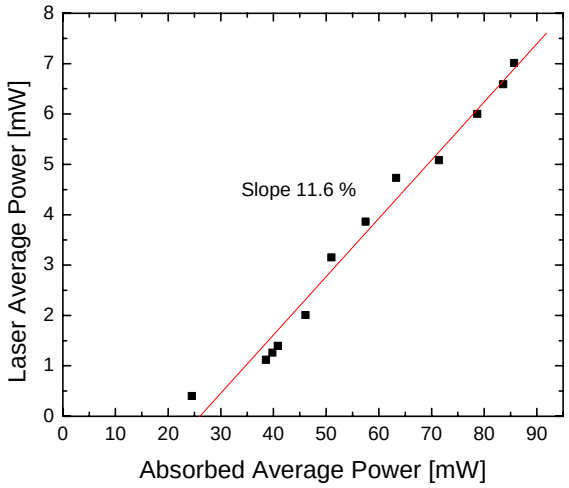

FIGURE 3.9: The input-output characteristics of the Q-switched laser when altering the pump power at constant pump pulse frequency.

If instead the peak absorbed power was fixed at 5.2 W and the pulse duration was similarly fixed at 2 ms while the repetition rate was increased, the output performance was slightly different as is illustrated in Fig. 3.10. This figure shows a linear dependence on input power for absorbed average powers lower than ~500 mW corresponding to average output powers of less than ~55 mW. After this point the thermal effects degraded the performance of the crystal until it finally fractured. The maximum output power, 88 mW, was achieved at 928 mW of absorbed average power.

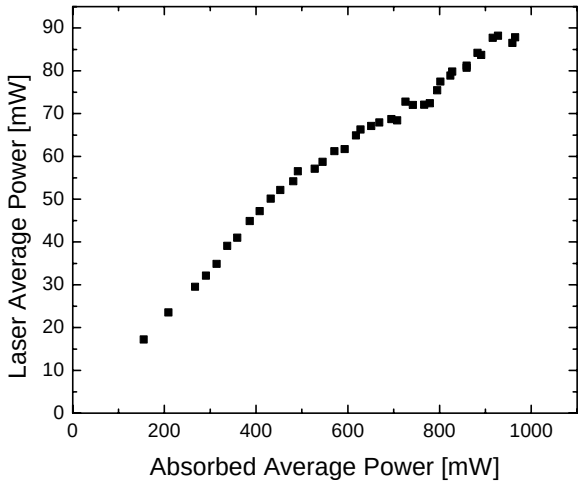

FIGURE 3.10: The input-output characteristics when altering the pump pulse frequency at constant pump peak power.

The maximum average output power was comparable to glass lasers, as was the amount of absorbed average power at fracture. Because the higher thermal conductivity should have given lower steady-state temperature gradients in the crystal, it seems that the fracture limit of GdCOB

might be lower than that of glass. One possible reason for this could be the significantly higher and anisotropic thermal expansion coefficient in the crystal.

3.4 Fluorescence dynamics in Er,Yb:KReW and Er,Yb:YAG

Initial experiments on oxoborates, such as those described in the previous section, are promising and many results are record-high for crystalline hosts. Nevertheless, it seems that the thermal capacity of these crystals is not good enough to finally beat glass as the preferential host material for Er-Yb lasers. Even if optimization would make the crystals slightly better than glass in terms of output performance, it does not seem realistic that the advantage would be strong enough to outweigh the vast knowledge base and easy manufacturing of glass materials. A benefit in some cases though, would be if the anisotropy could be utilized to yield polarized laser output.

In order to find a suitable crystal with better thermal capabilities, we performed spectroscopic investigations of several double tungstates[III] as well as YAG crystals at elevated temperatures.[IV] Of major interest in these investigations is the lifetime of the upper laser level, $\tau_{Er,2}$, as well as the transfer rate given by Eq. 3.1. The latter requires measurements of the ytterbium lifetime at different dopant levels as well as in singly Yb-doped samples. Another important issue is the lifetime of the $^4I_{11/2}$-level in erbium, $\tau_{Er,3}$. If this lifetime is short, it means that the upconversion processes involving this level, i.e. UC_2 and part of UC_1, are weak and it also indicates that the energy transfer is efficient since there is practically no back-transfer. Note that the effective transfer rate is still measured through the ytterbium lifetimes, although it is to a significant degree a result of $\tau_{Er,3}$. Finally, measuring the dynamics of the green upconversion from the $^4S_{3/2}$-level helps fitting parameters from Eqs. 3.3 - 3.8 to the experimental results while measurements of emission and absorption spectra are interesting for predicting the lasing wavelength, the pumping possibilities and the gain.

Compared to glass and borates, the Er,Yb-codoped double tungstates offer better thermal conductivity and significantly higher cross-sections, almost an order of magnitude in the case of absorption. This could even enable efficient Er-Yb thin-disc lasers as a solution to the thermal problems. However, as has been mentioned in Section 3.2, earlier experiments with Er,Yb:KGW are quite discouraging[6]. It seems possible though, that the poor efficiency was the result of non-optimal dopant concentrations. In KReW, $\tau_{Er,3}$ is much higher than in glass or borates and back transfer can no longer be ignored. As a result, the optimal dopant concentrations become quite different. Based on the following spectroscopic investigation, such concentrations have been estimated.

The first step in the investigation of the double tungstates was to find the lifetimes, $\tau_{Er,3}$ and $\tau_{Er,6}$, in the singly-erbium doped crystals. For this purpose, the erbium ions were excited by a Q-switched, frequency-doubled Nd:YAG laser with 3 ns pulse duration and 20 Hz repetition rate, focused into a 200 µm diameter spot. This spot was positioned close to one of the crystal side facets and collected perpendicularly by an imaging system with a sharp depth-of-focus in order to reduce the effects of radiation trapping. It is possible to further reduce such effects by using a limiting aperture, since the measured lifetimes depend on the acceptance angle of the detecting system.[85] This is often done by repeatedly decreasing the aperture of a pinhole and then extrapolate the lifetimes to zero aperture. In our setup, however, we did not use a pinhole but by reducing the detector area from 13 mm^2 to 0.8 mm^2 we noticed a reduction in the measured lifetimes of 6 - 21 %. After collection, the fluorescence passed several band-pass filters to select the wavelength of interest, before being detected by a silicon photodiode. In this way, the dynamics of the fluorescence at 0.55 µm (for $\tau_{Er,6}$) and 1 µm (for $\tau_{Er,3}$) in KGW and KYW crystals of different doping concentrations were measured. Table 3.4 summarizes these results, together with the values for $\tau_{Er,3}$ in phosphate glass[3] and GdCOB[I]. The results agree well with the measurements by Pujol et al. (Er:KGW)[76] and Kuleshov et al. (Er:KYW).[86] The results further confirm that $\tau_{Er,3}$ in KReW is much longer than in glass or in GdCOB.

Host crystal	Er conc. (mol %)	$^4S_{3/2}$ lifetime (μs)	$^4I_{11/2}$ lifetime (μs)
KGW	1%	26	148
	3%	23	153
	5%	19	151
KYW	5%	14	123
Glass	0.9%		2.5[3]
GdCOB	2.5%		0.25[I]

TABLE 3.4: Lifetimes of the $^4S_{3/2}$ and $^4I_{11/2}$ levels in singly Er-doped crystals.

Next, we employed a nanosecond optical parametric oscillator (OPO) to selectively excite the ytterbium ions in codoped samples. The OPO was tuned to 935 nm, where there is significant ytterbium absorption but negligible erbium absorption, and focused in a similar way to that of the YAG laser of the previous paragraph. The fluorescence gathering and detection system was also the same as before, except that an InGaAs photodiode was used for the ~1.5 μm emission. With this setup, the dynamics of the Yb ($^2F_{5/2}$), Er ($^4I_{13/2}$) and Er ($^4S_{3/2}$) levels could be measured. For the Er($^4I_{11/2}$) level, codoping should not affect the lifetime so the measurements shown in Table 3.4 for the singly-doped sample should suffice. The temporal resolution of the detection system was at least 100 ns, except for low-power upconversion fluorescence signals, where a 12 μs resolution was sometimes necessary to increase the sensitivity. This resolution was determined by the adjustable RC time constant of the detection system. Since the density of the excited Yb^{3+} ions never rose above 5% of the total Yb^{3+} concentration in our experiments, absorption saturation and stimulated emission can safely be neglected. The measured risetimes and lifetimes, as well as some measured and literature values for glass and GdCOB for reference, are shown in Table 3.5 below.

Host crystal	Er conc. (mol %)	Yb conc. (mol %)	Yb ($^2F_{5/2}$) lifetime (μs)	Er ($^4S_{3/2}$) risetime (μs)	Er ($^4S_{3/2}$) lifetime (μs)	Er ($^4I_{13/2}$) risetime (μs)	Er ($^4I_{13/2}$) lifetime (ms)
KGW	–	5%	438	–	–	–	–
	0.5%	5%	273		126	252	3.3
	0.5%	2.5%	229		101	24	3.3
	2.5%	7.5%	222		95	222	3.8
	1.4%	2.5%	212		92	207	3.2
	5%	5%	170	4	71	173	3.6
KYW	–	5%	440	–	–	–	–
	0.5%	5%	341	8.5	111		
	0.5%	2.5%	262	7.5	95		
	1.5%	2.5%	177	6	79	170	3.4
KYbW	1%		(~ 490)		(~ 115)		3.2
	3%		(~ 410)		(~ 105)		3.8
Glass	–	15.5%	1200[3]	–	–	–	–
	2.75%	22%	12	–	–		8.5[3]
GdCOB	–	10%	2300	–	–	–	–
	2.5%	28%	34	–	–	35	1.16

TABLE 3.5: Lifetimes and risetimes of the Yb ($^2F_{5/2}$), Er ($^4S_{3/2}$) and Er ($^4I_{13/2}$) levels in Er,Yb-codoped crystals.

The fluorescence dynamics of the Yb ($^2F_{5/2}$) level in Yb:KGW and some different Er,Yb:KGW crystals are shown in semilogarithmic scale in Fig. 3.11. For the KYW crystals of various dopings, the dynamics look very similar. It appears that the lifetime, $\tau_{Yb,2}$, decreases from 438 μs to 170 μs with increasing erbium concentration. This indicates significant energy transfer and the deduced transfer rate using Eq. 3.1, $W_{Yb\text{-}Er}$ = 3600 s^{-1}, is only a factor 2 - 3 below that of glass and GdCOB. For the case of stoichometric crystals, KYbW, the decay was non-exponential due to the high Yb^{3+}-excitation and thus strong upconversion in these samples. For these crystals, the lifetimes given in Table 3.5 are

from a single-exponential fit to the tail after 0.5 ms. Naturally, there is a much larger uncertainty in these experiments, but it seems that the lifetimes are approximately the same as those of the singly-doped Yb samples. This is not surprising given the low Er-to-Yb ratio in these crystals.

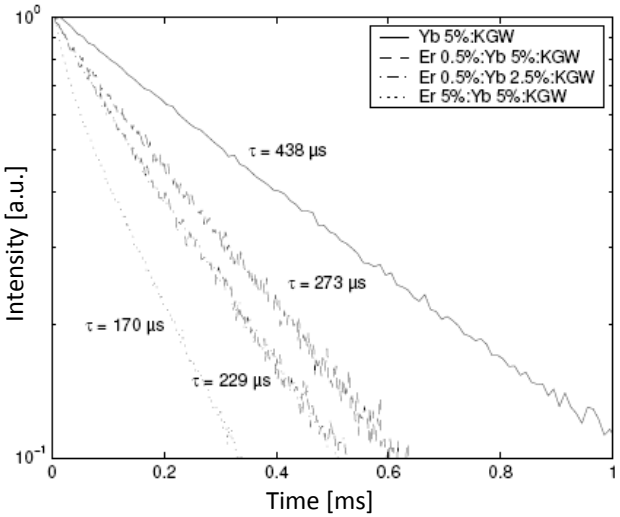

FIGURE 3.11: Fluorescence dynamics from the Yb ($^2F_{5/2}$) level around 1 µm in Yb:KGW and Er,Yb:KGW.

The visible green upconversion is much stronger in Er,Yb:KGW than in Er,Yb:GdCOB or Er,Yb:glass. The reason for this is a strong dipole-dipole interaction and a long lifetime of the Er($^4I_{11/2}$) level. This becomes evident through lifetime measurements. Because the energy redistribution between excited Yb^{3+} and Er^{3+} ions is fast and efficient due to the strong interaction, the dynamics of Yb($^2F_{5/2}$) and Er($^4I_{11/2}$) become coupled and thereby approximately equal. Furthermore, the lifetime of the Er($^4S_{3/2}$) level is very short, so the relaxation dynamics of this level follow closely the level from which the upconversion originates. Since the process scales as the square of the originating level population, the green lifetime should be half the lifetime of this level. Thus, the fact that the green lifetime is ~20 µs in singly-doped Er:KGW, as seen in table 3.4, and 126 µs in 0.5 % Er, 5 % Yb:KGW clearly indicates significant cumulative upconversion. Examples of green emission curves are given in Fig. 3.12.

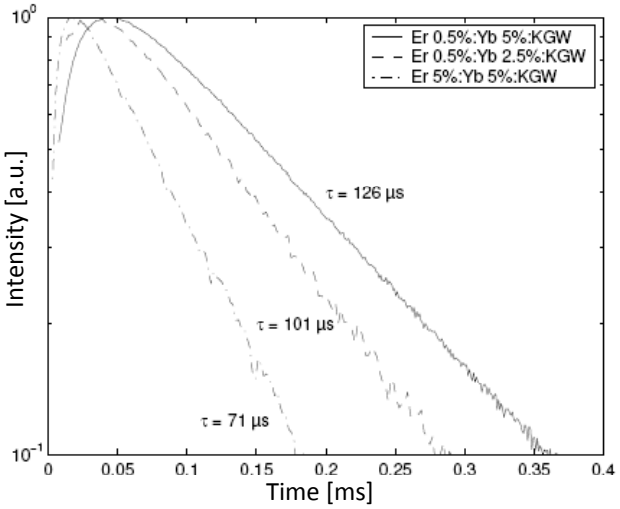

FIGURE 3.12: Dynamics of the green emission from the Er ($^4S_{3/2}$) level at 0.55 µm in Er,Yb:KGW.

In order to analyze the spectroscopic results and to find the optimal dopant concentrations, it is important to account for the UC and the ESA processes. The probability of these processes

correlates strongly with the match between the involved energy transitions. For example, the energy released in de-excitation from Yb ($^2F_{5/2}$) to Yb ($^2F_{7/2}$) is between 9619 cm^{-1} and 10728 cm^{-1} depending on the involved Stark levels. This matches well the excitation energy from Er ($^4I_{11/2}$) to Er ($^4F_{7/2}$), which ranges from 10140 cm^{-1} to 10385 cm^{-1}, making this cumulative upconversion process likely. On the other hand, the excitation energy from Er ($^4I_{13/2}$) to Er ($^4F_{9/2}$) ranges between 8461 cm^{-1} and 8852 cm^{-1} resulting in a low probability for a cumulative upconversion process involving the upper laser level. Using a similar energy reasoning regarding the upconversion processes involving two Er ions, it is possible to conclude that such upconversion from the Er ($^4I_{13/2}$) level should also be relatively weak. An experimental indication of this is that the Er ($^4I_{13/2}$) lifetime does not decrease with Er concentration, despite the non-linear behavior of the upconversion. Finally, the ESA process would require photons with a wavelength of 1655 - 1777 nm to match the excitation energy. Thus it seems that ESA of the lasing photons around 1.55 µm is unlikely.

In conclusion, the relevant lifetimes for 1.5 µm lasing in Er,Yb:KGW and Er,Yb:KYW have been measured. In addition, the physical background suggests that ESA should be negligible and that only UC involving the Er ($^4I_{11/2}$) level needs to be considered. This forms a good fundament for mathematical modeling following e.g. Eqs. 3.3 - 3.8.

Er,Yb:YAG is similar to Er,Yb:KReW in the sense that the phonon cut-off is low enough for $\tau_{Er,2}$ to be determined by spontaneous emission while $\tau_{Er,3}$ is determined by a relatively slow multi-phonon relaxation process. As a consequence, when the temperature is increased to 600 – 800 °C, $\tau_{Er,2}$ should remain approximately constant while $\tau_{Er,3}$ should drop significantly. This way the energy transfer efficiency should increase so as to match glass or borates, while the upper laser level lifetime should remain at acceptable levels. Furthermore, Er,Yb:YAG is an outstanding crystal in terms of thermal conductivity. This remains true even at 800 °C, where the thermal conductivity of YAG is ~5 $W\ K^{-1}m^{-1}$.[87] For the purpose of investigating the change in the fluorescence dynamics at elevated temperatures, we grew several Er,Yb:YAG crystals of different doping concentrations using the vertical zone melting technique.

For the high-temperature spectroscopy, the crystals were placed in resistant-heated ceramic tube ovens with open ends and with a thermocouple for measuring the temperatures. For measurement of the lifetimes $\tau_{Er,2}$ and $\tau_{Yb,2}$, a pulsed diode laser at 975 nm was used. When measuring the lifetime $\tau_{Er,3}$, however, the signal dropped rapidly at higher temperatures and a Q-switched ruby laser had to be employed to excite the erbium ions through the Er($^4F_{9/2}$) level. To avoid radiation trapping, all measurements were held in small samples (< 0.3 mm) immersed in glycerin.

The measured lifetimes in singly-doped Er:YAG and Yb:YAG samples at different temperatures can be seen in Fig. 3.13 below. Clearly, neither $\tau_{Er,3}$ nor $\tau_{Yb,2}$ are significantly influenced by temperature. In contrast to this, $\tau_{Er,3}$ decreased rapidly with temperature and at 600 – 800 °C all lifetimes were comparable to the corresponding room temperature parameters in the common phosphate based laser glasses. Also shown in Fig. 3.13 is the theoretical prediction based on Eq. 3.9 with an assumed bandgap of 3750 cm^{-1} [88] bridged by five phonons around 750 cm^{-1} and an assumed lifetime at room temperature of 100 µs. While the measurements and the theory agree well at lower temperatures, there is a significant discrepancy at 600 – 800 °C. This discrepancy is probably caused by the increased impact of additional relaxation processes involving lower-energy phonons not included in the single-frequency model.

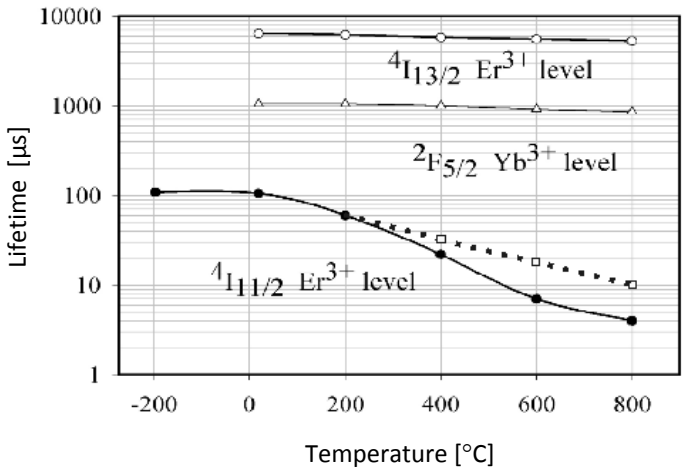

FIGURE 3.13: Temperature dependence of the most interesting lifetimes in singly-doped Er:YAG and Yb:YAG samples at temperatures from -200 °C to +800 °C. The squares correspond to the theoretical values using Eq. 3.8.

Next, the absorption spectrum of Yb:YAG and both the emission and the absorption spectra of Er:YAG were measured at different temperatures. For the absorption measurements we used an incandescent lamp as excitation source, while the emission spectra were recorded using a 975 nm laser diode for excitation. In general, the spectra were broadened and the amplitudes were reduced at higher temperatures, as can be seen for Yb:YAG in Fig. 3.14 given as an example. This also resembles the typical situation in glass compared to that in crystals and the absolute values of the cross-sections in YAG at 800 °C are very close to those in glass.

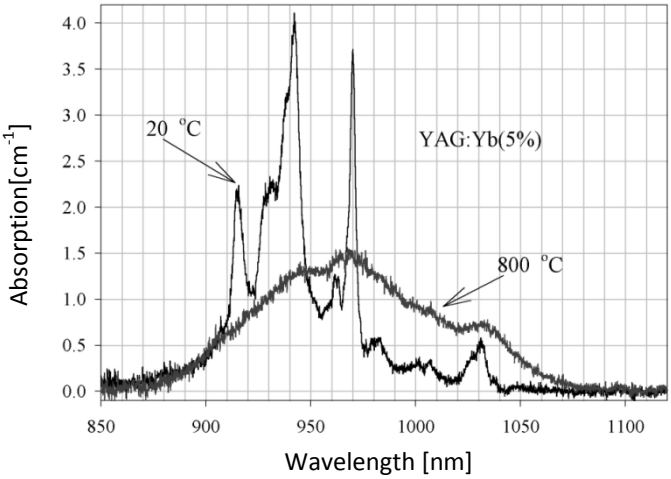

FIGURE 3.14: Absorption spectra of Yb:YAG at both 20 °C and 800 °C. Yb concentration is $1.38 \cdot 10^{20}$ cm^{-3}.

Once the cross-sections are known, the gain curves can now be calculated for different population inversions. Some representative curves for both room temperature and elevated temperature are presented in Fig. 3.15. Due to the increased thermal population of the higher order Stark levels at 800 °C, the population inversion necessary to reach threshold in a cavity with, say, 2 % loss is increased from ~0.4 to ~0.6. Furthermore, while lasing in a low-loss cavity can be expected to start in one of the two peaks above 1600 nm at room temperature, the laser wavelength will always be below 1600 nm at 800 °C. The FWHM-bandwidth of the gain is also increased. This increased bandwidth and the wavelength shift are more similarities to glass lasers.

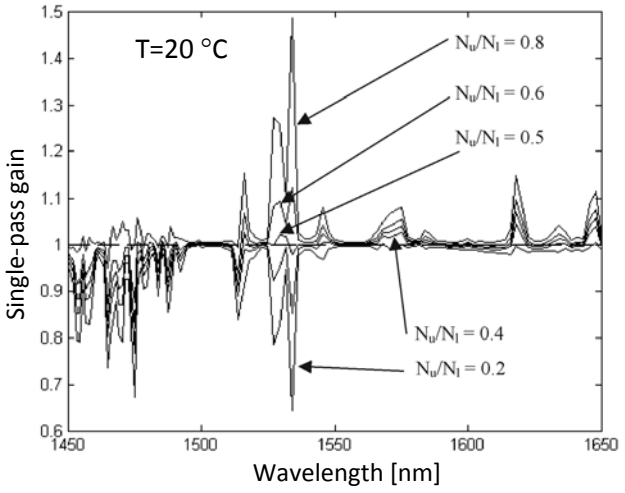

(a)

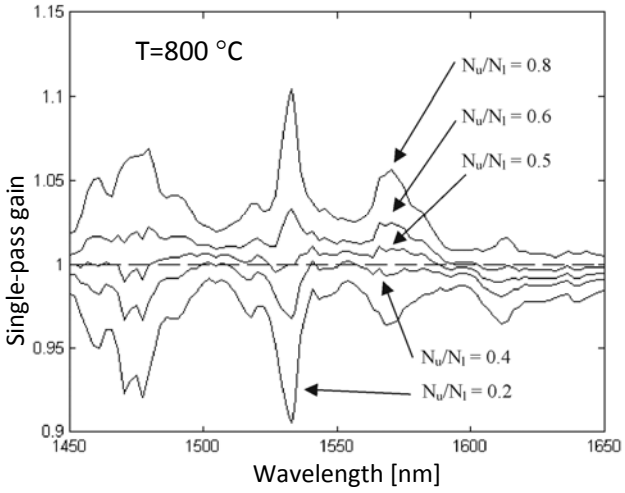

(b)

FIGURE 3.15: Calculated single-pass gain curves for Er^{3+} in YAG at different population inversions (N_u/N_l) for both (a) 20 °C and (b) 800 °C. The Er concentration is 10^{20} cm^{-3} and the crystal thickness is 3 mm.

Finally, we turned our attention to the co-doped samples in order to find the energy transfer efficiency. The macroscopic transfer rate, $W_{Yb\text{-}Er}$, was found through measurements of the Yb($^2F_{5/2}$) level lifetime by use of Eq. 3.1. The dopant concentrations are of course an issue of optimization and Fig. 3.16 shows the measured transfer rates at three different temperatures and four Yb concentrations for the samples with $1 \cdot 10^{20}$ cm^{-3} Er concentration. Considering the short lifetime of the Er($^4I_{11/2}$) level, it is a bit surprising that the transfer rate does not reach above 4500 s^{-1}. The explanation for this can be found from Eq. 3.1, where it is seen that the microscopic transfer rates are proportional to the integrated cross-sections. It appears thus that not only the peak values of the cross-sections decrease but also the area under the cross-sections, despite the broadening.

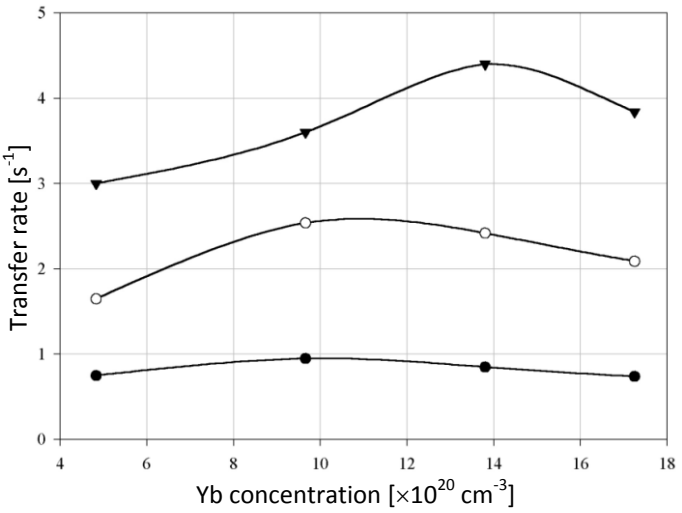

FIGURE 3.16: The $W_{Yb\text{-}Er}$ dependencies on Yb concentration at various temperatures for $1 \cdot 10^{20}$ cm^{-3} Er concentration. Solid triangles refer to 800 °C, empty circles to 600 °C and solid circles to 20 °C.

Following these results, it appears that the lifetimes and spectra of Er, Yb:YAG at elevated temperatures closely resemble those in Er,Yb:glass, while the thermal conductivity is at least five times higher. Still, though the lifetimes look promising and the energy transfer rate is indeed increased five times as compared to room temperature, the energy transfer is not quite as high as in the case of glass. As for the issue of a high-temperature laser, some initial experiments were actually made. Most probably, however, the practical problems with high-temperature lasers of this kind in terms of e.g. coatings, as well as the increased upconversion from the high inversion levels make such a laser very challenging.

Chapter 4
End-pumped Yb:KReW lasers

4.1 The Yb laser system

The energy level system of the 1 µm laser transition in Yb^{3+} is extraordinarily simple. The only relevant energy levels are the $^2F_{7/2}$ and $^2F_{5/2}$ levels with their respective Stark sublevels. Similar to the Er-Yb system, the pumping process takes place between the lowest energy Stark sublevel of the $^2F_{7/2}$ level and one of the Stark sublevels of the $^2F_{5/2}$ level. The lasing typically occurs between the lowest sublevel of the $^2F_{5/2}$ level and one of the upper Stark sublevels of the $^2F_{7/2}$ level. These three possible energy transitions in combination with vibronic broadening,[11] give rise to a broad emission spectrum. This is illustrated for Yb:KYW in Fig. 4.1.

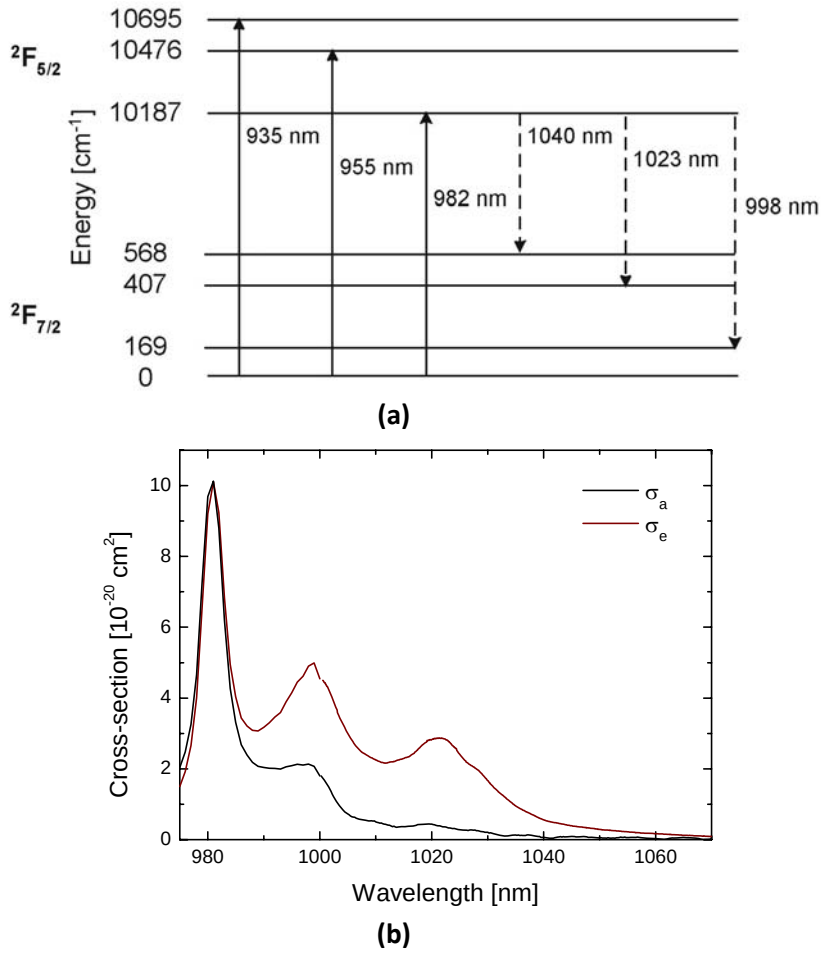

FIGURE 4.1: (a) The different energy levels in Yb:KYW with respective energies in cm^{-1} [10] as well as the wavelengths of the essential transitions. (b) The measured cross-sections for $\mathbf{N_m}$ polarization.

Within this spectrum, the exact laser wavelength is set by the cavity loss. In a low-loss cavity, the laser threshold is reached already at low population inversions. Under such conditions the gain is highest at long wavelengths with weak reabsorption, typically around 1040 - 1050 nm in Yb:KReW (Re = Gd, Y, Lu, …). In cavities with higher losses, the wavelength will be closer to the peak, around 1020 - 1025 nm in Yb:KReW. For much the same reason, there is also a drift towards longer wavelengths with increasing pump power. At higher pump powers, the temperature of the pumped region rises and thereby also the thermal population of the lower laser level which affects the reabsorption. The amplitude of this drift can be up to a few nanometers.[V]

Because both pumping and lasing occurs between the same $^{2S+1}L_J$ levels, the only energy loss in the process is due to phonon relaxation between the two Stark levels in the $^2F_{7/2}$ manifold. This property and the practical absence of UC and ESA make Yb systems extremely efficient. For the same reasons, the heat generation is low. This low heat generation in combination with a laser medium geometry that maximizes the surface-to-volume ratio, such as a thin-disc[14] or fiber[17] setup, has made kW-level lasers possible. Another approach, which has met a lot of interest during the last few years, is to cryogenically cool the Yb-doped laser medium.[89] Cryogenic temperatures improve the thermo-optic properties significantly. In YAG, for example, the heat conductivity is increased almost four-fold.

While these laser designs are often necessary to obtain output powers above ~10 W, they have several drawbacks. The cryogenic approach requires cryogenic cooling, fiber lasers are ill-suited for high peak-powers and many host materials are challenging to form into thin-discs or fibers. Furthermore, with a room temperature end-pumped laser utilizing a small crystal as active medium the laser head can be made much more compact. This design is therefore often preferable when extreme powers are not needed and it is also suitable for testing new laser concepts. This design has been used throughout the thesis and the following two paragraphs will discuss different output powers and efficiencies obtained with this configuration.

Using Ti:sapphire end-pumping, slope efficiencies with respect to absorbed power of 86.8 % have been reported using Yb:KGW.[10] Under diode end-pumping, the most efficient configuration has used Yb:KLuW pumped by a fiber-coupled diode focused to a spot of ~40 µm.[11] Here, the slope efficiencies with respect to the incident pump power reached 78 % and the optical efficiency was around 50 %. Chénais et al.[90] presented a series of experiments using different host materials and the slope efficiencies versus absorbed power were ~58 % in GdCOB, ~57 % in YCOB, ~54 % in YAG, ~25 % in KGW, ~66 % in GGG and ~40 % in YSO. The low slope efficiency of KReW in the experiments by Chénais et al. are somewhat surprising and, in contrast, Lagatsky et al. presented a higher slope efficiency of 53 % versus absorbed power,[91] as did Liu et al.[11] Recently, a slope efficiency of 78 % versus absorbed power was reported in $GdVO_4$.[92]

In the above demonstrations relatively low-power and high-brightness pump sources have been used and the maximum generated power did not exceed 3.5 W. Higher output powers were generated by Kong et al.[93] who achieved 9.2 W of output power at 27 W of absorbed pump power with a slope efficiency of 41 %. In these experiments, a ceramic Yb:Y_2O_3 crystal was pumped by a fiber-coupled laser bar. In the same experiment, an Yb:YAG crystal gave a maximum output power of slightly more than 3 W at 15 W absorbed power. Here, the performance of the YAG crystal was severely limited by thermal lensing and higher pump powers rendered even the shortest possible cavity unstable. Other experiments using the same ceramic host material yielded 5.5 W output power at 31.1 W absorbed pump power with a 25 % slope efficiency.[94] With Yb:$LuYSiO_5$ (Yb:LYSO) a maximum output power of 7.8 W at 51 % optical efficiency in terms of absorbed power was obtained.[95] Very recently, a total of 11.5 W at 40 % optical efficiency regarding incident power was reported from an Yb:KLuW crystal.[96] Finally, using Yb:KGW we achieved 12.4 W of output power at 47 % optical efficiency in terms of incident power.[V] This experiment is described in further detail in Section 4.2.

However, since the achieved output powers and efficiencies depend on the available pump sources and other experimental details, they do not necessarily reflect the merit of the different crystals for any arbitrary application. Furthermore, several crystal compounds have mostly been

tested in thin-disc configurations while others have been tested primarily under end-pumping conditions. To present some properties which are more inherently linked to the crystals themselves, Table 4.1 gives an overview of a number of common Yb host crystals.

Host	λ_{pump} [nm]	λ_{laser} [nm]	τ [µs]	σ_e [$\times 10^{-20}$ cm^2]	σ_a [$\times 10^{-20}$ cm^2]	κ [Wm^{-1}K^{-1}]
YAG	941, 968	1021[97]-1052[97]	1040[85]	1.9[85]	0.7[98]	11[85]
LuAG	940, 970	1078[99]	1100[99]	2.7[100]	1[99]	10[100]
YVO_4	985	1014[101]-1037[102]	318[102]	0.5-1[102]	6.7[102]	7.9-11[102]
KGW/ KYW	981	995[103,104] -1063[VII]	232[85]	3[33]	18.8[33]	2.5-3.5[81]
GSO	974	1012[105]-1112[105]	-	0.4[105]	0.3[105]	-
YSO	977	1003[106]-1091[107]	670[107]	0.5[107]	2.3[107]	4.4[107]
LSB	981	1000[108]-1085[108]	730[85]	0.3[108]	1.2[108]	2.8[85]
YAB	977	520[109] -522[110] 1034[111]-1050[112]	450[112]	0.5[110]	4.1[112]	4.7[111]
Y_2O_3	976	1077[93]	850[113]	1[114]	2.4[114]	12.8[113]
Lu_2O_3	976	990[113]-1105[113]	820[85]	1.3[85]	3[113]	12.5[85]
S-FAP	905, 985	1047[115]	1260[115]	6[85]	10[116]	2[115]

TABLE 4.1: Overview of some material properties for selected Yb-doped host crystals. κ is the thermal conductivity for an undoped sample.

Regarding the lasing wavelengths, Table 4.1 states the shortest and longest wavelengths where relatively efficient lasing has been achieved, i.e. with an optical efficiency of at least ~10 %. Less efficient lasing at odd wavelengths may well be interesting from a physical point of view, see for example Refs. 104 and 117, but this does not prove that the crystal is a suitable material for lasing at those wavelengths. Also, the special case of lasing on the zero-phonon transition has not been included. On the other hand, for the case of YAB, the shortest wavelengths that can be reached through self-frequency doubling with significant optical efficiency have been included. Here, it is worth mentioning that a wavelength of 1139 nm can also be reached through self-Raman conversion in the double tungstate Yb:KLuW.[96] Finally, it is noteworthy and a bit surprising how much the absorption cross-sections of YSO and GSO differ.

4.2 Laser experiments with the basic cavity

The basic cavity first constructed was used as a base and reference for all the other Yb-based cavities constructed in the thesis work. As laser medium, an antireflection (AR)-coated $3 \times 3 \times 3$ mm^3 crystal of 5 % (~$2.8 \cdot 10^{20}$ cm^{-3}) Yb:KGW was used. This crystal was pressed from two sides into a water-cooled copper holder, using indium foil to fill out possible air gaps. A crystal with a smaller cross-section, perhaps also shaped as a rod or slab, could have improved the heat removal properties. On the other hand, all crystals proved to be quite inhomogeneous so ordering a smaller sample meant a risk of not finding an ideal crystal section. Since KGW is very anisotropic, the crystal orientation is an important issue which will be exemplified in later parts of the thesis. In the basic cavity, the crystal was cut for propagation along the dielectric axis $\mathbf{N_p}$.

The pump laser and focusing system was the same as has been described in Section 3.3. With the laser at maximum operation temperature, the laser wavelength at threshold was just below 980 nm and at full power the wavelength was around 981 nm. Consequently, the absorption coefficient varied with pump power. With the pump polarization aligned along the $\mathbf{N_m}$-axis, the absorption spanned from 85 % near threshold to 93 % at maximum power. The maximum pump power transmitted through the flat input coupler was 19.3 W.

Different concave output couplers where evaluated in the cavity and it turned out that the shortest available radius of curvature (ROC) of 50 mm together with a cavity length of ~20 mm gave

the best results. This gives a cavity mode radius inside the crystal of 70 µm with variations around ± 5 µm due to the different thermal lens strengths at different power levels. In this way, the cavity mode radius matches the narrow direction of the pump focus well but is smaller than the wider direction. However, the effect of this is hard to predict since the pump beam twists through the focus due to the beam shaping optics.

With this cavity, the maximum output power was just above 9 W with a threshold of 4 W. To increase the output power of the cavity and explore the damage threshold limits, the crystal was taken to Berlin for experiments with a 50 W fiber-coupled diode-bar pump source. The wavelength of this bar varied more expressively with pump power and spanned from 973 nm near threshold to 980 nm. Absorption was also reduced compared to the original pump as a consequence of the non-polarized output from the fiber-coupled source. Still, with more incident power available, the maximum output power now rose to 12.4 W before crystal fracture. The slope efficiency in terms of incident pump power also rose to 74 %, but this is largely an apparent effect due to the strong increase in absorption with pump power. The output power characteristics can be seen in Fig. 4.2.

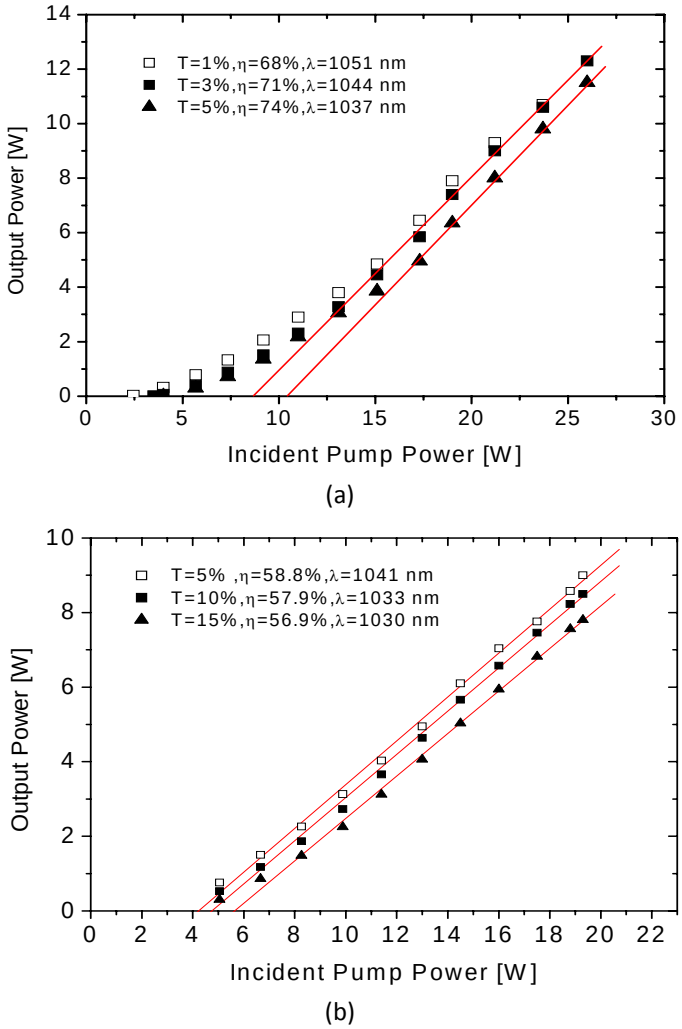

FIGURE 4.2: The input-output power characteristics for the b-cut 5 % Yb:KGW microchips using (a) the fiber-coupled diode and (b) the non-fiber-coupled diode, respectively. T is the output coupler transmission.

While the slope efficiency tells a lot about the scalability of the laser, as long as severe thermal problems are not encountered, the actual efficiency of the laser is best described by the optical efficiency. The optical efficiencies for the constructed lasers are given as functions of incident power in Fig. 4.3. As could be expected due to the higher absorption, the optical efficiency using the non-

fiber-coupled pump was higher for the same incident power. However, the final efficiency at the respective maximum power is 47 % for both pump lasers.

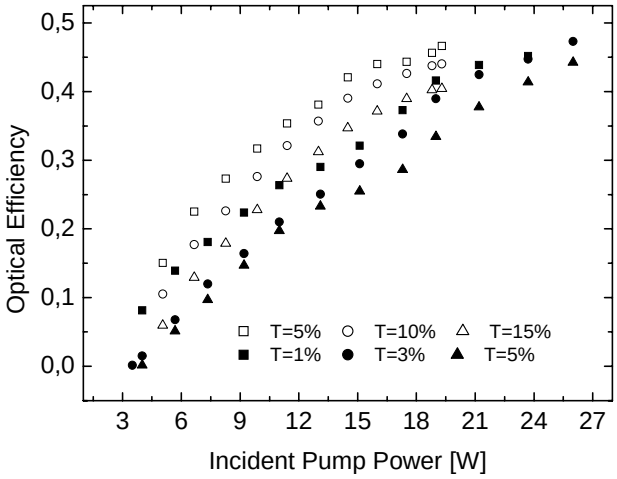

FIGURE 4.3: The optical efficiencies of the fiber-coupled pump scheme (solid symbols) and the non-fiber-coupled pump scheme (open symbols), respectively.

4.3 Reducing the thermal lens in Yb:KGW

The thermal lens is a limiting factor for power-scaling in end-pumped lasers.[93] It also decreases the beam quality and reduces the freedom in cavity design already at moderate pump powers. It follows that the measurement and reduction of the thermal lens is a critical issue in these laser systems. One approach to reduce the thermal lens is by propagating along an athermal direction. This is a propagation direction where, using a cavity with external mirrors, there is no change in the optical path length when the temperature of the laser crystal is increased. Under uniform heating and cooling, this statement together with Eq. 2.15 implies that, if the weaker photoelastic effect is ignored, the following expression is true:

$$\mathbf{x} \cdot (\alpha_T)_{mpg} \cdot \mathbf{x} \cdot (n-1) = -\, dn/dT. \tag{4.1}$$

Here, **x** is the athermal propagation direction, $(\alpha_T)_{mpg}$ is the thermal expansion tensor in the dielectric axes system and dn/dT is a function of the polarization. Under non-uniform heating, it can be seen from Eq. 2.15 that the change in optical path length (OPL) varies depending on the geometry parameter, C_α, as well as the temperature distribution. It follows that no general athermal direction can be defined. Still, it is common to define the athermal direction as the direction that fulfills the athermal condition under uniform temperature distribution. This direction may well be approximately athermal under non-uniform temperature distributions as well, or at least give a reduced thermal lens.

In order to find this athermal orientation, the thermo-optic and thermal expansion tensors have to be measured accurately. The thermo-optic coefficient may be measured by scanning the incident angle until the angle for total internal reflection is found and repeat the procedure for several different temperatures. The thermal expansion coefficients may be measured by uniformly heating the sample in a furnace and measuring the change in length. Using these methods, the tensors in the indicatrix axes directions were found by Biswal et al. to be:[81]

$$\left(\frac{dn}{dT}\right)_{mpg} = \begin{bmatrix} -10 & 0 & 0 \\ 0 & -15 & 0 \\ 0 & 0 & -16 \end{bmatrix} \times 10^{-6} K^{-1} \quad , \quad (\alpha_T)_{mpg} = \begin{bmatrix} 11 & 0 & 7.1 \\ 0 & 2.4 & 0 \\ 7.1 & 0 & 17 \end{bmatrix} \times 10^{-6} K^{-1}$$

Since the thermo-optic coefficient depends on the polarization, so does the athermal orientation. It follows that in order to calculate this orientation, the intended polarization state must first be chosen. Here we choose the polarization to be along the dielectric axis $\mathbf{N_p}$, which should enable the lowest threshold. This sets the right side of Eq. 4.1 as $dn/dT = -15 \cdot 10^{-6}\ K^{-1}$. Now, the athermal vector **x** can be obtained from Eq. 4.1. This calculation gives a propagation direction ~15° clockwise from the dielectric axis $\mathbf{N_m}$. However, there is some uncertainty in the exact angles between the dielectric directions and the crystal lattice.[76, 81] Consequently, the angle to the athermal direction should be somewhere between 15° and 17°.

For the laser experiments with the athermal direction[VI], a 3×3×3 mm^3 sample of 5 % Yb:KGW was cut for propagation at an angle of 17° from the $\mathbf{N_m}$ dielectric axis. This will be referred to as the 'ad-cut' crystal in the following discussion. During the measurements, the basic cavity was used with either the ad-cut crystal or the standard crystal, cut for propagation along $\mathbf{N_p}$. The latter crystal served as a reference and will be denoted the 'b-cut' crystal.

A frequency doubled Nd:YVO_4 ring laser with 30 mW output power and a TEM_{00} beam profile was utilized as a probe beam to measure the thermal lens. The probe beam was introduced collinearly with the pump beam by a dichroic mirror before the laser cavity. The beam waist of the probe inside the crystal was 75 µm ($1/e^2$ radius), which closely matched the cavity mode waist. The near and far fields, respectively, of the probe beam were then imaged onto a CCD camera in order to determine the thermal lens parameters.

While the b-cut crystal was pumped as usual with the diode polarization parallel to $\mathbf{N_m}$, this was not possible in the case of the ad-cut crystal. Instead, this crystal had to be pumped with a polarization parallel to $\mathbf{N_p}$, which gave less absorption. In the ad-cut crystal, the absorption ranged from 42 % near threshold to 55 % at full power. The maximum absorbed power was thus limited to 10.4 W as opposed to 18.1 W with the b-cut crystal.

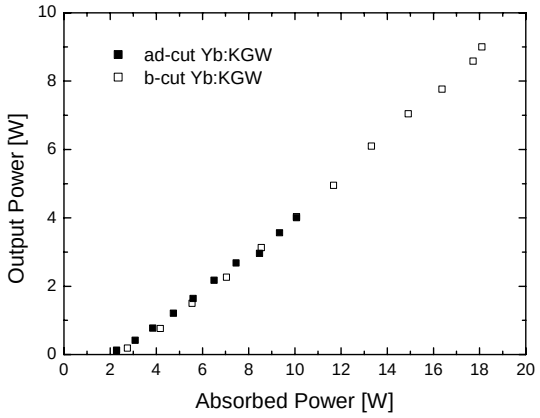

FIGURE 4.4: Output power versus absorbed power for the ad-cut crystal and the b-cut crystal, respectively.

Fig. 4.4 shows the dependence of the laser output power on the absorbed pump power for an output coupler with reflectivity R = 95 %. Both crystals exhibited similar output characteristics, at least up to the maximum absorbed power of the ad-cut crystal. The laser emission was linearly polarized for both crystals with the laser polarization being parallel to the $\mathbf{N_m}$ and $\mathbf{N_p}$ axis for the b-cut and the ad-cut crystal, respectively. The latter is exactly as required in the athermal direction estimations.

Since the lasing wavelengths around 1040 nm are much longer than the fluorescence wavelength of 997 nm in Yb:KGW, especially with respect to the pump wavelength around 980 nm, the thermal load in the crystal is substantially increased when the laser is aligned compared to non-lasing conditions. This is rather uncommon for a laser system, typically the opposite is true.[90] One reason for the more common, opposite situation is the increased absorption under lasing conditions, a factor that remains true also in Yb:KGW. This occurs since the population inversion at lasing

threshold is lower than the non-lasing inversion at pump powers above threshold, a fact that gives less absorption saturation when lasing. The total thermal load increase under lasing conditions can be estimated from the ratio $P_{abs.L}(\lambda_L - \lambda_p)\lambda_F / (P_{abs,NL}\,\lambda_L(\lambda_F - \lambda_p))$ where $P_{abs,L}$ and $P_{abs,NL}$ are the absorbed pump powers for lasing and non-lasing conditions while λ_L, λ_p and λ_F are the average wavelengths of the laser, pump and fluorescence, respectively. For the b-cut crystal the thermal load increases 5-fold while for the ad-cut crystal it becomes 5.6-times larger under lasing conditions. Even though the formula does not take into account the possible changes in the fraction of nonradiative processes or the spectral distribution of the fluorescence, it still gives a strong indication of the situation. The difference was indeed very pronounced in the thermal lens measurements. For this reason, all the thermal lens and beam distortion measurements described in this section have been performed in a well-aligned laser cavity.

Shown in Fig. 4.5 are the far-field profiles of the laser beams for both crystals at 10 W absorbed pump power. The dielectric axes $\mathbf{N_m}$ and $\mathbf{N_p}$ are also indicated. Both beam profiles show a clear astigmatism that is especially pronounced for the b-cut crystal. With this crystal, the long axis of the beam cross-section ellipses, corresponding to the direction of the stronger thermal lens, is rotated by about 32° from the dielectric axis $\mathbf{N_m}$. This direction approximately corresponds to the $\mathbf{X'_1}$ axis of the thermal expansion tensor, as shown in Fig. 4.5(a). This astigmatic behavior becomes even clearer at higher pump powers. It therefore appears that the astigmatism for the b-cut crystal is related to thermal expansion anisotropy. Regarding the ad-cut crystal, on the other hand, the only thermal expansion axis in the cross-sectional plane of the beam is $\mathbf{X'_2}$, which coincides with both $\mathbf{N_p}$ and the direction of strongest thermal lensing. Since the narrower direction of the pump focus is oriented along $\mathbf{N_p}$, the pump geometry could as likely be the reason for the stronger thermal lens in this direction as thermal expansion anisotropy. This view is also supported by the fact that the pump beam has a Gaussian distribution along the $\mathbf{N_p}$-direction but a top-hat distribution in the other direction.

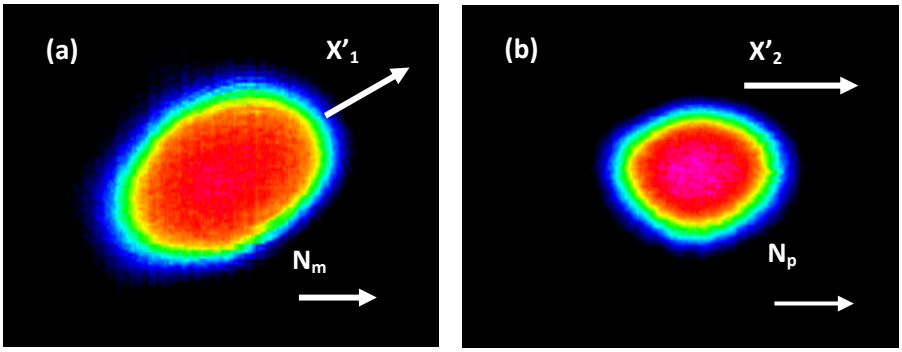

FIGURE 4.5: The far-field profile of the beam at 10 W of absorbed power for (a) the b-cut crystal and (b) the ad-cut crystal. $\mathbf{X'_1}$ and $\mathbf{X'_2}$ are the thermal expansion axes while $\mathbf{N_m}$ and $\mathbf{N_p}$ are dielectric axes.

As described above, the thermal lens as a function of the pump power was measured using a circular TEM_{00} probe beam at 532 nm. In accordance with the far-field images, these measurements revealed astigmatic thermal lenses for both crystals. In the weak lens direction, the changes due to thermal lensing were actually too weak to be accurately measured. In the strong direction, however, which was oriented similar to the far-field images, the thermal lenses were measured and the results are summarized in Fig. 4.6. From this figure, it is evident that the thermal lens of the ad-cut crystal is significantly weaker for the same absorbed pump powers. Moreover, the increase of the thermal lens power with the absorbed pump power in the ad-cut crystal is substantially slower as compared to the b-cut crystal. Note that although the thermal lens is actually measured to be weaker for the b-cut crystal at low pump powers close to threshold, this is a region with a small signal that is very sensitive to measurement errors. It should also be noted that the thermal lens in c-cut KGW, using the same crystal dimensions and 135 µm effective pump spot radius, has been reported to be 11 m^{-1}

for 6.8 W of absorbed power,[90] i.e. close to the measured value for the b-cut crystal but higher than for the ad-cut crystal.

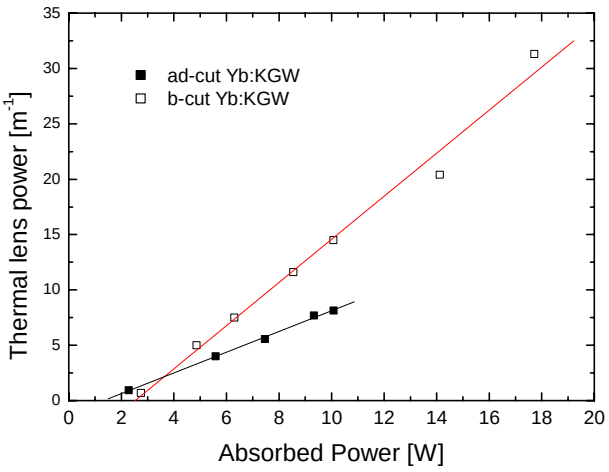

FIGURE 4.6: Dependence of the thermal lens power on the absorbed pump power in ad-cut and b-cut Yb:KGW.

From these measurements it is possible to conclude that the athermal direction gives a reduced and more stigmatic thermal lens. It also seems that, at least for the b-cut crystal, thermal deformation of the crystal should be the dominant effect determining the geometry of the thermal lens. Perhaps the strongest evidence is the fact that the thermal lens is positive, while all the thermo-optic coefficients are negative. Some contributions to the thermal lens may also come from the radial constraint of the thermal expansion through the photoelastic effect. It should finally be stressed that these results apply only to laser medium geometries similar to the one investigated due to the geometry parameter C_α in Eq. 2.15.

Chapter 5
Bragg-grating locked Yb:KReW lasers

5.1 Introduction to volume Bragg gratings

Volume Bragg gratings (VBGs) consist of a sinusoidally varying refractive index modulation that is written in a photosensitive silica glass by UV-radiation and subsequent thermal treatment.[19, 118] This enables both high peak reflectivities and low losses, but the main attraction of these devices is the narrow reflection bandwidth of typically a few hundred picometers. In recent years, people have started to take advantage of these properties to lock and tune diode lasers,[20, 119, 120] solid-state lasers[21-23, VIII, IX] and OPOs.[24, 121] In order to design and optimize such devices, it is desirable to have a solid theoretical understanding of these gratings' behavior under different conditions. This understanding has gradually grown since the pioneering work on plane waves by Kogelnik back in 1969.[122]

The physical situation when a real, finite laser beam is incident on a VBG can be seen from two different perspectives, each leading to its own solution method but yielding much the same results. The first perspective is the plane wave decomposition method,[123-125] where the incident, finite beam is decomposed into its corresponding plane wave components through the Fourier transform. Since the grating is a linear filter, each component can then easily be treated by Kogelnik's formulas for plane waves. The other perspective is the coupled-waves method, which focuses on the interference between the electric fields inside the grating. Here, the coupled wave equations are solved inside the grating with the appropriate boundary conditions.[124, 126, 127]

These perspectives, however, are generally valid for all periodically structured media and previous research has focused on transmission gratings such as accousto-optical modulators. For the reflection gratings that are of interest in laser locking, these models need to be modified. An extensive general model that is valid for all types of gratings and situations has been derived by Moharam at al.[128] However, to obtain this generality it is inevitable that the model becomes quite cumbersome for practical use and that it gives less insight on how each parameter influences the final result. Therefore, we derived a model that focuses on the specific case of reflection gratings in situations which are relevant for laser locking.[VII] We also performed several experimental series to verify these formulas and to highlight some peculiarities of these gratings in laser cavities. Some of these experiments agree with an earlier study by Hsieh et al,[129] while others present completely new possibilities such as transverse mode filtering. The assumptions of our model, the main conclusions and the experimental investigations will be recapitulated in this section. To conclude the recitation of published papers in this field, it is worth mentioning a theoretical investigation into the consequences of VBG deformation.[130] Such deformation might occur when a high-intensity beam is incident on the grating, e.g. the oscillating field inside a high-power laser cavity with low outcoupling.

The principal parameters of our model are defined in Fig. 5.1(a). We consider an incident beam with an electric field $M_{in}(\mathbf{r})$, a vacuum wavelength of λ and a propagation vector, $\mathbf{k}_M$, which makes an angle θ with respect to the z-axis. The reflected beam has an electric field $N(\mathbf{r})$ and a propagation direction defined through the Bragg condition, $\mathbf{k}_N = \mathbf{k}_M - m\mathbf{K} + 2\delta$, where m is the reflection order and δ is a small wavevector mismatch according to Fig. 5.1(b). $\mathbf{K} = (0,0,2\pi/\Lambda)$ is the grating vector where Λ is the period of the modulation, $n(z) = n_0 + n_1 f(z)$, with $f(z)$ being a periodic function. (u, v, q) and

(*u'*, v', *q'*) are rotated coordinate axes defined along the propagation direction of *M* and *N*, respectively, and the far field angles are (χ,ψ) = (*u*/*q*, *v*/*q*) for the *M*-beam, while the same primed variables are used for the reflected beam.

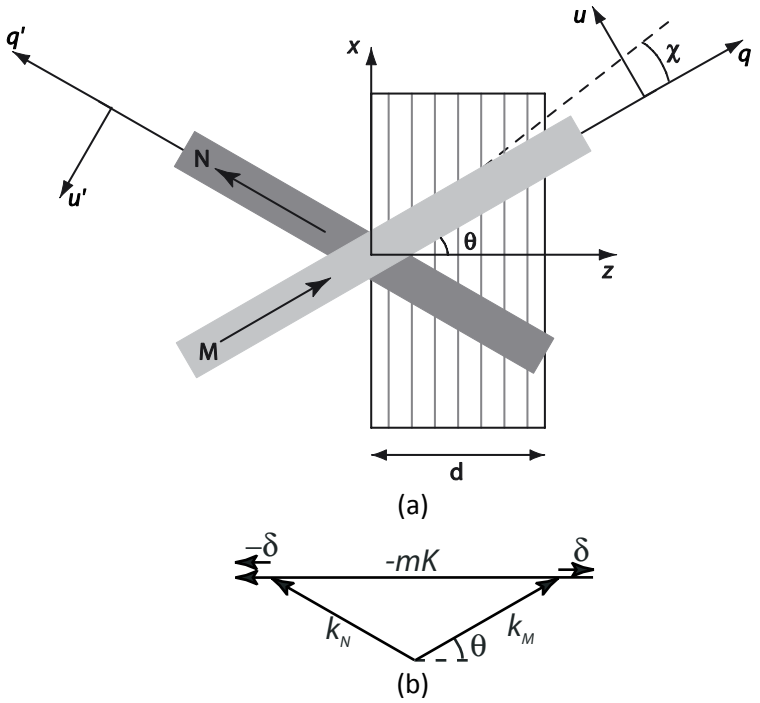

FIGUR 5.1: Illustration of the setup and definitions of coordinates in both (a) real space and (b) momentum space.

Apart from the implicit assumptions in the parameter definitions, there are a few more assumptions in the model. First, the grating is assumed to be surrounded by a medium with refractive index n_0. This is no real limitation, since refraction and reflection at the surfaces can easily be dealt with separately from the grating calculations. Second, the grating is assumed to have infinite extent in the *xy*-plane, which is valid as long as the diameters of the beams projected onto the grating boundaries are significantly smaller than the grating dimensions. Third, the light is assumed to be polarized along the *y*-axis, i.e. orthogonal to the plane of incidence (s- or TE-polarized). This polarization is chosen since p-polarized light is much more cumbersome to model, while at the same time, as will become evident from the experiments, it is of less interest for use in a laser cavity.

With these assumptions and parameters, the solutions inside the grating for a plane incident wave are:

$$M(\mathbf{r}) = M_0 t(\delta, z) e^{-i(\mathbf{k}_M + \boldsymbol{\delta})\mathbf{r}}, \tag{5.1}$$

$$N(\mathbf{r}) = M_0 r(\delta, z) e^{-i(\mathbf{k}_N + \boldsymbol{\delta})\mathbf{r}}, \tag{5.2}$$

where $M_0 = M_{in}(x,y,0)$ and:

$$t(\delta, z) = \frac{-\gamma \cosh\gamma(d-z) + i\delta \sinh\gamma(d-z)}{-\gamma \cosh\gamma d + i\delta \sinh\gamma d}, \tag{5.3}$$

$$r(\delta, z) = \frac{\kappa' \sinh\gamma(d-z)}{-\gamma \cosh\gamma d + i\delta \sinh\gamma d}. \tag{5.4}$$

Here, $\kappa' = \pi/(n_1 \cdot \lambda \cdot \cos\theta)$ is the coupling strength and $\gamma = (\kappa'^2 - \delta^2)^{1/2}$. The total power reflectivity becomes:

$$R_{PW}(\delta) = \left|\frac{N(x,y,0)}{M(x,y,0)}\right|^2 = \frac{\kappa'^2 \sinh^2\left(\sqrt{\kappa'^2-\delta^2}\, d\right)}{\kappa'^2 \cosh^2\left(\sqrt{\kappa'^2-\delta^2} d\right)-\delta^2}\,. \tag{5.5}$$

The spectral bandwidth defined as the separation between the two zero reflectivity points closest to the peak can be found for normal incidence as follows:

$$\Delta\lambda = \lambda_B \sqrt{\frac{n_1^2}{n_0^2 \cos^4\theta_0} + \frac{4\Lambda^2}{d^2}}. \tag{5.6}$$

Here, λ_B refers to the Bragg-matched wavelength at normal incidence. Eqs. 5.1 – 5.6 are all valid for the case of a plane incident wave. However, the situation in a laser cavity is typically such that the finite nature of the incident wave must be considered. Through a comparison between our experiments and simulations, an approximate rule-of-thumb for the limit of plane wave validity can be formulated. This limit is taken to be when four times the divergence angle of the e^{-2} intensity radius of the beam just fits within the zero-to-zero angular bandwidth. For normal incidence, the condition then becomes:

$$\frac{\pi^2}{4} n_0^2 \frac{w^2}{\lambda_B^2} \frac{\Delta\lambda}{\lambda_B} > 1\,. \tag{5.7}$$

Here, *w* is the beam waist, as measured in air for increased applicability. For oblique incidence the condition becomes:

$$\frac{\pi}{4} n_0 \frac{w}{\lambda_B} \frac{\Delta\lambda}{\lambda_B} > \sin\theta_0\,. \tag{5.8}$$

When the respective condition is not fulfilled, a model for finite beams is required. Such a model can be based on either one of the perspectives described above, with basically the same result. The solutions for the far-fields derived via the coupled-wave method can be written as:

$$M_{ff}(\chi, \psi) = C \cdot M_0^{if}(\beta\chi, \beta\psi) t(\delta'(\beta\chi\cos\theta, \beta\psi), d), \tag{5.9}$$

$$N_{ff}(\chi', \psi') = C' \cdot M_0^{if}(-\beta\chi', \beta\psi') r(\delta'(-\beta\chi'\cos\theta, \beta\psi'), 0), \tag{5.10}$$

where:

$$\delta'(\beta\chi\cos\theta, \beta\psi) = \beta\chi\sin\theta + \frac{1}{2}\beta\left(\chi^2\cos\theta + \frac{\psi^2}{\cos\theta}\right) + \delta. \tag{5.11}$$

Furthermore, β is defined as the absolute value of $\mathbf{k}_M$ and M_0^{if} is the inverse Fourier transform of $M_0(u,v,q_0)$ where q_0 is the q-coordinate of the beam waist. C and C' are normalization constants. Finally, it is worth mentioning that, as a consequence of the relation illustrated in Fig. 5.1(b), the wavelength experiencing the highest reflectivity varies with incidence angle as $\lambda_{max} = \lambda_B \cdot \cos\theta$. This can be used for laser tuning, which will be demonstrated in Section 5.2.

To illustrate some properties of VBGs that are of importance for locking and tuning lasers, a series of experiments and simulations will be presented in the following discussion. Particularly, the degradation of some grating parameters with increased incidence angle is of utter importance for the laser designs described in Section 5.2. One main objective is to explore the limits where the gratings are no longer useful as laser elements. Generally, this means that the beam waist of the cavity mode closest to the grating has to be made wide enough to avoid serious degradation of the grating's abilities.

For the experiments, we used a Ti:sapphire laser that was focused through different lens systems. Polarization control of this laser was established by a $\lambda/2$ wave-plate and a Glan-Taylor

polarizer. All beam waists were measured by the knife-edge method. These measurements were performed in air, so the beam radii ($1/e^2$) given below always refer to this medium. All angles of incidence, however, are the calculated internal angles inside the grating, i.e. θ.

Two different VBGs were employed, both of which were AR-coated. Grating A was 0.86 mm thick and had a peak reflectivity of 60 % at 975.3 nm for plane waves. The FWHM bandwidth of this grating was 0.45 nm, corresponding to an index modulation of $n_1 = 3.7 \cdot 10^{-4}$ with a period of $\Lambda = 325$ nm. Grating B was 1.4 mm thick with 97 % peak reflectivity at 1063.4 nm and a bandwidth of 0.55 nm. This corresponds to a modulation $n_1 = 5.8 \cdot 10^{-4}$ and a period of $\Lambda = 355$ nm.

The perhaps most critical parameter, at least for an intracavity VBG, is the reflectivity. If the beam waist is too small, the reflectivity will drop rapidly at oblique angles of incidence. This is illustrated for grating A in Fig. 5.2. The solid symbols represent the measurements for s-polarization and the solid lines show the corresponding simulation. It appears that the model agrees well with reality. The empty symbols show the measurements using p-polarization. It is clear that with this polarization, the reflectivity decreases faster with increasing incidence angle. Consequently, s-polarization should be used in laser applications whenever possible. For comparison, we also give the plane-wave result and the limits of plane wave validity according to the rule-of-thumb condition for different beam waists, see Eq. 5.8. Note that for a beam waist radius around 260 µm, there is no significant reduction of reflectivity. It follows that as long as the waist is kept above this limit, grating A should work well at oblique incidence. Naturally, this limit can be expected to vary for different gratings but can be found through simulations with a good reliability.

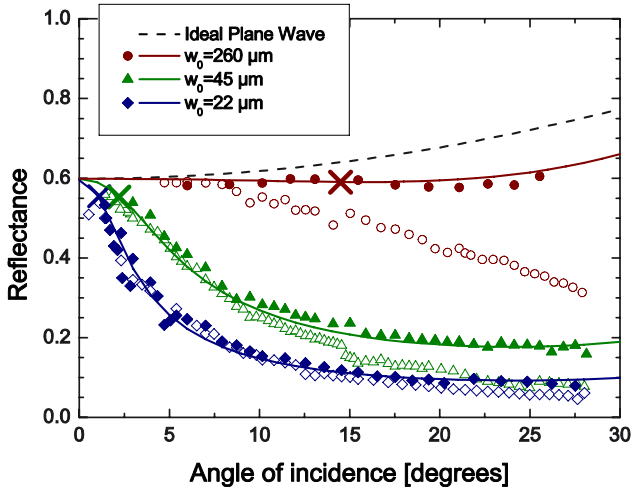

FIGURE 5.2: Reflectivity dependence on incident angle for various beam waists using grating A. Experiments with s-polarization (filled symbols) and p-polarization (empty symbols) as well as theoretical simulations for s-polarization (lines) are given. The approximate limits of plane wave theory as given by Eq. 5.8 are indicated with crosses.

Another important parameter is the reflectivity bandwidth. As can be seen in Fig. 5.3, this parameter increases with increased angle of incidence. In this figure, the FWHM bandwidth of grating A for different beam waists with s-polarization is shown, together with the model predictions and the rule-of-thumb limits. The correlation between the measurements and the model is fairly good, even though the uncertainties in these measurements are larger than for the reflectivity since the reflection spectrum curve is very steep close to the half maximum value. Once again, there is no significant degradation for a beam waist of 260 µm.

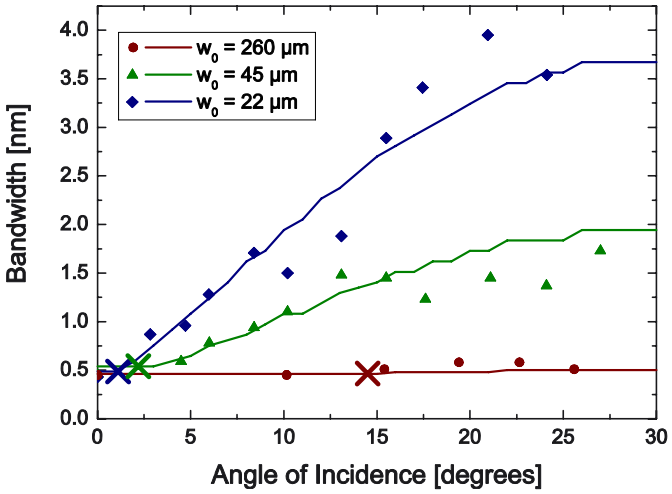

FIGURE 5.3: The reflectivity bandwidth dependence on incident angle for various beam waists with s-polarization using grating A. Experimental results are presented with symbols and theoretical simulations with lines. The approximate limits of plane wave theory as given by Eq. 5.8 are indicated with crosses.

For the case of normal incidence, both measurements and simulations agree that the plane wave theory is valid unless the waist is exceptionally small, < 20 µm. This also corresponds well to the rule-of-thumb limit.

In cases where the reflective abilities of the grating are reduced, the transverse beam profile is also altered by the grating. This is true for both the reflected and the transmitted beams. The reason for this can be understood from the plane wave decomposition point of view, by noting that different plane wave components of the beam will experience different reflectivities. The beam profiles were measured experimentally by the Ti:sapphire laser and a CCD-camera. Several filters had to be placed in front of the camera and interference as well as thermal effects in these filters significantly distorted the measured profiles. Even so, these profiles constitute a good indication of the general features of the real beam profiles.

Fig. 5.4 shows selected beam profiles for the far-fields when using grating B at an oblique angle. In these measurements, $\theta = 16°$ and w = 165 µm. It can be clearly seen how the plane wave components that fit under the acceptance angle of the grating are reflected, while the rest is transmitted.

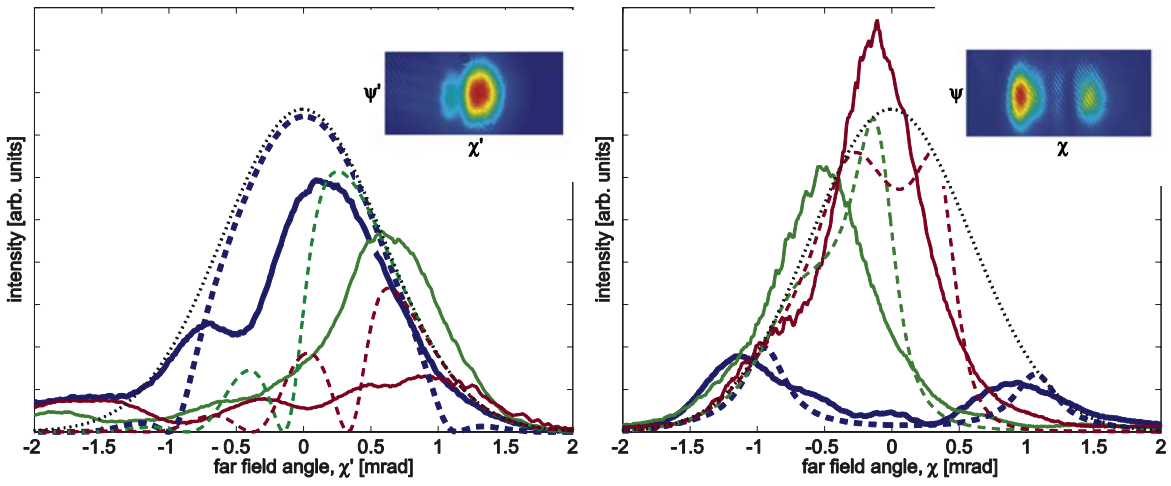

FIGURE 5.4: Transverse far-field intensity distribution at oblique incidence for reflection (left) and transmission (right) using grating B. The wavelengths range from perfect Bragg matching at 1019.9 nm (blue) to 1020.2 nm (green) and 1020.3 nm (red). Experimental data is shown as solid

lines while dashed lines indicate the theoretical predictions. The incident beam profile is given by the dotted line. Insets give the experimental beam profiles at 1019.9 nm.

It is also possible to use the gratings as transverse mode filters. Since higher-order modes have a broader angular spectrum, the incident beam waist can be adjusted so that higher-order modes are transmitted to a significant degree, whilst the TEM_{00} mode still experiences the peak reflectivity. For oblique incidence, as illustrated in Fig. 5.5, this can be achieved at fairly moderate beam sizes. Since this will only work in the oblique direction, however, two gratings have to be used in order to achieve complete mode filtering. Alternatively, strong focusing at normal incidence can be employed. For example, this method for mode filtering could potentially be used to enforce single transverse mode operation in a laser while at the same time locking, and possibly tuning, the wavelength. In such an application, the effect would be further enhanced by the changes in transverse beam profile that accompanies the reflectivity reduction.

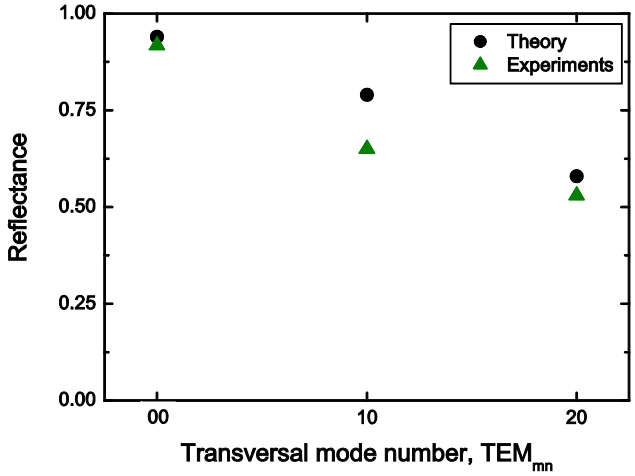

FIGURE 5.5: The reflectivity of grating B for some transverse modes at 1020 nm wavelength (θ = 16°) and with a TEM_{00} beam waist of 255 µm.

5.2 Tuning of Yb:KReW lasers with volume Bragg gratings

A direct approach for wavelength tuning with a VBG is by changing the grating temperature. Through thermal expansion and the thermo-optic effect, a temperature raise causes a red-shift of λ_B. Nevertheless, the shift that can be obtained in this way is limited to a few nanometers at most. Typically, this shift is instead an involuntary phenomenon that occurs when the laser oscillation heats the grating through a low, however existent, absorption in the glass. Extensive tuning is only possible by rotating the grating, thereby modifying the angle θ. Since this will cause a deviation of the reflected beam, the first tuning experiments involved constant realignment of the setup.[24]

To avoid this inconvenience, the grating was positioned next to an HR-mirror in a retroreflector setup[31] which enabled continuous tuning of an Yb:KYW laser[VIII, IX] by simply rotating the retroreflector. Compared to other tuning methods, such as etalons,[V] prisms[105] or birefringent filters,[103] VBGs offer the potential advantage of much higher loss dispersion. High loss dispersion is sometimes necessary to select the desired wavelength when a nearby wavelength has a significant advantage in round-trip gain from the rest of the cavity. Moreover, a VBG has an infinite free spectral range. In other words, the minimum of the loss function occurs for a single wavelength only. This is in contrast to e.g. etalons, where the loss minimum repeats itself periodically.

For the cavity design of the VBG-tuned Yb:KYW laser, three things had to be taken into consideration. First, the beam radius in the crystal had to be kept equally small as in the basic cavity described in Section 4.2, to avoid high thresholds due to the three-level nature of Yb lasers. Secondly, there had to be a beam waist closer to the grating with a radius of at least ~300 µm according to the insights discussed in Section 5.1. Thirdly, since the best available grating had a reflectivity of merely 97 %, a high output coupling was needed to reduce the fraction of the oscillating field lost through

the grating transmission. To properly match these considerations, we constructed a folded cavity with an ROC of 200 mm folding mirror and a total length of 470 mm. This cavity is depicted in Fig. 5.6(A). To avoid astigmatism in the folding mirror, the incidence angle on this mirror was kept below 3.5°.

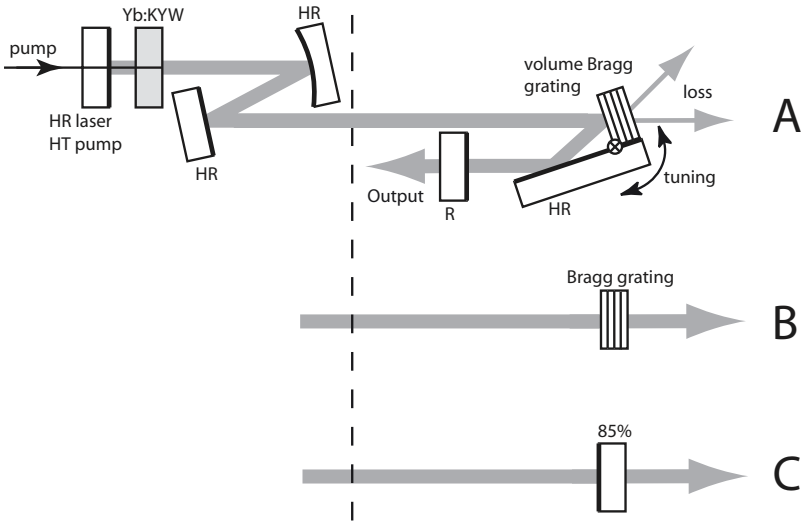

FIGURE 5.6: The different laser setups of the VBG-tuned laser.

The pump laser, focusing optics, input coupler and crystal with holder were all the same as in the experiments described in Section 4.2, except that an Yb:KYW crystal was now used instead of an Yb:KGW one. The polarization at the grating could be changed between p-polarization and s-polarization by rotating the laser crystal and simultaneously rotating the pump polarization so as to maintain the same pump absorption. The VBG had a peak reflectivity of 97 % at 1063.5 nm and a FWHM of 0.55 nm. The facets were slightly tilted compared to the grating direction as well as AR-coated, in order to avoid parasitic reflection effects. The HR-mirror of the retroreflector was specified to be HR between 1010 nm and 1050 nm for the corresponding incidence angles from 63° to 77°. A flat mirror with reflectivity R_1 was used as output coupler. In some experiments aiming at investigating the longest achievable wavelength, the grating was employed at normal incidence, as illustrated in Fig. 5.6(B), and used as an output coupler. Finally, as a reference cavity, a flat mirror with 85 % reflectivity replaced the retroreflector to form a standard cavity for reference, as illustrated in Fig. 5.6(C).

The general laser wavelength was measured by a spectrometer, while a flat-flat scanning Fabry-Perot interferometer was used for resolving the finer details. Fig. 5.7 shows a typical trace containing three Fabry-Perot orders. Evidently, the spectrum consists of two, sometimes three, distinct peaks with a separation of 10 GHz (35 pm) that sets the laser bandwidth. This structure was seen at all wavelengths and the peaks moved continuously when the laser was tuned. If the peaks were caused by an etalon effect somewhere in the cavity, the laser should instead be expected to jump from peak to peak. Consequently, we believe that the peaks correspond to the longitudinal modes of the entire cavity. Since the spacing between these modes, 0.3 GHz, is too small to be resolved, the peaks seem to move continuously. The presence of two peaks can be attributed to spatial hole-burning, allowing two non-neighboring modes to lase simultaneously.

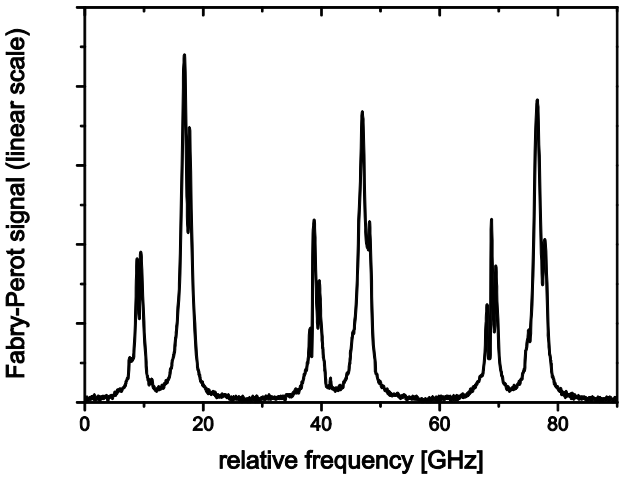

FIGURE 5.7: A typical trace from the Fabry-Perot measurements showing three orders of the double-line laser spectrum at 1030 nm with a line separation of approximately 10 GHz.

The tuning behavior, presented in Fig. 5.8, clearly shows the advantage of using s-polarized light at the grating. The tuning range is similar for both polarizations, between 997 nm and 1040-1050 nm depending on the mirror reflectivity. The output powers, however, are higher for s-polarization, especially in the peak region around 1020-1040 nm. The difference in output power between the two polarizations is a consequence of the differences in grating reflectivity at oblique incidence that give different losses due to the transmission through the grating. At the same time, the similarity of the tuning ranges is not surprising since this range is limited by other factors. At short wavelengths, for instance, the tuning range is limited by the rapidly increasing input coupler transmission. This transmission goes from 0.5 % at 1010 nm to 5 % at 1000 nm and 25 % at 995 nm. At long wavelengths, on the other hand, the tuning range is limited by a reduced gain that can no longer match the output coupling. In the end, at even longer wavelengths, the tuning range would also be limited by geometrical losses when the incidence angle on the grating becomes so small that the reflected light misses the HR-mirror of the retroreflector. To still show that VBGs can be used to enforce lasing at longer wavelengths in Yb:KYW, the grating was rotated to normal incidence following the design from Fig. 5.6(B). Here, with lower output coupling and thereby higher intracavity powers than before, the temperature drift mentioned earlier became noticeable. Thus, the wavelength close to threshold was 1063.43 nm and the wavelength at the maximum output power of 3 W was 1063.71 nm. With a wavelength tuning of 0.01 nm/K,[22, 24, 119] this gives an estimated heating of the grating by 30 K.

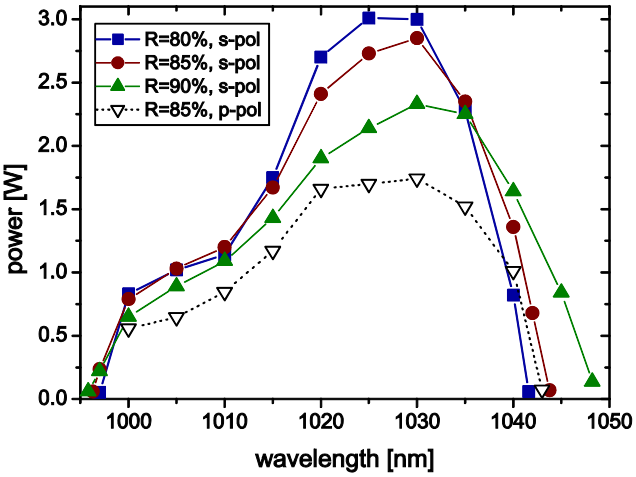

FIGURE 5.8: Laser tuning behavior for different output couplers and polarizations.

From the laser output measurements and simultaneous measurements of the power transmitted through the grating, the grating reflectivity can be calculated. Such results are given in Fig. 5.9 and they agree well with the theoretical predictions. Note also that above 1040 nm, the difference between s- and p-polarizations is quite small and both are close to the value at normal incidence. This is the reason why the long wavelength limit is set mostly by the output coupler reflectivity.

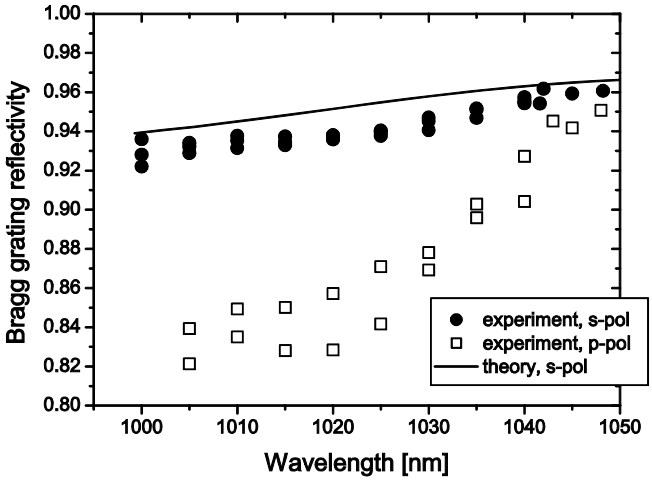

FIGURE 5.9: Volume Bragg grating reflectivity deduced from the laser experiments for both polarizations, as well as theoretical predictions for s-polarization assuming a beam waist w = 280 µm and M^2 = 1.1.

Concerning the beam quality, we measured an M^2 < 1.1 in all measurements with s-polarization and cavity A, while for p-polarization we measured an M^2 < 1.3. The slightly higher value for p-polarization might be related to noticeable beam profile changes at the grating, just prior to outcoupling, similar in behavior to, but weaker than, those shown in Fig. 5.4. For the normal incidence experiments at 1063.5 nm wavelength, we measured M^2-values between 1.3 and 2.2. In this case, the decrease in beam quality can be attributed in part to a larger quantum defect causing a stronger thermal lens and in part to a substantially higher circulating power that heats and deforms the grating.

To further improve this laser design, a direct possibility would be to increase the grating reflectivity. This would allow for less output coupling and, consequently, tuning to longer

wavelengths. Also, if a grating that is designed to reflect longer wavelengths at normal incidence is used, even longer wavelengths could be reached when tuning. Furthermore, since the reflectivity in our design is decreasing slightly even for s-polarized light, a larger beam waist close to the grating, i.e. at the flat output coupler, should be used. Theoretical predictions suggest a waist radius of $w >$ 440 µm, however, this would require a grating with a larger clear aperture than the one available to us. Therefore, in the experiments so far, we have been restricted to $w \approx 280$ µm. As a final note, tuning to shorter wavelengths would require a better input coupler. This issue is dealt with in Section 5.3.

The main objective of these experiments was to demonstrate the potential of VBG-tuning. Compared to other tuning results in Yb:KYW,[103] it seems that this method can indeed reach at least the same tuning range and output powers. However, there are other Yb-doped materials with even wider tuning ranges, such as Yb:Gd_2SiO_5[105] or Yb:Lu_2O_3.[114] Such materials, as well as various non-Yb materials, might well be interesting for VBG-tunable lasers.

5.3 Towards the quasi-two-level laser with volume Bragg gratings

The limitations due to the increasing transmission of the input coupler at shorter wavelengths can be overcome by using a VBG as input coupler.[X] In this way, wavelengths close to the pump wavelength becomes available for longitudinal pumping and thus efficient lasing can be established in the low quantum defect region. The lowest quantum defects reported have been 0.6 % in a thin-disk Yb:KYW laser[103] and 0.8 % in a skew-angle pumped Yb:CALGO laser.[104] At these low quantum defects the output powers have been limited to a few milliwatts. Watt-level output powers have been obtained only at quantum defects of ~1.5 % and only in thin-disk lasers.[103, 113]

For the experiments with a VBG input coupler, a grating with a maximum reflectivity at normal incidence of 99.7 % at 997.5 nm with a FWHM bandwidth of 0.25 nm was used. Such a high-reflectivity grating is rather thick and the total scattering loss of the grating was 2 %. Still, since most of the reflection occurs in the first 10 % of the grating, the loss experienced by the laser cavity at the wavelength peak of 997.5 nm should be limited to 0.2 %. The pump and focusing optics were similar to the basic cavity of Section 4.2, as were the output coupler curvature and cavity length. This cavity is depicted in Fig. 5.10(a).

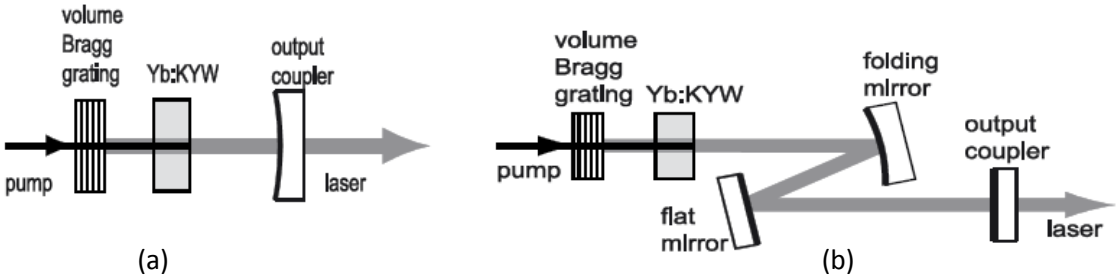

FIGURE 5.10: The experimental setup of both the linear (a) and folded (b) cavity, respectively.

When the laser is forced to operate at 997.5 nm, the lower laser level will be the Stark level closest to the ground level of the $^2F_{7/2}$ manifold. Since these two levels are separated by an energy gap of only 169 cm^{-1}, there will be a substantial 27 % thermal population of the lower lasing level at room temperature. This situation has several consequences for the laser design and performance. First, there will be a significant depletion of the ground state at lasing threshold, causing an absorption decrease from 95 % to 70 %. Secondly, there will be a strong reabsorption in the wings of the pumped region, where the pump intensity is lower. As a consequence, a lower mirror reflectivity and a smaller cavity mode radius in the crystal, w_c, compared to the basic cavity are desired. Finally, with the substantial amount of ions that need to be excited to obtain population inversion, the lasing threshold will be relatively insensitive to output coupling.

In accordance with this reasoning, the best results were achieved using the output coupler with the lowest available reflectivity, R = 85 %. The maximum output power in these experiments

was 2.5 W. To further improve the output performance, even lower reflectivity and/or a smaller w_c was necessary. Due to the lack of suitable mirrors, a folded cavity had to be constructed in order to meet these demands. This cavity is depicted in Fig. 5.10(b). As folding mirror, we initially used an ROC 200 mm mirror that gave a cavity length for maximum stability of 469 mm. In this configuration, w_c remained at ~75 µm, but a series of flat output couplers available could be employed. As it turned out, R = 77 % showed the highest output powers. Replacing the folding mirror with an ROC 150 mm one reduced w_c to ~55 µm. This measure raised the output power to 3.6 W, as shown in Fig. 5.11, using the same R = 77 % output coupler. In both cases, the slope efficiency was ~40 % with regard to incident power and thus 57 % with regard to absorbed power.

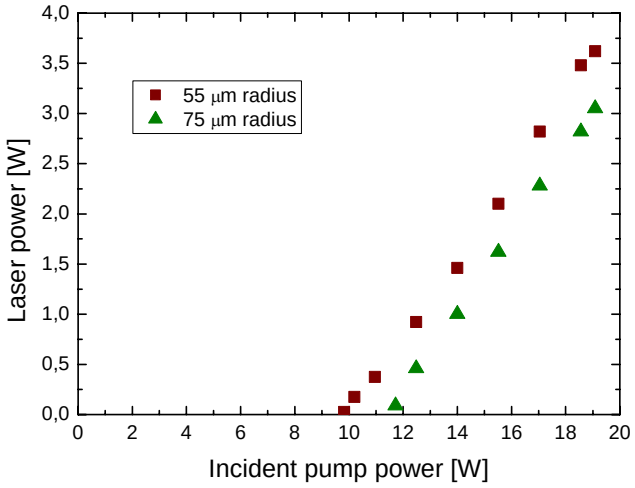

FIGURE 5.11: Laser output power versus pump power for different values of w_c with an R = 77 % output coupler.

Similar to the previous experiments in Section 5.2, the bandwidth was limited to 10 GHz by the separation of the two peaks in the spectrum. Also similar to those experiments with the grating at normal incidence, the lasing wavelength shifted slightly with output power. In this case, the wavelength shifted from 997.68 nm to 997.77 nm. Furthermore, the beam quality was good with M^2 < 1.1 for the w_c = 75 µm experiments and M^2 = 1.3 × 1.7 for the w_c = 55 µm case. The reduced beam quality in the latter case is a reasonable consequence of the mode overlap situation.

The potential advantage of low quantum defect systems is the reduced heat generation and thereby enhanced power scalability. This advantage is illuminated by the following approximate estimation of the potential output power before crystal fracture. For this estimation, we consider the three main sources of heat generation in a laser crystal. The first source, H_1, is nonradiative decay from the upper laser level corresponding to the quantum radiative efficiency, η_r, and the threshold absorbed pump power, P_{th}, according to the formula $H_1 = (1-\eta_r)P_{th}$. The second source, H_2, is the fluorescence quantum defect given by $H_2 = \eta_r.P_{th}(1-\lambda_p/\lambda_F)$ where λ_F is the average fluorescence wavelength and λ_p is the pump wavelength. Finally, there is the heat related to the lasing quantum defect, H_3, which is given by $H_3 = (P-P_{th})\,(1-\lambda_p/\lambda_L)$. Here, P is the total absorbed power and λ_L is the lasing wavelength. Assuming that the total heat generation, $H_1 + H_2 + H_3$, is limited to ~1.1 W,[V] this gives a maximum absorbed power of just above 20 W for lasing around 1030 nm, as opposed to 45 W for lasing at 998 nm. In these calculations, η_r is supposed to equal the value for Yb:KGW, which has been reported to be between 0.96[90] and 0.99.[131] Here, the lower value 0.96 has been used to avoid any over-optimistic predictions. Further assumptions are that the fluorescence is centered at λ_F = 998 nm, that for 1030 nm P_{th} = 2 W[V] and that for 998 nm P_{th} = 7 W as in these experiments. Given that the slope efficiency in terms of absorbed power is 57 %, these figures predict output powers of 22 W. The power could be further improved by reducing the reabsorption loss in the wings of the cavity mode. This means either improving the pump focus or deploying a shorter crystal with higher

doping. Also, for each given pump and laser setup, the wavelength can probably be chosen to optimize the balance between threshold, reabsorption loss and reduced heat generation.

As mentioned in Section 4.1, there is currently a trend in the Yb-doped laser community towards cryogenic temperatures. At such temperatures, low quantum defect lasers would gain additional advantage because of the significant impact given by thermal population of the lower laser level in these systems. This population is 27 % at 300 K but only 5 % at 80 K. The result will be a substantial reduction of the threshold power.

Chapter 6
Polarization-tuning by conical refraction

6.1 Introduction to conical refraction

Conical refraction is an optical phenomenon that occurs when a light beam is propagating along one of the two optic axes in a biaxial crystal. There are two types of conical refraction, external and internal. In external conical refraction, a convergent, unpolarized or circularly polarized beam incident on the crystal will propagate as a collimated beam through the crystal and thereafter diverge again. In internal conical refraction, the situation is reversed and a collimated input beam will diverge in the shape of a cone inside the crystal. After the crystal, the beam will once again propagate in a collimated fashion, in the form of a cylinder, where each segment of the beam cross-section corresponds to a unique polarization. Since internal conical refraction is the type used in our experiments, this chapter will treat this type only. Even so, the physics behind the two types are much the same.

Thorough theoretical treatment of internal conical refraction can be found in references 25-30. Here, the discussion will be limited to the principle explanation for the phenomenon and the presentation of some useful formulas that describe the situation. For this discussion, we will consider plane waves with fields oscillating as $\hat{\mathbf{a}}\cdot\exp[i(\mathbf{kr}-\omega t)]$, where $\mathbf{k} = k\cdot n_{\mathbf{k}}\hat{\mathbf{e}}_{\mathbf{k}}$ is the wavevector, k is the wavenumber and $n_{\mathbf{k}}$ is an allowed refractive index for propagation direction $\hat{\mathbf{e}}_{\mathbf{k}}$. Moreover, $\hat{\mathbf{a}}$ is the amplitude of the respective field, i.e. the electric field **E**, the electric displacement **D,** the magnetic field **B** or the auxiliary magnetic field **H**. Also, ω is the angular frequency and (**r**, t) are the space and time coordinates, respectively. Now, in a medium with a dielectric tensor, $\boldsymbol{\varepsilon}$, and a magnetic permeability equal to that of vacuum, μ_0, it is true that $\boldsymbol{\varepsilon}\mathbf{E} = \mathbf{D}$ and $\mu_0\mathbf{H} = \mathbf{B}$. Furthermore, Maxwell's equations state that $\omega\mathbf{D} = -\mathbf{k}\times\mathbf{H}$ and $\omega\mathbf{B} = -\mathbf{k}\times\mathbf{E}$. By combining these equations, it is possible to obtain an expression that implicitly gives the allowed plane waves in the medium:

$$\frac{\mathbf{D}}{n_{\mathbf{k}}^2} = -\hat{\mathbf{e}}_{\mathbf{k}}\times\hat{\mathbf{e}}_{\mathbf{k}}\times(\varepsilon_0\boldsymbol{\varepsilon}^{-\mathbf{1}}\cdot\mathbf{D}). \tag{6.1}$$

By using a coordinate system with one axis parallel to $\hat{\mathbf{e}}_{\mathbf{k}}$, the solution stating the allowed values of $n_{\mathbf{k}}$ can be derived from the two eigenvalues, $\xi_{\pm}$, to the 2×2 inverse dielectric tensor for the remaining two axes of the coordinate system. This gives:

$$n_{\mathbf{k}\pm} = \frac{1}{\sqrt{\xi_{\pm}}}. \tag{6.2}$$

Typically, for a biaxial crystal, there will be two different eigenvalues corresponding to two orthogonal polarization states with different refractive indices. Now, imagine two sheets in **k**-space, defined through the expression $\omega = k\cdot c_0/n_{\mathbf{k}\pm}$ = constant, as illustrated in Fig. 6.1. These sheets are sometimes called wave surfaces and this term will be used in the following. Since the group velocity is given by $\mathbf{v_g} = \nabla_{\mathbf{k}}\omega(\mathbf{k})$, this velocity, and thus the energy transfer and the Poynting vector for each polarization state, will be directed normally to the corresponding wave surface at each position in **k**-

space. It follows that there will generally be two propagation directions allowed inside the crystal, which is the situation known as double refraction.

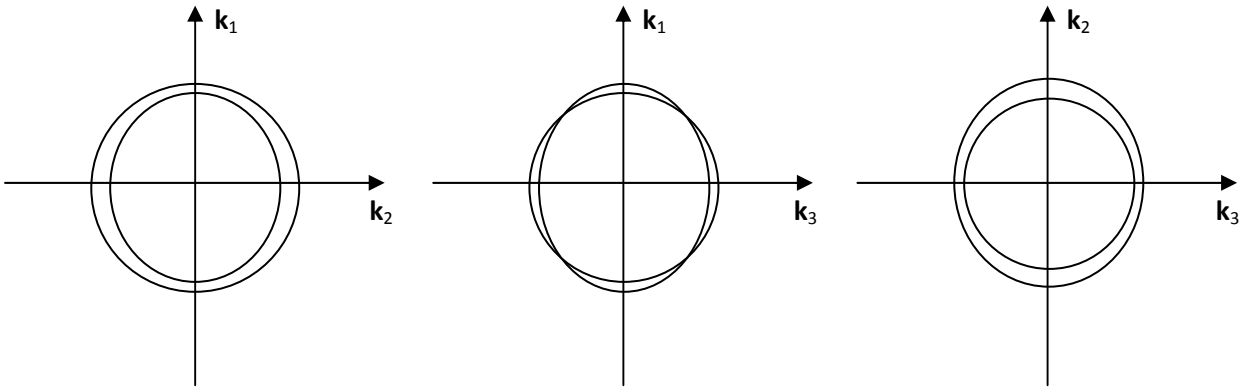

FIGURE 6.1: Three cross-sections of the wave surfaces in a hypothetic crystal where $n_1 < n_2 < n_3$.

In Fig. 6.1 the wave surfaces are given for a hypothetic biaxial crystal. As is vaguely indicated by this figure, there are four points in **k**-space where the wave surfaces intersect. At these points, located along the two optic axes, the eigenvalues are degenerate and there are an infinite number of normals to the combined surfaces. Based on Maxwell's equations and the definition of the Poynting vector, **S**, it is possible to show that at the four points:[30]

$$\mathbf{S} = \frac{cD^2}{\varepsilon_0 n_2^3}\left(\hat{e}_z - \frac{\tan 2A}{2}\left(\hat{e}_x + \hat{e}_x \cos 2\varphi + \hat{e}_y \sin 2\varphi\right)\right), \tag{6.3}$$

where $\hat{\mathbf{e}}_z$ is parallel to the optic axis, $\hat{\mathbf{e}}_y$ is parallel to $\mathbf{k}_2$ and where it is assumed that $n_1 < n_2 < n_3$. The polarization angle, φ, is given by **D** = D[cos φ, sin φ, 0]. These definitions are illustrated in Fig. 6.2.

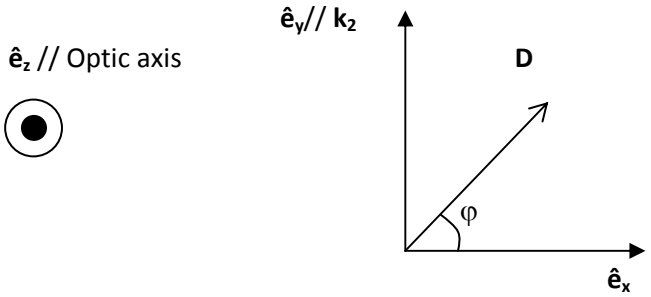

FIGURE 6.2: Definition of the vectors as well as the angle in Eq. 6.3.

From Eq. 6.3 it follows that all possible Poynting vectors together form a skewed cone with half-angle A defined through the expression:

$$\tan 2A = n_2^2 \sqrt{\left(\frac{1}{n_1^2} - \frac{1}{n_2^2}\right)\left(\frac{1}{n_2^2} - \frac{1}{n_3^2}\right)}\,. \tag{6.4}$$

Since the direction of the Poynting vector depends on φ, each cone segment will correspond to a unique polarization. This implies that each polarization state will propagate along a different direction inside the crystal and emerge separated from each other along a ring-shaped structure. After the crystal, the different states will once again propagate in parallel. The situation is illustrated in Fig. 6.3 below.

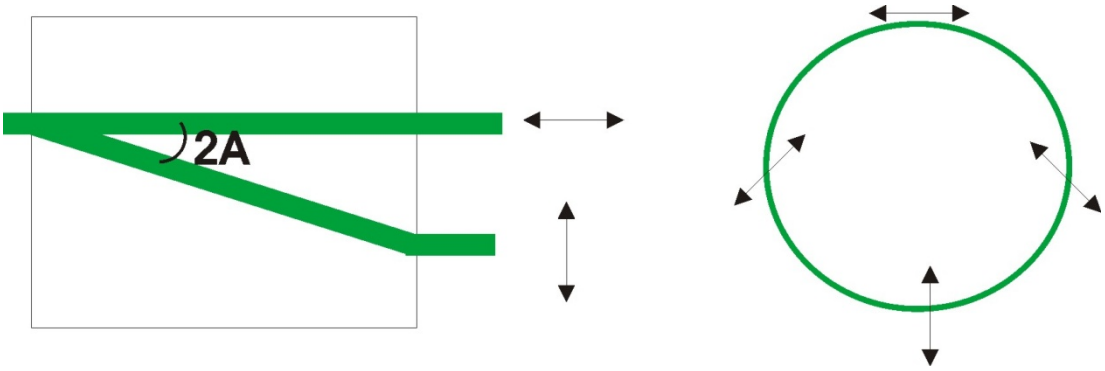

FIGURE 6.3: Illustration of the beam propagation in the case of internal conical refraction. The propagation of the polarization states corresponding to $\varphi = 0$ and $\varphi = \pi/2$ as seen from the side (left) as well as the resulting ring of all polarization states as seen from the front (right).

KGW is one of the materials in which conical refraction have been observed.[30] Here, the dielectric axes follow $\mathbf{N_g} > \mathbf{N_m} > \mathbf{N_p}$, so the optic axes lie in the $\mathbf{N_p}$-$\mathbf{N_g}$ plane at approximately 45° angle from these axes. For the laser experiments under conical refraction conditions, as described in Section 6.2, a 5 % Yb:KGW crystal was cut for propagation along one of the optic axes. To verify that conical refraction is indeed occurring in this crystal, probe experiments were performed using the same single-frequency, TEM_{00}, frequency-doubled Nd:YVO_4 ring laser as previously in Section 4.3.

When investigating conical refraction it is important that the beam radius is significantly smaller than the radius of the ring at the exit surface of the crystal. At the same time, the incident beam should be practically collimated. For this reason, demonstrations of this effect are typically held in long samples of 15-25 mm in length. The length of the laser crystal, on the other hand, was merely 3 mm resulting in a ring radius of 54 µm for 532 nm wavelength. Therefore, a tight focusing of the probe beam was necessary but not too tight considering the beam divergence. This was accomplished by an f = 30 mm lens that gave a beam waist of 25 µm. This focusing was just sufficient to visualize some of the finer details such as the Poggendorf inner ring, seen as a central spot in Fig. 6.4(a).

The crystal was positioned on a rotational stage and the probe beam at the exit surface of the crystal was imaged by an f = 150 mm lens onto a CCD chip. Since the probe beam was polarized, a half-ring pattern was obtained that rotated with the polarization of the beam as shown in Fig. 6.4(a).

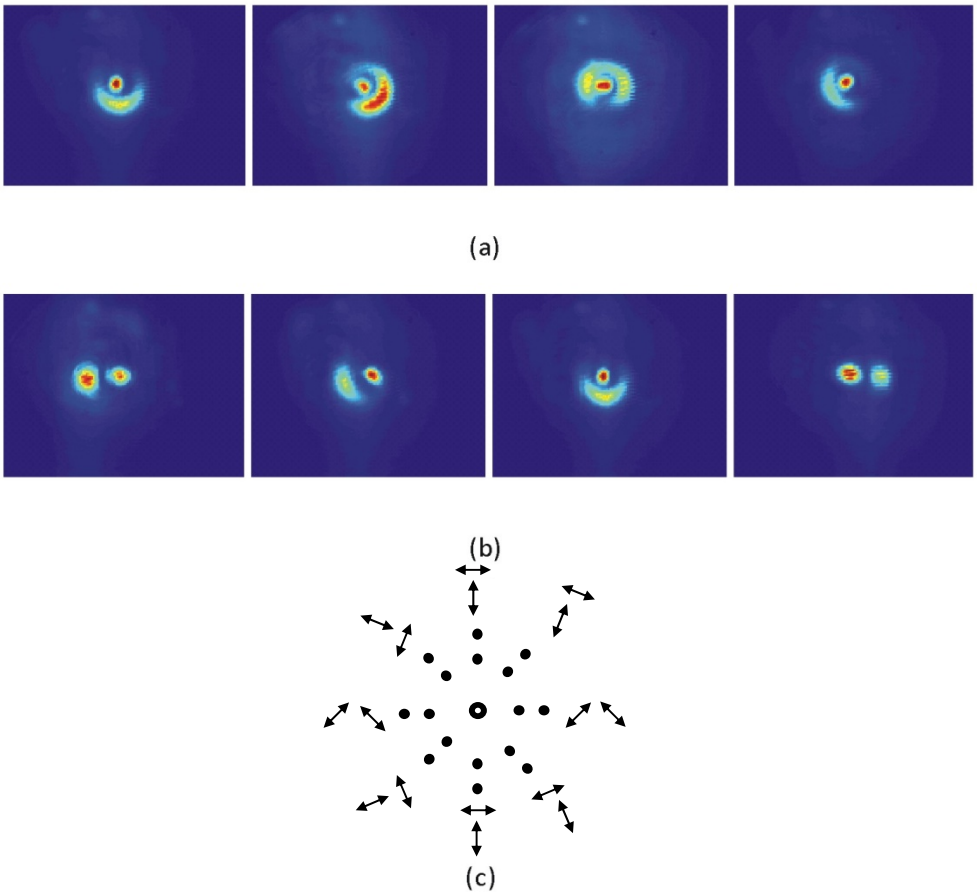

FIGURE 6.4: CCD camera pictures of the probe beam transverse profile at the exit surface of the crystal for (a) different polarization states and (b) different propagation directions. (c) shows a schematic view of how the double refraction spots appear when the crystal is rotated around the optic axis as well as the polarization states of these spots.

The acceptance angle of conical refraction is relatively small. This is illustrated in Fig. 6.4(b) where the crystal is rotated while the polarization is kept constant. The total rotation in this image series was less than 1°, so a slight crystal rotation away from conical refraction will result in a return to common double refraction. Moreover, the orthogonal polarization states of the two double refraction spots will correspond to the polarization directions of the opposite ring segments along the crystal's line of movement. This translation scheme is illustrated in Fig. 6.4(c). In this way, arbitrary double refraction states can be obtained by a slight, controlled crystal rotation.

6.2 Polarization-tuning based on internal conical refraction

The principle behind laser tuning based on internal conical refraction is to use the spatial separation of the different polarization states to establish cavity feedback for a single polarization state only. In a cavity with a flat end-mirror close to the crystal, the cavity mode will have a waist just prior to the crystal and will be practically collimated at the crystal. If the crystal is properly oriented for conical refraction, it follows that the oscillating field propagation in the crystal will depend on the polarization as illustrated in Fig. 6.3. If the cavity feedback from the rest of the cavity is transversally selective, for example by use of a concave mirror, all polarization states except the desired one will experience loss. If these losses are sufficiently high, the laser will operate in a single polarization state. If the losses are intermediate, the laser will operate in a mixed polarization state and if the losses are negligible, compared to the gain anisotropy, the laser will simply operate along the polarization state with the highest gain. If the transverse selectivity of the cavity feedback can be adjusted, e.g. by translating a concave mirror, the polarization state can be tuned accordingly. In the

case where sufficient loss cannot be established to enforce a desired polarization state due to a nearby state with superior gain, the crystal itself can be slightly rotated in the corresponding direction to move closer to, or even into, double refraction where only two states are allowed. In many systems, the same effect can also be achieved by instead translating the pump optics in order to tilt the pump channel inside the crystal. So, by use of internal conical refraction, any polarization direction should be obtainable and even the degree of polarization should be controllable. There is no need for additional cavity components, but for tuning it is necessary to be able to adjust the cavity feedback and possibly even rotate the crystal ~1°.

For the laser experiments on polarization-tuning,[XI] the basic cavity of Section 4.2 was used with two differently oriented 3×3×2 mm^3, 5 % Yb:KGW crystals. The first crystal, denoted the NG-crystal, was cut for propagation along the $\mathbf{N_g}$ dielectric axis. The second crystal, denoted the CR-crystal, was cut for propagation along one of the optic axes. Both crystals were AR-coated and 3 mm long, with the second 3 mm direction parallel to $\mathbf{N_m}$. The pump diode polarization was directed along $\mathbf{N_m}$. The absorption in the CR-crystal was measured to be 90 %, while the absorption in the NG-crystal was found to be 96 %. Small differences in the actual dopant concentration could be the reason for the difference between these crystals, and also for the difference compared to the b-cut crystal of Section 4.2. These two crystals were also delivered by another manufacturer, Vision Crystal Technology as opposed to EKSPLA. An interesting detail is that the color of the fluorescence from upconversion in the unwanted but nevertheless unavoidable lanthanide ions such as Er^{3+} and Pr^{3+} was also different, beautifully indicating a different pollution mix.

With the CR-crystal, the polarization could be tuned by translation of the output coupler. For several polarization states, a small crystal rotation was also necessary, as outlined above. An example of the output power and degree of polarization as a function of mirror position for translation along a straight, e.g. horizontal, line is shown in Fig. 6.5. From this figure, it can be seen that a mirror translation of about 90 µm is necessary to rotate the polarization completely. This is in reasonable agreement with the theoretical calculation of the ring diameter on the exit surface of the crystal, which is 145 µm at a wavelength of 1 µm. Furthermore, this experiment was performed at full power. At lower power levels, the necessary translation distance is reduced since misalignment loss has more impact on the laser system. The laser wavelength varied with the polarization state and was in the 1036-1038 nm region with a FWHM bandwidth of ~0.5 nm.

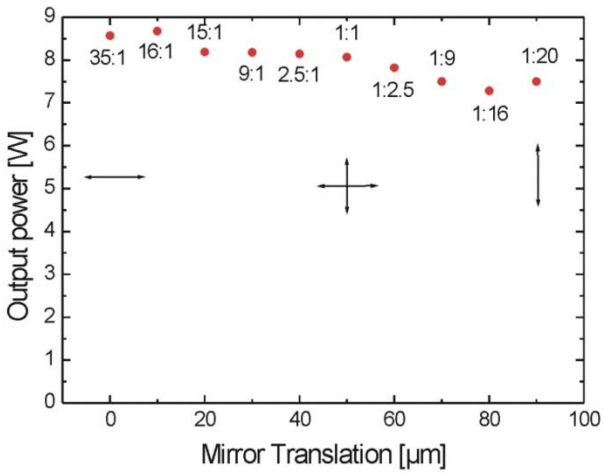

FIGURE 6.5: Output powers and degrees of polarization at different mirror positions for a typical pair of opposite polarization states.

When using the NG-crystal, mirror translations just resulted in a decreased output power. No polarization changes could be observed, just as expected. The polarization state of the NG-crystal was not in the $\mathbf{N_m}$-direction, as for the b-cut crystal, but in the $\mathbf{N_p}$-direction. This could be a bit surprising at first glance, since the cross-sections in the $\mathbf{N_m}$-direction are far higher. However, that is

the situation around the peak at 1025 nm. In Yb-doped systems, the strong reabsorption cause a situation where gain is first established at longer wavelengths. With 5 % output coupler transmission, the NG-crystal operated at 1041 nm, with a FWHM bandwidth of 0.5 nm. In this spectral region, the most advantageous cross-sections giving the lowest threshold are in the $\mathbf{N_p}$-direction.

However, the $\mathbf{N_p}$-direction could not be accessed in the b-cut crystal, since this was the propagation direction. Neither could it be accessed in the CR-crystal. It is, therefore, not surprising that the thresholds of the CR-crystal and the b-cut crystal were rather similar, though slightly lower in the b-cut case, while that of the NG-crystal was substantially lower. Nevertheless, the slope efficiencies of all the crystals were about the same, ~60 % with respect to incident power, as illustrated in Fig. 6.6. For the CR-crystal, the maximum output power was 8.6 W, with 8.4 W in a single polarization direction. The slope efficiency was 60.5 %. For both crystals, the M^2-value near threshold was ~1 and increased to almost 2 at maximum power. This beam quality did not differ noticeably between different polarizations.

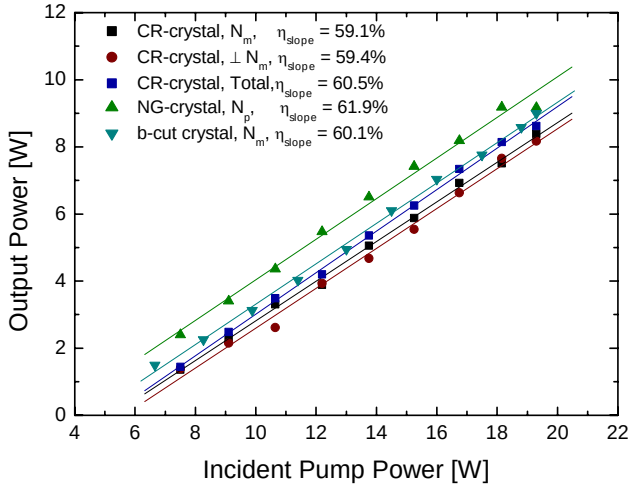

FIGURE 6.6: Output power characteristics for two of the possible polarizations of the CR-crystal, as well as the output power of the NG-crystal and the b-cut crystal for reference.

Judging from the thresholds and slope efficiencies illustrated in Fig. 6.6, it seems that there are no additional losses introduced by this method for complete polarization control. Although an Yb:KGW crystal was used in this first demonstration of a laser operating along the direction of conical refraction, the methodology should be applicable to all biaxial crystals with different dopants. Furthermore, this is also an effective way to enforce unpolarized output from highly anisotropic gain media. For example, this is the first completely unpolarized laser in Yb-doped ordered double tungstates. Looking in the other direction, further improvement of the extinction ratio could be possible by increasing the diameter of the conical refraction ring using a longer crystal or a more anisotropic medium. An equivalent measure would be to reduce the radius of curvature of the output coupler. Such improvements would also reduce the need of a small crystal rotation in some cases to enhance the polarization discrimination.

Chapter 7
Conclusions

The focus of this thesis has been on diode-pumped solid-state lasers incorporating Yb-doped and Er,Yb-codoped laser crystals. Various material configurations, crystal orientations and cavity concepts have been evaluated in order to improve the output power performance, to reduce the bandwidth and to enable spectral as well as polarization tuning.

The crystal Er,Yb:GdCOB has been evaluated in two articles for cw and Q-switched lasing, respectively. In the cw regime, the output performance was good for a crystalline host in a monolithic cavity and not far from typical glass lasers. In the Q-switched regime, the situation was much the same, the performance was close to standard Q-switched Er,Yb:glass lasers but not sufficient to beat the best reported results. To find a crystalline host material that can eventually replace glass, spectroscopic investigations were made into Er,Yb:KReW. These experiments gave the fundament for a mathematical model for optimizing the dopant concentrations that enabled the demonstration of more than 150 mW output power from Er,Yb:KLuW.[132] A spectroscopic investigation was also made into Er,Yb:YAG at elevated temperatures. This revealed that at 600-800 °C, all the important properties such as lifetimes and spectra closely resemble the corresponding values in glass. Still, such high temperatures are probably too high for any practical laser operation.

The major part of the thesis concerns Yb:KReW lasers. A cavity design that served as a fundament and reference for all these lasers was constructed with a compact, longitudinally pumped design. From this 20 mm cavity, 9 W output power at 60 % slope efficiency was typically obtained. At higher power levels the thermal lens was strong, up to 30 m^{-1}. However, this could conveniently be reduced by cutting the crystal for propagation along an athermal direction. In this way, the increase of thermal lens strength with absorbed power could be reduced by a factor of 2.

The introduction of a VBG in the cavity reduced the bandwidth from > 500 pm to 35 pm, limited by spatial hole burning. Furthermore, wavelength tuning could be achieved by employing the VBG in a retroreflector configuration. Such employment involves using the VBG at oblique incidence, which initiates several complications. To understand and overcome these complications, a theoretical and experimental study of the physical behavior in VBGs was undertaken. The insights from this study then enabled the construction of a cavity where wavelengths between 997 nm and 1048 nm could be obtained by rotation of this retroreflector. Potential advantages for this tuning technique are a high modulation, i.e. a strong loss difference between nearby wavelengths, and an infinite free spectral range. With the VBG used as an output coupler instead of retroreflector, the laser was locked at 1063 nm. For such a long wavelength, the gain in Yb:KGW is very low, so this clearly shows the spectral control potential of VBGs. In order to reach shorter wavelengths close to the pump wavelength, on the other hand, the limitation of the increasing input coupler transmission had to be solved. This was done by using a VBG as input coupler. In this way, the output power at 998 nm rose to 3.6 W at a quantum defect of 1.6 %. This is the lowest quantum defect so far for a watt-level, longitudinally pumped laser and the power scaling possibilities promises a significant increase in output power from this type of lasers.

The laser properties of an Yb:KGW crystal cut for propagation along the optic axis were also examined. Here, it was demonstrated how the conical refraction phenomenon could be used to accomplish complete polarization control. The orientation of the polarization could be arbitrarily

tuned and so could also the extinction ratio from completely unpolarized light to 40:1. This tuning could be accomplished without any additional cavity components and with no noticeable decrease in laser performance. The maximum output power was 8.6 W at 60 % slope efficiency. It is worth noting that this is probably the first practical application of a 200 years old discovery as well as the first demonstration of conical refraction in a laser.

Many of the concepts introduced here using Yb:KReW crystals can easily be applied to other host materials as well. The VBG-tuning technique can be applied to for example Ti:sapphire lasers, different glass lasers or other lasers with wide emission spectra. Using a VBG input coupler can be an effective way to get low quantum defects in e.g. Nd-lasers. For example, it has become more and more common to either lase or pump these lasers at the Nd($^4F_{3/2}$) level. A VBG input coupler could enable simultaneous longitudinal pumping and lasing to this level. Finally, polarization tuning by conical refraction should in principle be possible to employ in any biaxial host material such as KReW, ReCOB or YAP.

Chapter 8
Description of work and author contribution

Paper I

Luminescent and laser properties of Yb-Er:$GdCa_4O(BO_3)_3$: a new crystal for eye-safe 1.5-µm lasers

B. Denker, B. Galagan, L. Ivleva, V. Osiko, S. Sverchkov, I. Voronina, J. E. Hellström, G. Karlsson, and F. Laurell, Appl. Phys. B **79**, 577-581 (2004)

This paper presents and evaluates $GdCa_4O(BO_3)_3$, GdCOB, as a crystalline replacement for glass in Er,Yb-codoped systems. Spectroscopic investigations and laser tests on crystals grown by the Czochralski method from platinum crucibles are described. Several pump sources are evaluated; two laser diodes and a Ti:sapphire laser. A continuous-wave output power of 80 mW was achieved in a monolithic microchip cavity under laser-diode pumping. The slope efficiency was up to 15 %. The output power and efficiency were not far from standard glass lasers of similar design.
Contributions by the candidate: The candidate performed the laser experiments using cw diode and Ti:sapphire pumping together with G. Karlsson and the laser experiments using pulsed diode pumping together with G. Karlsson, S. Sverchkov and B. Galagan. The candidate was also responsible for writing the manuscript.

Paper II

Passive Q-switching at 1.54 µm of an Er-Yb:$GdCa_4O(BO_3)_3$ laser with a Co^{2+}:$MgAl_2O_4$ saturable absorber

J. E. Hellström, G. Karlsson, V. Pasiskevicius, F. Laurell, B. Denker, S. Sverchkov, B. Galagan and L. Ivleva, Appl. Phys. B **81**, 49-52 (2005)

This paper evaluates Er,Yb:GdCOB in the passively Q-switched regime. The laser has a monolithic design with the spinel saturable absorber in optical contact with the crystal, a suitable configuration for many practical applications. The laser produced a train of Q-switched pulses with 5-6 ns duration at a slope efficiency of 11.6 %. The maximum output power was 88 mW, limited by thermal fracture.
Contributions by the candidate: The candidate performed the laser experiments using a 2 % loss spinel plate together with S. Sverchkov and the candidate performed the laser experiments using a 3 % loss spinel plate together with V. Pasiskevicius. This constitutes all experimental work in the paper. The candidate was also responsible for writing the manuscript.

Paper III

Fluorescence dynamics and rate-equations analysis in Er^{3+}, Yb^{3+} doped double tungstates

S. Bjurshagen, J. E. Hellström, V. Pasiskevicius, M. C. Pujol, M. Aguiló and F. Díaz, Appl. Opt. **45**, 4715-4725 (2006)

This paper presents a spectroscopic investigation of KGW and KYW crystals with different Er and Yb doping concentrations. Lifetimes have been measured for the Yb ($^2F_{5/2}$), Er ($^4I_{13/2}$) and Er ($^4S_{3/2}$) levels. The Yb ($^2F_{5/2}$) lifetimes are showing a decreasing trend towards the limiting Er ($^4I_{11/2}$) lifetime with increasing Er-to-Yb concentration ratio, whereas the Er ($^4I_{13/2}$) lifetimes are mostly unaffected by the doping concentrations. A rate equations analysis has been performed to explain the observed behavior and the gain is calculated for a continuous-wave laser at 1.53 µm to find the optimum doping concentrations for high gain.

Contributions by the candidate: The candidate performed all of the spectroscopic measurements in the paper together with S. Bjurshagen and V. Pasiskevicius. The candidate actively participated in the discussion to analyze and interpret the results and assisted S. Bjurshagen in developing the mathematical model. The candidate also assisted S. Bjurshagen and V. Pasiskevicius in writing the manuscript.

Paper IV

Yb^{3+},Er^{3+}:YAG at high temperatures: energy transfer and spectroscopic properties

B. Denker, B. Galagan, V. Osiko, S. Sverchkov, A. M. Balbashov, J. E. Hellström, V. Pasiskevicius and F. Laurell, Opt. Commun. **271**, 142-147 (2007)

In this paper we present a spectroscopic evaluation of Er,Yb:YAG at elevated temperatures. The evolution of important lifetimes, energy transfer rates and cross-sections with temperature was investigated and discussed. Interestingly, the measurements reveal that Er,Yb:YAG at elevated temperatures shows spectroscopic properties that are very similar to Er,Yb:glass. Alas, this situation does not arise before temperatures around 600-800 °C, which is probably too high for a practical laser system.

Contributions by the candidate: S. Sverchkov proposed the idea of investigating Er,Yb:YAG at elevated temperatures. All experiments were performed by the group of B. Denker in Moscow and the candidate participated in some of them. The candidate also assisted in writing the manuscript.

Paper V

Efficient Yb:KGW lasers end-pumped by high-power diode bars

J. E. Hellström, S. Bjurshagen, V. Pasiskevicius, J. Liu, V. Petrov and U. Griebner, Appl. Phys. B **83**, 235-239 (2006)

This paper reports on an investigation of the laser performance of Yb:KGW under longitudinal end-pumping by a diode bar. Two different pump schemes are evaluated, one with a non-fiber-coupled pump source yielding an asymmetric but polarized pump spot and one with a fiber-coupled pump source. Both designs resulted in an optical efficiency of 47 % and the output powers were 9 W and 12.4 W with the non-fiber-coupled and the fiber-coupled sources, respectively. In the former case,

the output power was limited by available pump power while in the latter case, the output power was limited by thermal fracture.
Contributions by the candidate: The candidate performed all of the experiments using the non-fiber-coupled pump source together with S. Bjurshagen and V. Pasiskevicius. The candidate participated actively in a discussion regarding the results using the fiber-coupled pump, results which were obtained by J. Liu, V. Petrov and U. Griebner. The candidate also calculated the thermal gradients at crystal fracture. The candidate wrote the manuscript together with V. Pasiskevicius.

Paper VI

Laser performance and thermal lensing in high-power diode pumped Yb:KGW with athermal orientation

J. E. Hellström, S. Bjurshagen and V. Pasiskevicius, Appl. Phys. B**83**, 55-59 (2006)

This paper describes a comparative study of the longitudinally pumped laser performance and thermal lensing between standard b-cut Yb:KGW and Yb:KGW cut along a novel athermal orientation. It is found that thermal expansion dominates the thermal lensing in both crystals and that the thermal lens is about twice as strong in b-cut KGW at 10 W of absorbed power, as compared with the crystal with athermal orientation. The athermally cut crystal also shows a considerably less astigmatic thermal lens. It is further shown that these properties allow for better beam quality in the athermally cut crystal.
Contributions by the candidate: The candidate performed all of the experiments together with S. Bjurshagen and V. Pasiskevicius. The candidate wrote the manuscript together with V. Pasiskevicius.

Paper VII

Finite beams in reflective volume Bragg gratings: theory and experiments

J. E. Hellström, B. Jacobsson, V. Pasiskevicius and F. Laurell, IEEE J. Quantum Electron (in press)

The paper consists of two parts, one theoretical and one experimental. In the theoretical part, we started with the existing models for holographic structures and made appropriate assumptions for, as well as focused the details on, the case of reflective volume Bragg gratings in situations which are relevant for locking and tuning of lasers. In this way we found very suitable formulas to make the necessary simulations when designing tunable Bragg grating-locked lasers. In general, this means that the beam waist closest to the grating has to be sufficiently wide. In the experimental part we confirmed these formulas and highlighted some interesting peculiarities that arise when the beam waist is too narrow. We also showed how the gratings can be used to filter spatial modes as well as spectral ones.
Contributions by the candidate: The candidate performed the experiments together with B. Jacobsson. The candidate, B. Jacobsson and V. Pasiskevicus formulated the theoretical models. The candidate wrote the paper together with B. Jacobsson with assistance from V. Pasiskevicius and F. Laurell.

Paper VIII

Widely tunable Yb:KYW laser with a volume Bragg grating

B. Jacobsson, J. E. Hellström, V. Pasiskevicius and F. Laurell, Opt. Express **15**, 1003-1010 (2007)

Here we present the concept of laser tuning with volume Bragg gratings. This technique is based on employing the grating at oblique incidence in a retroreflector design. As a demonstration, we showed an Yb:KYW laser that was tunable between 997 nm and 1050 nm with a bandwidth < 0.1 nm, which was the resolution limit of the spectrometer. In a single beam with M^2 < 1.3, the maximum output power was 1.7 W. The achievement of 1063 nm lasing when the grating was used at normal incidence constituted an indication of the possibility to reach even longer wavelengths.
Contributions by the candidate: The candidate performed the experiments together with B. Jacobsson. The candidate wrote the paper together with B. Jacobsson with assistance from V. Pasiskevicius and F. Laurell.

Paper IX

Tunable Yb:KYW laser using volume Bragg grating in s-polarization

B. Jacobsson, J. E. Hellström, V. Pasiskevicius and F. Laurell, submitted to Applied Physics B

In this paper we show that the use of s-polarization can significantly improve the power performance of Bragg grating tuned lasers. We obtained a maximum output power of 3 W and a tuning range of 996-1048 nm. The beam quality was excellent with M^2 < 1.1 for the entire spectral range. We also constructed a Fabry-Perot interferometer to resolve the bandwidth. With this interferometer we found that the bandwidth was 10 GHz, limited by the separation of two peaks in the spectrum.
Contributions by the candidate: The candidate performed the experiments together with B. Jacobsson. The candidate wrote the paper together with B. Jacobsson with assistance from V. Pasiskevicius and F. Laurell.

Paper X

Quasi-two-level Yb:KYW laser with a volume Bragg grating

J.E. Hellström, B. Jacobsson, V. Pasiskevicius and F. Laurell, Opt. Express **15**, 13930-13935 (2007)

For longitudinally pumped lasers, it is problematic to obtain low quantum defects since the input coupler has to reflect the laser wavelength while at the same time transmitting the pump beam. In this paper, we solved this problem by using a volume Bragg grating as input coupler. Furthermore, with this method wavelength locking with a bandwidth of 10 GHz was simultaneously obtained. The Yb:KYW laser constructed had an output power of 3.6 W at 998 nm with 1.6 % quantum defect. The threshold in terms of absorbed power was 7 W. This is higher than in conventional Yb:KYW lasers operating around 1030-1040 nm, due to reabsorption loss. However, estimation on power scaling indicates that the possible output power before thermal fracture will be higher due to the substantially reduced heat generation.
Contributions by the candidate: The candidate performed the experiments together with B. Jacobsson. The candidate wrote the paper together with B. Jacobsson with assistance from V. Pasiskevicius and F. Laurell.

Paper XI

Polarization-tunable Yb:KGW laser based on internal conical refraction

J. Hellström, H. Henricsson, V. Pasiskevicius, U. Bünting and D. Haussmann, Opt. Lett. **32**, 2783-2785 (2007)

In this paper we introduce a new method for polarization tuning that is based on internal conical refraction. With this method, there is no need for any additional cavity elements and tuning can be achieved by e.g. a slight translation of the output coupler. Both direction and extinction ratio of the polarization can be arbitrarily altered. We have demonstrated this method with an Yb:KGW laser where we obtained a maximum output power of 8.6 W at a slope efficiency of 60.5 % in terms of incident power. This is in good agreement with a standard Yb:KYW laser used for reference. The extinction ratio could be varied from completely unpolarized output to 40:1. This is probably the first application of internal conical refraction since the discovery almost 200 years ago.

Contributions by the candidate: U. Bünting and D. Haussman grew the crystals and brought the attention to conical refraction. The experiments were performed by the candidate together with H. Henricsson. The mechanism behind polarization control using internal conical refraction was found and analyzed by the candidate, H. Henricsson and V. Pasiskevicius. These three also wrote the paper.

References

1. A. A. Kaminskii, “Laser crystals and ceramics: recent advance,” Laser & Photon. Rev. **1**, No. 2 (2007)
2. E. Snitzer and R. Woodcock, “Yb^{3+}-Er^{3+} Glass Laser,” Appl. Phys. Lett. **6**, 45-46 (1965)
3. G. Karlsson, F. Laurell, J. Tellefsen, B. Denker, B. Galagan, V. Osiko and S. Sverchkov, “Development and characterization of Yb-Er laser glass for high average power laser diode pumping,” Appl. Phys. B **75**, 1-6 (2002)
4. T. Schweizer, T. Jensen, E. Heumann and G. Huber, “Spectroscopic properties and diode pumped 1.6 µm laser performance in Yb-codoped Er: $Y_3Al_5O_{12}$ and Er: Y_2SiO_5,” Opt. Commun. **118**, 557-561 (1995)
5. B. Simondie-Teisseire, B. Viana, A. M. Lejus, J-M Benitez, D. Vivien, C. Borel, R. Templier and C. Wyon, “Room-temperature CW laser operation at ~1.55 µm (eye-safe range) of Yb:Er and Yb:Er:Ce:$Ca_2Al_2SiO_7$ crystals,” IEEE J. Quantum Electron. **32**, 2004-2009 (1996)
6. N. V. Kuleshov, A. A. Lagatsky, V. G. Shcherbitsky, V. P. Mikhailov, E. Heumann, T. Jensen, A. Diening and G. Huber, “CW laser performance of Yb and Er, Yb doped tungstates,” Appl. Phys. B **64**, 409-413 (1997)
7. I. Sokolska, E. Heumann, S. Kuck and T. Lukasiewicz, “ Laser oscillation of Er^{3+}:YVO_4 and Er^{3+}, Yb^{3+}:YVO_4 crystals in the spectral range around 1.6 µm,” Appl. Phys. B **71**, 893-896 (2000)
8. N. A. Tolstik, S. V. Kurilchik, V. E. Kisel, N. V. Kuleshov, V. M. Maltsev, O. V. Pilipenko, E. V. Koporulina and N. I. Leonyuk, “Efficient 1W continuous-wave diode-pumped Er,Yb:$YAl_3(BO3)_4$ laser,” Opt. Lett. **32**, 3233-3235 (2007)
9. P. Burns, J. Dawes, P. Dekker, J. Piper, H. Jiang and J. Wang, “Optimization of Er,Yb:YCOB for cw laser operation,” IEEE J. Quantum Electron. **40**, 1575-1582 (2004)
10. N. V. Kuleshov, A. A. Lagatsky, A. V. Podlipensky, V. P. Mikhailov and G. Huber, “Pulsed laser operation of Yb-doped $KY(WO_4)_2$ and $KGd(WO_4)_2$,” Opt. Lett. **22**, 1317-1319 (1997)
11. J. Liu, U. Griebner, V. Petrov, H. Zhang, J. Zhang and J. Wang, “Efficient continuous-wave and Q-switched operation of a diode-pumped Yb:$KLu(WO_4)_2$ laser with self-Raman conversion,” Opt. Lett. **30**, 2427-2429 (2005)
12. P. Klopp, V. Petrov, U. Griebner, V. Nesterenko, V. Nikolov, M. Marinov, M. A. Bursukova and M. Galan, “Continuous-wave lasing of a stoichometric Yb laser material : $KYb(WO_4)_2$,” Opt. Lett. **28**, 322-324 (2003)
13. F. D. Patel, E. C. Honea, J. Speth, S. A. Payne, R. Hutcheson and R. Equall, “Laser demonstration of $Yb_3Al_5O_{12}$ (YbAG) and materials properties of highly doped Yb:YAG,” IEEE J. Quantum Electron. **37**, 135-144 (2001)

14. C. Stewen, K. Contag, M. Larionov, A. Giesen and H. Hügel, “A 1-kW CW thin disc laser,” IEEE J Sel. Top. Quantum Electron. **6**, 650-657 (2000)

15. A. Beyertt, D. Nickel and A. Giesen, “Femtosecond thin-disk Yb:KYW regenerative amplifier,” Appl. Phys. B **80**, 655-660 (2005)

16. A. D. Pearson and S. P. S. Porto, “Non-radiative energy exchange and laser oscillation in Yb^{3+}-, Nd^{3+} -doped borate glass,” Appl. Phys. Lett. **4**, 202-204 (1964)

17. J. Nilsson, J. K. Sahu, Y. Jeong, V. N. Philippov, D. B. S. Soh, C. A. Codemard, P. Dupriez, J. Kim, D. J. Richardson, A. Malinowski, A. N. Piper, J. H. V. Price, K. Furusawa, W. A. Clarkson and D. N. Payne, “High power fibre lasers,” in *OFC/NFOEC Technical Digest* (Anaheim, USA, 2005), p. 157-159 (2005)

18. R. Hua, S. Wada and H. Tashiro, “Analytical method for design a TEM_{00} mode resonator of a dual-rod Nd:YAG laser with full birefringence compensation,” Opt. Commun. **232**, 333-341 (2004)

19. O. Efimov, L. Glebov, L. Glebova, K. Richardsson and V. Smirnov, “High-efficiency Bragg gratings in photothermorefractive glass,” Appl. Opt. **38**, 619-627 (1999)

20. G. B. Venus, A. Sevian, V. I. Smirnov and L. B. Glebov, “Stable coherent coupling of laser diodes by a volume Bragg grating in photothermorefractive glass,” Opt. Lett. **31**, 1453-1455 (2006)

21. B. Jacobsson, V. Pasiskevicius and F. Laurell, “Single-longitudinal mode Nd-laser with a Bragg-grating Fabry-Perot cavity,” Opt. Express **14**, 9284-9292 (2006)

22. B. Jacobsson, V. Pasiskevicius and F. Laurell, “Tunable single-longitudinal-mode ErYb:glass laser locked by a bulk glass Bragg grating,” Opt. Lett. **31**, 1663-1665 (2006)

23. T. Chung, A. Rapaport, V. Smirnov, L. B. Glebov, M. C. Richardsson and M. Bass, “Solid-state laser spectral narrowing using a volumetric photothermal refractive Bragg grating cavity mirror,” Opt. Lett. **31**, 229-231 (2006)

24. B. Jacobsson, M. Tiihonen, V. Pasiskevicius and F. Laurell, “Narrowband bulk bragg grating optical parametric oscillator,” Opt. Lett. **30**, 2281-2283 (2005)

25. W. R. Hamilton, “Third supplement on an essay on the theory of systems of rays,” Trans. R. Irish Acad. **17**, 1-144 (1837)

26. J. C. Poggendorff, “Über die konische refraktion,” Pogg. Ann. **48**, 461-462 (1839)

27. A. J. Schell and N. Bloembergen, “Laser studies of internal conical diffraction I. Quantitative comparison of experimental and theoretical conical intensity distribution in aragonite,“ J. Opt. Soc. Am, **68**, 1093-1098 (1978).

28. J. P. Fève, B. Boulanger and G. Marnier, “Experimental study of internal and external conical refractions in KTP,” Optics Commun. **105**, 243-252 (1994)

29. A.M. Belsky, M.A. Stepanov, “Internal conical refraction of coherent light beams,” Opt. Commun. **167**, 1-5 (1999)

30. M.V. Berry, M.R. Jeffrey and J.G. Lunney, “Conical refraction: Observations and theory,” Proc. R. Soc. A**462**, 1629-1642 (2006)

31. F. Havermeyer, W. Liu, C. Moser, D. Psaltis and G. J. Steckman, “Volume holographic grating-based continuously tunable optical filter,” Opt. Eng. **43**, 2017-2021 (2004)

32. A. Yariv: “Quantum Electronics,” John Wiley & Sons Inc., USA, 1989

33. M. C. Pujol, M. A. Bursukova, F. Güell, X. Mateos, R. Solé, Jna. Gavaldà, M. Aguiló, J. Massons, F. Díaz, P. Klopp, U. Griebner and V. Petrov, "Growth, optical characterization, and laser operation of a stoichometric crystal $KYb(WO_4)_2$," Phys. Rev. B **65**, 165121 (2002)

34. B. F. Aull and H. P. Jenssen, "Vibronic interactions in Nd:YAG resulting in nonreciprocity of absorption and stimulated emission cross sections," IEEE J. Quantum Electron. **18**, 925-930 (1982)

35. A. E. Siegman: "Lasers", University Science Books, USA 1986

36. S. A. Payne, L. L. Chase, H. W. Newkirk, L. K. Smith and W. F. Krupke, "$LiCaAlF_6:Cr^{3+}$: a promising new solid-state laser material," IEEE J. Quantum Electron. **24**, 2243-2252 (1988).

37. C. Hirt, S. T. Fredrich-Thornton, F. Tellkamp, K. Petermann and G. Huber, "Photoconductivity measurements indicating a nonlinear loss mechanism in highly Yb-doped oxides," in *Technical digest of ASSP* (Nara, Japan, 2008), paper MF1

38. R. Paschotta, P. R. Barber, A. C. Tropper and D. C. Hanna, "Characterization and modelling of thulium:ZBLAN blue upconversion fiber lasers," JOSA B **14**, 1213-1218 (1997)

39. M. Pollnau, T. Graf, J. E. Balmer, W. Luthy and H. P. Weber, "Explanation of the CW operation of the Er^{3+} 3-µm crystal laser," Phys. Rev. A **49**, 3990-3996 (1994)

40. M. Pollnau, P. J. Hardman, M. A. Kern, W. A. Clarkson and D. C. Hanna, "Upconversion-induced heat generation and thermal lensing in Nd:YLF and Nd:YAG," Phys. Rev. B **58**, 16076-16092 (1998)

41. S. C. Tidwell, J. F. Seamans, M. S. Bowers and A. K. Cousins: "Scaling CW diode-end-pumped Nd:YAG lasers to high powers," IEEE J. Quantum Electron. **28**, 997-1009 (1992)

42. W. A. Clarkson and D. C. Hanna: "Resonator design considerations for efficient operation of solid-state lasers end-pumped by high-power diode-bars," in R. Kossowsky et al. (eds.): "Optical resonators – Science and engineering," Kluwer Academic Publishers, Netherlands 1998

43. S. Bjurshagen and R. Koch: "Modeling of energy-transfer upconversion and thermal effects in end-pumped quasi-three-level lasers," Appl. Opt. **43**, 4753-4767 (2004)

44. V. Gapontsev, S. Matitsin, A. Isineev and V. Kravchenko, "Erbium glass lasers and their applications," Opt. Laser Technol. **14**, 189-196 (1982)

45. N. A. Tolstik, A. E. Troshin, V. E. Kisel, N. V. Kuleshov, V. N. Matrosov, T. A. Matrosova and M. I. Kupchenko, "Spectroscopy and continuous-wave diode-pumped laser operation of Er^{3+}, Yb^{3+}:YVO_4 single crystal," in *Technical digest of ASSP* (Incline Village, USA, 2006), paper TuB22

46. D. F. de Sousa, J. A. Sampaio, L. A. O. Nunes, M. L. Baesso, A. C. Bento and L. C. M. Miranda," Energy transfer and the 2.8-µm emission of Er^{3+}- and Yb^{3+}-doped low silica content calcium aluminate glasses," Phys. Rev. B **62**, 3176-3180 (2000)

47. V. P. Gapontsev, S. M. Matitsin and A. A. Inineev, "Channels of energy losses in erbium glasses in the stimulated emission process," Opt. Commun. **46**, 226-230 (1983)

48. B. Denker, B. Galagan, V. Osiko and S. Sverchkov, "Peculiarities of energy storage and relaxation in Yb-Er laser glasses with enhanced Er content," OSA TOPS **50**, 598-602 (2001)

49. B. Simondi-Teisseire, B. Viana, D. Vivien and A. M. Lejus, "Yb^{3+} to Er^{3+} energy transfer and rate-equations formalism in the eye safe laser material Yb:Er:$Ca_2Al_2SiO_7$," Opt. Mater. **6**, 267-274 (1996)

50. L. F. Johnson, H. J. Guggenheim, T. C. Rich and F. W. Ostermayer, "Infrared-to-visible conversion by rare-earth ions in crystals," J. Appl. Phys. **43**, 1125–1137 (1972)

51. J. A. Hutchinson, H. R. Verdun, B. H. T. Chai, B. Zandi and L. D. Merkle, “Spectroscopic evaluation of CaYAlO4 doped with trivalent Er; Tm, Yb and Ho for eyesafe laser applications,” Opt. Mater. **3**, 287–306 (1994)

52. I. Kudryashov, D. Garbuzov and M. Dubinskii, “Volume Bragg grating improves characteristics of resonantly diode-pumped Er:YAG 1.65-µm DPSSL,” Proc. of SPIE **6451**, 64510P (2007)

53. W. A. Clarkson, D. Shen and J. K. Sahu, “High-power fiber-bulk hybrid lasers,” Proc. of SPIE **6100**, 61000A (2006)

54. Y. Jeong, S. Yoo, C. A. Codemard, J. Nilsson, J. K. Sahu, D. N. Payne, R. Horley, P. W. Turner, L. Hickey, A. Harker, M. Lovelady and A. Piper, “Erbium:Ytterbium codoped large-core fiber laser with 297-W continuous-wave output power,” IEEE J. Sel. Top. Quantum Electron. **13**, 573-579 (2007)

55. S. Taccheo, G. Sorbello, P. Laporta, G. Karlsson and F. Laurell, “230-mW diode-pumped single-frequency Er:Yb laser at 1.5 µm,” Photonics Tech. Lett. **13**, 19-21 (2001)

56. T. L. Boyd, D. Klemer, P. A. Leilabady, J. Noriega and M. Pessot, “A 1.55-µm solid state laser source for DWDM applications,” IEEE J. Light. Tech. **17**, 1904-1908 (1999)

57. A. Diening, E. Heumann, G. Huber and O. Kuzmin, “High-power diode-pumped Yb,Er:LSB laser at 1.56 µm,” in *CLEO Technical Digest* (San Fransisco, USA, 1998), p 299-300

58. J. J. Degnan, “Optimization of passively Q-switched lasers,” IEEE J. Quantum Electron. **31**, 1890-1901 (1995)

59. G. Karlsson, V. Pasiskevicius, F. Laurell, J. A. Tellefsen, B. Denker, B. I. Galagan, V. V. Osiko and S. Sverchkov, ”Diode-pumped Er-Yb:glass laser passively Q-switched by use of Co^{2+}:$MgAl_2O_4$ as a saturable absorber,” Appl. Opt. **39**, 6188-6192 (2000)

60. E. Georgiou, F. Kiriakidi, O. Musset and J.-P Boquillon, ”1.65-µm Er:Yb:YAG diode-pumped laser delivering 80-mJ pulse energy,” Opt. Engineering **44**, 064202 (2005)

61. N. Leonyuk, V. V. Maltsev, E. A. Volkova, O. V. Pilipenko, E. V. Koporulina, V. E. Kisel, N. A. Tolstik, S. V. Kurilchik and N. V. Kuleshov, “Crystal growth and laser properties of new $RAl_3(BO_3)_4$ (R = Yb, Er) crystals),” Opt. Mater. **30**, 161-163 (2007)

62. L. A. Riseberg and H. W. Moos, “Multiphonon Orbit-Lattice Relaxation of Excited States of Rare-Earth Ions in Crystals,” Phys. Rev. **174**, 429-438 (1968)

63. H. Giesber, J. Ballato, G. Chumanov, J. Kolis and M. Dejneka, “Spectroscopic properties of Er^{3+} and Eu^{3+} doped acentric $LaBO_3$ and $GdBO_3$,” J. Appl. Phys. **93**, 8987-8994 (2003)

64. V. A. Lebedev, V. F. Pisarenko, Yu. M. Chuev, A. A. Perfilin, A. G. Avanesov, V. V. Zhorin, A. G. Ohrimchuk and A. V. Shestakov, “Study of energy transfer from Yb^{3+} to Er^{3+} in rare-earth silicates and borates,” J. Lumin. **72-74**, 942-944 (1997)

65. A. Lorriaux-Rubbens, G. Aka, E. Antic-Fidancev, D. A. Keszler and F. Wallart, “Polarized Raman spectra of the non-linear and laser crystal Ca/sub 4/GdO(BO/sub 3/)/sub 3/ (GdCOB),” J. Raman Spectroscopy **31**, 535-538 (2000)

66. L. F. Johnson, H. J. Guggenheim, T. C. Rich and F. W. Ostermayer, “Infrared-to-visible conversion by rare-earth ions in crystals,” J. Appl. Phys. **43**, 1125–1137 (1972)

67. D. Jaque, M. O. Ramirez, L. E. Bausá, J. Garcia Solé, E. Cavalli, A. Speghini and M. Bettinelli, “$Nd^{3+} \rightarrow Yb^{3+}$ energy transfer in the $YAl_3(BO_3)_4$ nonlinear laser crystal,” Phys. Rev. B **68**, 035118 (2003)

68. A. F. Obaton, C. Parent, G. Le Flem, P. Thony, A. Brenier and G. Boulon, "Yb^{3+}–Er^{3+}-codoped $LaLiP_4O_{12}$ glass: a new eye-safe laser at 1535 nm ," J. Alloys and Comp. **300-301**, 123-130 (2000)

69. S. Campos, A. Denoyer, S. Jandl, B. Viana, D. Vivien, P. Loiseau and B. Ferrand, "Spectroscopic studies of Yb-doped rare-earth orthosilicate crystals," J. Phys.: Condens. Matter **16**, 4579-4590 (2004)

70. L. Macalik, J. Hanuza, A. A. Kaminskii: "Polarized infrared and Raman spectra of $KGd(WO_4)$ and their interpretation based on normal coordinate analysis," J. Raman Spectroscopy **33**, 92-103 (2002)

71. H. R. Xia, L. X. Li, H. J. Zhang, X. L. Meng, L. Zhu, Z. H. Yang, X. S. Liu and J. Y. Wang, "Raman spectra and laser properties of Yb-doped yttrium orthovanadate crystals," J. Appl. Phys. **87**, 269-273 (2000)

72. G. Aka, A. Kahn-Harari, F. Mougel, D. Vivien, F. Salin, P. Coquelin, P. Colin, D. Pelenc and J. P. Damelet, "Linear- and nonlinear-optical properties of a new gadolinium calcium oxoborate crystal, $Ca_4GdO(BO_3)_3$," J. Opt. Soc. Am. B **14**, 2238-2247 (1997)

73. S. Zhang, Z. Cheng, J. Lu, G. Li, J. Lu, Z. Shao and H. Chen, "Studies on the effective non-linear coefficient of $GdCa_4O(BO_3)_3$ crystal," J. Cryst. Growth **205**, 453-456 (1999)

74. F. Mougel, A. Kahn-Harari, G. Aka and D. Pelenc, "Structural and thermal stability of Czochralski grown GdCOB oxoborate single crystals," J. Mater. Chem. **8**, 1619-1623 (1998)

75. M. C. Pujol, R. Solé, J. Massons, Jna. Gavaldà, X. Solans, C. Zaldo, F. Díaz and M. Aguiló, "Structural study of monoclinic $KGd(WO_4)_2$ and effects of lanthanide substitution," J. Appl. Cryst. **34**, 1-6 (2001)

76. M. C. Pujol, M. Rico, C. Zaldo, R. Solé, V. Nikolov, X. Solans, M. Aguiló and F. Díaz, "Crystalline structure and optical spectroscopy of Er^{3+}-doped $KGd(WO_4)_2$ single crystals," Appl. Phys. B**68**, 187-197 (1999)

77. A. Brenier, "A new evaluation of Yb^{3+}-doped crystals for laser applications," J. Lum. **92**, 199-204 (2001)

78. S. Erhard, J. Gao, A. Giesen, K. Contag, A. A. Lagatsky, A. Abdolvand, N. V. Kuleshov, J. Aus der Au, G. J. Spühler, F. Brunner, R. Paschotta and U. Keller: "High power Yb:KGW and Yb:KYW thin disk laser operation," in *CLEO Technical Digest* (Baltimore, USA, 2001), p 333-334

79. G. Paunescu, J. Hein, R. Sauerbrey: "100-fs diode-pumped Yb:KGW mode-locked laser," App. Phys. B**79**, 555-558 (2004)

80. A. A. Lagatsky, A. Abdolvand and N. V. Kuleshov, "Passive Q-switching and self-frequency Raman conversion in a diode-pumped Yb:$KGd(WO_4)_2$ laser," Opt. Lett. **25**, 616-618 (2000)

81. S. Biswal, S. P. O'Connor and S. R. Bowman, "Thermo-optical parameters measured in ytterbium-doped potassium gadolinium tungstate," Appl. Opt. **44**, 3093-3097 (2005)

82. A. A. Demidovich, A. N. Kuzmin, G. I. Ryabtsev, M. B. Danailov, W. Strek and A. N. Titov, "Influence of Yb concentration on Yb:KYW laser properties," J. Alloys and Comp. **300-301**, 238-241 (2000)

83. W. Ying-wei, C. Hao-bo and L. Jing-He, "Raw material synthesis and single crystal growth of Yb:KGW laser," J. synth. cryst. **33**, 887-891 (2004)

84. H. M. Pask, "The design and operation of solid-state Raman lasers," Prog. Quantum Electron. **27**, 3-56 (2003)

85. K. Petermann, D. Fagundes- Peters, M. Mond, V. Peters, J. J. Romero, S. Kutovoi, J. Speiser and A. Giesen, “Highly Yb-doped oxides for thin-disc lasers,” J. Crystal Growth **275**, 135-140 (2005)

86. N. V. Kuleshov, A. A. Legatsky, A.V. Podlipensky, V. P. Mikhailov, A. A. Kornienko, E. B. Dunina, S. Hartung and G. Huber, “Fluorescence dynamics, excited-state absorption and stimulated emission of Er^{3+} in $KY(WO_4)_2$,” J. Opt. Soc. Am. B **15**, 1205–1212 (1998).

87. S. P. Arutunyan, Kh. S. Bagdasarov, A. P. Dodokin and A. M. Kevorkov, Sov. J. Solid State Phys. **28**, 957-961 (1985)

88. J. B. Gruber, J. R. Quagliano, M. F. Reid, F. S. Richardson, M. E. Hills, M. D. Seltzer, S. B. Stevens, C. A. Morrison and T. H. Allik, “Energy levels and correlation crystal-field effects in Er^{3+} -doped garnets,” Phys. Rev. B **48**, 15561-15573 (1993)

89. T. Y. Fan, D. J. Ripin, R. L. Aggarawal, J. R. Ochoa, B. Chann, M. Tilleman and J. Spitzberg, ”Cryogenic Yb^{3+}-doped solid-state lasers,” IEEE J. Sel. Top. Quantum Electron. **13**, 448-458 (2007)

90. S. Chénais, F. Balemois, F. Druon, G. Lucas-Leclin and P. Georges, “Thermal lensing in diode-pumped ytterbium lasers – Part II: Evaluation of quantum efficiencies and thermo-optic coefficients,” IEEE J. Quantum Electron. **40**, 1235-1243 (2004)

91. A. A. Lagatsky, N. V. Kulsehov and V. P. Mikhailov, ” Diode-pumped CW lasing of Yb:KYW and Yb:KGW,” Optics Commun. **165**, 71-75 (1999)

92. J. Liu, X. Mateos, H. Zhang, J. Wang, M. Jiang, U. Griebner and V. Petrov, ”Characteristics of a continuous-wave $Yb:GdVO_4$ laser end pumped by a high-power diode,” Opt. Lett. **31**, 2580-2582 (2006)

93. J. Kong, D. Y. Tang, B. Zhao, J. Lu, K. Ueda, H. Yagi and T. Yanagitani, “9.2-W diode-end-pumped $Yb:Y_2O_3$ ceramic laser,” Appl. Phys. Lett. **86**, 161116 (2005)

94. M. Hai xia, L. Qi hong, Q. Yun feng, D. Jing xing and W. Yun rong, “5.5 W CW $Yb^{3+}:Y_2O_3$ ceramic laser pumped with 970 nm laser diode,” Opt. Commun. **246**, 465-469 (2004)

95. W. Li, S. Xu, H. Pan, L. Ding, H. Zeng, W. Lu, G. Guo, G. Zhao, G. Yan, L. Su and J. Xu, “Efficient tunable diode-pumped Yb:LYSO laser,” Opt. Express **14**, 6681-6686 (2006)

96. J. Liu, V. Petrov, H. Zhang and J. Wang,” Power scaling of a continuous-wave and passively Q-switched $Yb:KLu(WO_4)_2$ laser end-pumped by a high-power diode,” Appl. Phys. B **88**, 527-530 (2007)

97. U. Brauch, A. Giesen, M. Karszewski, Chr. Steven and A. Voss, ” Multiwatt diode-pumped Yb:YAG thin disk laser continuously tunable between 1018 and 1053 nm,” Opt. Lett. **20**, 713-715 (1995)

98. F. D. Patel, E. C. Honea, J. Speth, S. A. Payne, R. Hutcheson and R. Equall, “Laser demonstration and material properties of highly doped Yb:YAG,” IEEE J. Quantum Electron. **37**, 135-144 (2001)

99. A. Brenier, Y. Guyot, H. Canibano, G. Boulon, A. Ródenas, D. Jaque, A. Eganyan and A. G. Petrosyan, “Growth, spectroscopic and laser properties of Yb^{3+}-doped $Lu_3Al_5O_{12}$ garnet crystal,” J. Opt. Soc. Am. B **23**, 676-683 (2006)

100. D. S. Sumida, T. Y. Fan and R. Hutcheson, ”Spectroscopy and diode-pumped lasing of Yb^{3+}-doped $Lu_3Al_5O_{12}$ (Yb:LuAG),” in *Technical digest of ASSL* (Memphis, USA, 1995), p 348-349 (2005)

101. V. E. Kisel, A. E. Troshin, N. A. Tolstik, V. G. Shcherbitsky, N. V. Kuleshov, V. N. Matrosov, T. A. Matrosova and M. I. Kupchenko, "Q-switched Yb^{3+}:YVO4 laser with Raman self-conversion," Appl. Phys. B **80**, 471-473 (2005)

102. C. Kränkel, D. Fagundes-Peters, S. T. Fredrich, J. Johannsen, M. Mond, G. Huber, M. Bernhagen and R. Uecker, "Continuous wave laser operation of Yb^{3+}: YVO_4," Appl. Phys. B **79**, 543-546 (2004)

103. M. Hildebrandt, U. Bünting, U. Kosch, D. Haussman, T. Levy, M. Krause, O. Müller, U. Bartuch and W. Viöl, "Diode-pumped Yb:KYW thin-disk laser operation with wavelength tuning to small quantum defects," Opt. Commun. **259**, 796-798 (2006)

104. J. Petit, P. Goldner, B. Viana, J. Didierjean, F. Balembois, F. Druon and P. Georges, "Quest of athermal solid-state laser: Case of Yb:$CaGdAlO_4$," *Technical digest of ASSP* (Incline Village, USA, 2006), paper WD1 (2006)

105. W. Li, Q. Hao, H. Zhai, H. Zeng, w. Lu, G. Zhao, C. Yan, L. Su and J. Xu," Low-threshold and continuously tunable Yb:Gd_2SiO_5 laser," Appl. Phys. Lett. **89**, 101125 (2006)

106. M. Jacquemet, F. Balembois, S. Chenais, F. Druon, P. Georges, R. Gaume and B. Ferrand, "First diode-pumped Yb-doped solid-state laser continuously tunable between 1000 and 1010 nm," Appl. Phys. B **78**, 13-18 (2004)

107. M. Jacquemet, C. Jacquemet, N. Janel, F. Druon, F. Balembois, P. Georges, J. Petit, B. Viana, D. Vivien and B. Ferrand, "Efficient laser action of Yb:LSO and Yb:YSO oxyorthosilicates crystals under high-power diode-pumping," Appl. Phys. B **80**, 171-176 (2005)

108. C. Kränkel, J. Johannsen, R. Peters, K. Petermann and G. Huber, " Continuous-wave high power laser operation and tunability of Yb:$LaSc_3(BO_3)^4$ in thin disk configuration," Appl. Phys. B **87**, 217-220 (2007)

109. P. Dekker, J. M. Dawes, J. A. Piper, Y. Liu and J. Wang, " 1.1 W CW self-frequency-doubled diode-pumped Yb:$YAl_3(BO_3)_4$ laser," Opt. Commun. **195**, 431-436 (2001)

110. P. Dekker, J. M. Dawes and J. A. Piper, "2.27-W Q-switched self-doubling Yb:YAB laser with controllable pulse length," J. Opt. Soc. Am. B **22**, 378-384 (2005)

111. J. L. Blows, P. Dekker, P. Wang, J. M. Dawes and T. Omatsu, "Thermal lensing measurements and thermal conductivity of Yb:YAB," Appl. Phys. B **76**, 289-292 (2003)

112. J. Liu, X. Mateos, H. Zhang, J. Li, J. Wang and V. Petrov, "High-power laser performance of Yb:$YAl_3(BO_3)_4$ crystals cut along the crystallographic axes," IEEE J. Quantum Electron. **43**, 385-390 (2007)

113. R. Peters, C. Krankel, K. Petermann and G. Huber, "Broadly tunable high-power Yb:Lu_2O_3 thin disk laser with 80 % slope efficiency," Opt. Express **15**, 7075-7082 (2007)

114. K. Petermann, G. Huber, L. Fornasiero, S. Kuch, E. Mix, V. Peters and S. A. Basun, "Rare-earth-doped sesquioxides," J. Lumin. **87**, 973-975 (2000)

115. A. Dergachev, J. H. Flint, Y. Isyanova, B. Pati, E. V. Slobodtchikov, K. F. Wall and P. F. Moulton, " Review of multipass slab laser systems," IEEE J. Sel. Top. Quantum Electron. **13**, 647-659 (2007)

116. A. J. Bayramian, C. Bibeau, C. D. Marshall, S. A. Payne and W. F. Krupke, "3-Level quasi-CW laser operation and Q-switching of Yb:S-FAP at 985 nm," in *Conference Proceedings of LEOS* (San Fransisco, USA, 1999) p 910-911 (1999)

117. M. Fujita, E. Sano, R. Kubo, T. Kawashima, M. Yamanaka, Y. Izawa, S. Nakai and C. Yamanaka, “New potential of a direct laser-diode-pumped Yb:YAG laser,” Jpn J Appl Phys Part 2 Letter **39**, L1300-1301 (2000)

118. L. B. Glebov, “Kinetics modelling in photosensitive glass,” Opt. Mater. **25**, 413-418 (2004)

119. B. Volodin, S. Dolgy, E. Melnik, E. D. J. Shaw and V. Ban, “Wavelength stabilization and spectral narrowing of high-power multimode laser diodes and arrays by use of volume Bragg gratings,” Opt. Lett. **29**, 1891-1893 (2004)

120. S. Giet, H. Sun, S. Calvez, M. Dawson, S. Suomalainen, A. Harkonen, M. Guina, O. Okhotnikov and M. Pessa, “Spectral narrowing and locking of a vertical-external-cavity surface-emitting laser using an intracavity volume Bragg grating,” IEEE Photon. Technol. Lett. **18**, 1786-1788 (2006)

121. M. Henriksson, M. Tiihonen, V. Pasiskevicius and F. Laurell, “$ZnGeP_2$ parametric oscillator pumped by a linewidth narrowed 2 μm source,” Opt. Lett. **31**, 1878-1880 (2006)

122. H. Kogelnik, “Coupled wave theory for thick hologram gratings,” Bell. Sys. Tech. J. **48**, 2909-2947 (1969)

123. R. S. Chu, J. A. Kong and T. Tamir, “Diffraction of gaussian beams by a periodically modulated layer,” J. Opt. Soc. Am. **67**, 1555-1561 (1977)

124. B. Benlarbi, P. S. J. Russel and L. Solymar, ”Bragg diffraction of gaussian beams by thick gratings: two rival theories,” Appl. Phys. B **28**, 63-72 (1982)

125. I. V. Ciapurin, L. B. glebov and V. I. Smirnov, “Modeling of phase volume diffractive gratings, part 1: transmitting sinusoidal uniform gratings,” Opt. Eng. **45**, 015802 (2006)

126. M. G. Moharam, T. K. Gaylord and R. Magnusson, “Bragg diffraction of finite beams by thick gratings,” J. Opt. Soc. Am. **70**, 300-304 (1980)

127. P. S. J. Russel and L. Solymar, “Borrman-like anomalous effects in volume holography,” Appl. Phys. **22**, 335-353 (1980)

128. M. G. Moharam, E. B. Grann, D. A. Pommet and T. K. Gaylord, ”Formulation for stable and efficient implementation of the rigorous coupled-wave analysis of binary gratings,” J. Opt. Soc. Am. A **12**, 1068-1076 (1995)

129. H.-T. Hsieh, W. Liu, F. Havermeyer, C. Moser and D. Psaltis, “Beam-width-dependent filtering properties of strong volume holographic gratings,” Appl. Opt. **45**, 3774-3780 (2006)

130. H. Shu and M. Bass, “Modeling the reflection of a laser beam by a deformed highly reflective volume Bragg grating,” Appl. Opt. **46**, 2930-2938 (2007)

131. S. Biswal, S. P. O’Connor and S. R. Bowman, “Nonradiative losses in $Yb:KGd(WO_4)_2$ and $Yb:Y_3Al_5O_{12}$,” Appl. Phys. Lett. **89**, 091911 (2006)

132. S. Bjurshagen, P. Brynolfsson, V. Pasiskevicius, I. Parreu, M. C. Pujol, A. Peña, M. Aguiló and F. Díaz, “Crystal growth, spectroscopic characterization and eye-safe laser operation of Er and Yb co-doped $KLu(WO_4)_2$,” submitted to Appl. Opt.